Integration of fiber mirrors and ion traps for a high-fidelity quantum interface

Dissertation

Zur Erlangung des Doktorgrades an der

Fakultät für Mathematik, Informatik und Physik
der Leopold-Franzens-Universität Innsbruck
vorgelegt von

Dipl. Ing. Birgit Ursula Brandstätter

durchgeführt am Institut für Experimentalphysik

unter der Leitung von
Univ.-Prof. Dr. Rainer Blatt

Innsbruck, Juli 2013

Abstract

Optical cavities can be used as efficient quantum interfaces between photons and atoms to realize a quantum network. In such a network, photonic channels link quantum nodes composed of trapped atoms. Due to decoherence, however, the technical requirements for the building blocks of such a network are demanding. Trapped ions are promising realizations of network nodes as they allow for efficient initialization, coherent manipulation, and readout of quantum states. In combination with cavities of small mode volumes, which provide a high coupling rate between ions and single cavity photons, high fidelities and efficiencies for network protocols are achieved. Cavities constructed from mirrors fabricated on fiber facets provide such small mode volumes.

This thesis presents the development of an integrated ion-trap fiber-cavity setup. The trap is a miniaturized linear Paul trap which features a deep trapping potential, optical access to detect and manipulate ions, and clearance for a fiber-based Fabry-Perot cavity. The small dimensions of the fiber mirrors allow us to minimize the influence of the dielectric mirrors on the trapping potential seen by the ion. The cavity parameters are designed for strong coupling between a single ion and a cavity photon with coherent effects dominating over decoherence in the system. Simulations of network protocols such as ion-photon state mapping and ion-photon entanglement show the advantage of a fiber-cavity system over a system with a smaller coupling rate.

Zusammenfassung

Optische Resonatoren können als effiziente Quantenschnittstelle zwischen Photonen und Atomen und somit für den Aufbau eines Quantennetzwerkes verwendet werden. In solchen Netzwerken verbinden optische Kanäle stationäre Prozessoren, die durch einzelne Atome realisiert werden. Aufgrund der Dekohärenz in Quantensystemen sind die technischen Anforderungen für die Bausteine eines solchen Netzwerkes äußerst anspruchsvoll. Eine vielversprechende Realisierung für Quantenprozessoren verwendet gefangene Kalziumionen. Kalziumionen können effizient initialisiert und ausgelesen werden und lassen präzise kohärente Manipulationen zu. In Kombination mit optischen Resonatoren mit kleinem Modenvolumen, welche hohe Kopplungsraten zwischen Ionen und Resonatorphotonen ermöglichen, können Netzwerkprotokolle hoher Güten und Effizienzen realisiert werden. Solche Resonatoren mit kleinem Modenvolumen können aus Spiegeln, die auf Faserfacetten produziert werden, hergestellt werden.

In dieser Doktorarbeit wird die Entwicklung eines Ionenfallen-Faserresonator-Aufbaus vorgestellt. Als Falle wird eine miniaturisierte lineare Paulfalle verwendet. Die Falle bietet ein tiefes Fallenpotenzial, guten optischen Zugang, um Ionen zu detektieren und zu manipulieren, und Raum für einen Faser-basierten Fabry-Perot Resonator. Die kleinen Abmaße der Faserspiegel erlauben zusätzlich, den Einfluss der dielektrischen Spiegel auf das Fallenpotenzial des Ions zu minimieren. Die Parameter des optischen Resonators sind so gewählt, dass kohärente Effekte über Dekohärenz im System dominieren. Simulationen von Netzwerkprotokollen, wie die Übertragung eines Quantenzustandes von einem Ion auf ein Photon und die Verschränkung zwischen einem Ion und einem Photon, zeigen die Überlegenheit eines Faserresonatorsystems über ein System mit niedrigerer Kopplungsrate.

Contents

1 Introduction

A single atom coupled to a single photon is one of the most fundamental quantum mechanical systems. Through the interaction of the atomic multipole with the light field, quanta of energy are exchanged. A high-finesse cavity increases the amplitude of the field of one electromagnetic mode, thus enhancing this interaction and acting as an interface between the atom and a photon in the field.

The coupling is a coherent, reversible interaction, whose strength is given by the rate at which quanta are exchanged in the system. As in all quantum mechanical systems, however, dissipative interactions with the environment lead to decoherence. If the coherent interaction dominates over such dissipative mechanisms, the system is in the strong coupling regime, a regime of great interest in the field of cavity quantum electrodynamics (CQED).

Coupled atom-photon systems are explored in the field of quantum information science (Zol05). Analogous to a classical network with processors sharing and exchanging information, in a quantum network (Cir97), the quantum processors located at network nodes generate, store, and process quantum information, while the channels transport quantum information from node to node. The distribution of quantum information is made possible by a quantum interface which coherently transfers quantum information from a node to a channel and vice versa (Kim08).

The fundamental unit of such quantum information, the qubit (quantum bit), is the quantum mechanical analogue of a classical bit of information. Experimentally, the electronic states of atoms have proven to be excellent realizations for the physical implementation of such stationary qubits at quantum nodes. Similarly, the polarization states of photons are ideal implementations of flying qubits traveling through quantum channels (Zol05), and the cavity provides the interface between atomic qubits and photonic qubits. The building blocks for an elementary quantum network have recently been implemented in the conceptually simple system of single neutral atoms in distant high-finesse cavities (Rit12).

Compared to neutral atoms, however, trapped ions offer a range of advantages making them uniquely suited for quantum networks: ions are trapped stably in Paul traps (Pau58, Fis59, Wue59, Pau90) for several days, localized to within 10 nm via ground-state cooling, and can be individually positioned and addressed in a cavity (Cas13). Furthermore, trapped ions are promising candidates for quantum information processing, as techniques for high-fidelity quantum operations such as initialization, manipulation, and readout are well established for ions (Lei03a, Häf08). Therefore, several research groups worldwide are currently working on the technological challenge of integrating ions and cavities with the aim of realizing a quantum network. The coupling of ions to the field of a high-finesse cavity has already been shown in a range of setups (Gut01, Mun02, Rus09, Lei09, Her09, Ste12, Ste13).

For a high-fidelity ion-photon quantum interface, the coherent coupling strength g

must be larger than the ion's rate of spontaneous decay. In order to maximize this coupling strength in CQED systems, the interaction with the cavity mode can be enhanced by a factor of $\sqrt{N}$ by coupling N atoms to the mode, as shown in (Her09). To enhance the coupling of a single atom, in contrast, both the cavity length L and the cavity waist w_0 should be minimized, as $g \propto (w_0\sqrt{L})^{-1}$. Such small dimensions are realized by the development of optical microcavities, which require mirror surfaces with small radii of curvature, compatible with small lengths and waists. Additionally, the mirror substrates should have low surface roughness to minimize losses in the mirror coating.

State-of-the-art low-loss coatings at optical wavelengths are dielectric. The challenge for an ion in a microcavity is that charges on these dielectrics distort the ion's trapping potential. Other mirror materials, such as metals, have too high mirror losses in the optical domain and would put the setup in the bad cavity regime, in which cavity losses dominate the system dynamics. Therefore, strong coupling has only been achieved with neutral atom systems (Rai01, Mil05), whereas current ion-cavity setups operate in the intermediate coupling regime (Gut01, Mun02, Rus09, Lei09, Ste12, Ste13) in which the coherent coupling rate between a single ion and a photon is smaller than the rate of at least one of the relevant incoherent processes (scattering from the ion and loss from the cavity). Such experiments are limited by the technological complexity of combining a stable ion trap with a high-finesse microcavity.

Fiber-based Fabry-Perot cavities provide both a high coupling rate and a small dielectric cross section and are thus promising candidates to be integrated with ions (Hun10). The term fiber-based Fabry-Perot cavity (FFPC) describes two opposing optical fiber tips, each with a mirror coating. At least one of the mirror surfaces is concave and aligned relative to the other such that a stable standing wave forms between them. Laser machining of fiber mirrors produces radii of curvature that are two orders of magnitude smaller than radii of curvature of state-of-the-art substrate mirrors (Hun10). Thus, short cavity length and small cavity waists are inherent to such fiber cavities, allowing for high coupling rates. This technology was pioneered by our collaborator Jakob Reichel, who reached the strong coupling regime with a fiber cavity integrated with neutral atoms trapped on an atom chip (Col07).

In our laboratory, we have two experimental setups that integrate a linear ion trap with an optical cavity. The first design uses a cavity constructed with high-finesse substrate mirrors. This setup operates in a regime which is dominated by the atomic decay rate. The second apparatus is meant to overcome the technological challenges of bringing ions close to dielectric mirrors and to reach the strong-coupling regime by integrating an FFPC with an ion trap. Both setups use $^{40}\mathrm{Ca}^+$ trapped in a linear Paul trap.

The first apparatus was set up almost 10 years ago by Carlos Russo during his thesis work (Rus08). The ion trap is mounted vertically from above in the vacuum chamber. Left and right from the trap center, cavity mirrors are mounted from below with a separation $L = (19.96 \pm 0.02)$ mm. The cavity consists of macroscopic mirrors with radius of curvature $R = (10.02 \pm 0.01)$ mm. The configuration is such that the mirrors form a cavity in the near-concentric regime with a small waist $w_0 = (13.2 \pm 0.8)$ µm and thus a high coupling rate g on the order of 1 MHz. A measure for the reflectivity of the mirrors is the finesse, which for this cavity is 7×10^4 at 866 nm.

This setup has been used in the recent years to demonstrate tunable photon statistics

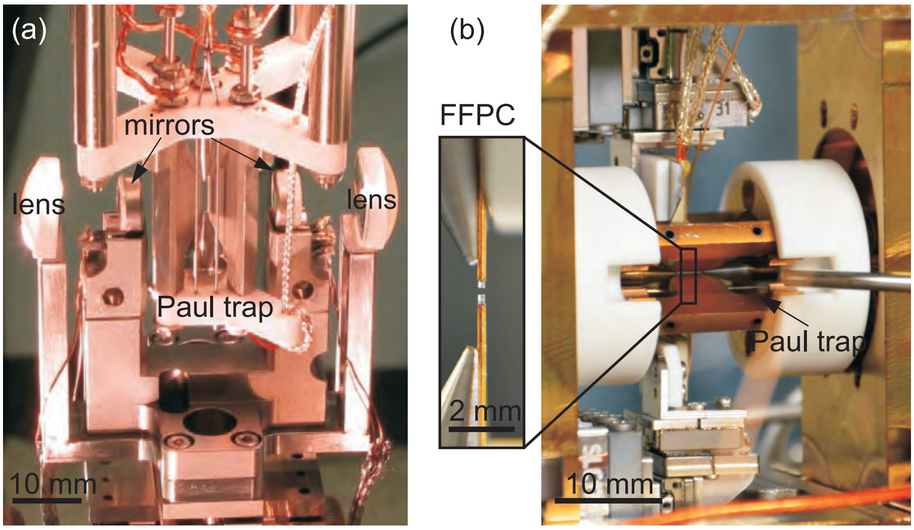

Figure 1.1: (a) Photograph taken by Carlos Russo of the cavity-trap system that he designed and developed. The ion trap is mounted vertically from above. The cavity mounted horizontally from below has a length of 20 mm and is orthogonal to the trap axis. (b) Photo of the new cavity-trap setup whose development is described in this thesis. Here, the optical fibers with concave mirrors on the tips are mounted vertically from below and above the trap center. The inset (photo taken by Klemens Schüppert) shows a fiber-based Fabry Perot resonator (FFPC) to indicate the position of the fibers in the setup.

of a single ion (Dub10) and the production of single photons inside the cavity with high efficiency, as described in Helena Barros' thesis (Bar09). More recently, three quantum-communication protocols have been implemented: entanglement between a single ion and a cavity photon (Stu12c), quantum-state mapping from an ion to a cavity photon (Stu13), and heralded ion-ion entanglement via the cavity (Cas13). The first two experiments were the focus of Andreas Stute's thesis (Stu12a), while the third is part of Bernardo Casabone's thesis work. My role in these experiments was primarily to contribute numerical simulations, which are presented in Chapter 3 together with an overview of the experimental protocols and results. The simulations provide an understanding of the protocols and analyze the effects that limit the success of the experimental processes.

In order to be able to increase the quantum interface's fidelity and efficiency, both requirements for scalable quantum computing, we want to reach the strong-coupling regime of CQED with ions. Access to this new parameter regime required the development and construction of a second experimental apparatus based on an FFPC. The design and its implementation were the primary focus of my thesis work and represent a first step towards strong coupling between a single ion and a cavity photon.

This thesis presents the various steps in the development of this apparatus and its technological challenges, addressing possible solutions. Chapter 4 shows several ion-trap designs and simulations of the corresponding trap potentials. The development and optimization of FFPCs for ion traps is discussed in Chapter 5. Solutions for specific technological challenges are elaborated, including the annealing and baking of fiber mirrors (Chapter 6). Finally, Chapter 7 introduces the novel design for a linear Paul trap integrated with a fiber cavity, which should enable us to reach the strong coupling regime with a single calcium ion. Chapter 8 concludes with an outlook on quantum-communication experiments in a new parameter regime of CQED. The protocols presented in Chapter 3 are revisited, highlighting the possibilities that the new apparatus affords.

2 Foundations

This thesis work, summarized in the outlook above, relies on the body of knowledge accumulated over many years of research in Rainer Blatt's Quantum Optics group in Innsbruck. The research group works primarily with calcium. To use $^{40}\mathrm{Ca}^+$ as a qubit at the node of a quantum network, the ion is coupled to a cavity. Our cavity experiments employ a sophisticated set of techniques including trapping, cooling, addressing, and coherently manipulating single ions. Here, the important aspects of this quantum optics background are summarized. Specific details of the techniques are published in several publications of the research group, such as (Häf08). Particularly helpful in understanding basic concepts is Christian Roos' thesis (Roo00) and, for reading more about sophisticated methods, the thesis of Thomas Monz (Mon11a).

2.1 $^{40}\mathrm{Ca}^+$ as a quantum bit

The five lowest electronic levels of $^{40}\mathrm{Ca}^+$ are shown in Fig. 2.1. The system comprises one ground state, $4^2S_{1/2}$; two metastable states, $3^2D_{3/2}$ and $3^2D_{5/2}$; and two short-lived excited states, $4^2P_{1/2}$ and $4^2P_{3/2}$. Both the 3^2D and the 4^2P states are energetically split by spin-orbit coupling. More detail about the Zeeman structure of the ion is given in the next chapter (Sec. 3.1.1).

Experimentally, $^{40}\mathrm{Ca}^+$ is loaded from a neutral calcium beam, which traverses the trap center. Via a two-photon process, the atoms are ionized (Gul01) and are then confined in the potential provided by the linear Paul trap. A red-detuned laser cools the ions on the transition $4^2S_{1/2} \leftrightarrow 4^2P_{1/2}$ (Hän75, Win75) via Doppler cooling. The ion can decay to the metastable $3^2D_{3/2}$ state, and therefore, an additional laser is required to repump the population. During Doppler cooling, the atomic fluorescence from $4^2P_{1/2}$ to $4^2S_{1/2}$ is used to image the ions via a high-numerical-aperture objective either with a charge-coupled-device camera or with a photo-multiplier tube.

The minimal temperature of the ions after Doppler cooling is proportional to the linewidth of the cooling transition. The ions can be cooled further to the vibrational ground state of their collective motion in the trap via sideband cooling (Lei03a). This requires an ultrastable laser at 729 nm driving the quadrupole transition between the $4^2S_{1/2}$ and the $3^2D_{5/2}$ manifolds, which is available in our laboratory (Chw09).

Each ion can be used to represent a qubit, taking advantage of the long lifetimes of the $3^2D_{3/2}$ and $3^2D_{5/2}$ states. In the ion, binary quantum information is assigned to two electronic levels. Typically, the qubit is realized on the optical $4^2S_{1/2} \leftrightarrow 3^2D_{5/2}$ transition (Häf08). In principle, however, information can be encoded in any of the electronic states, e.g., in two different spin states of the same manifold, such as the $3^2D_{5/2}$ manifold or the $4^2S_{1/2}$ manifold.

Quantum computation with a string of ions requires single and multi-qubit operations, which are implemented via coherent manipulations between the qubit states. The ultra-

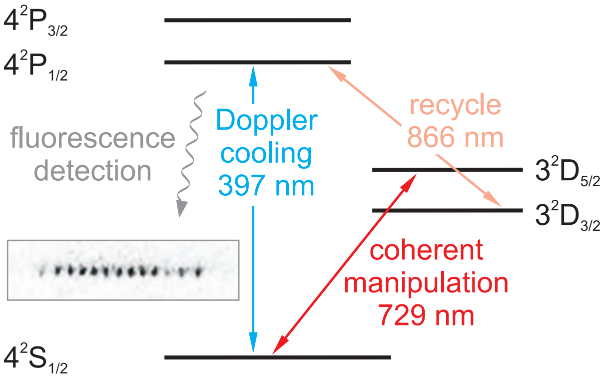

Figure 2.1: Transitions in $^{40}\mathrm{Ca}^+$. The ion is cooled on the $4^2S_{1/2} \leftrightarrow 4^2P_{1/2}$ transition, and population from the metastable $3^2D_{3/2}$ is recycled. Atomic fluorescence is used to image single or multiple ions. The inset shows a charge-coupled-device (CCD) camera image of a linear string of ions. Coherent qubit rotations are implemented between the ground state $4^2S_{1/2}$ and the metastable $3^2D_{5/2}$ state.

stable 729 nm laser coupling the $4^2S_{1/2}$ and the $3^2D_{5/2}$ states is used for these coherent operations. When applying laser light at the atomic transition frequency, the ion's state population oscillates between the two states with the Rabi frequency. Therefore, the phase and the length of the $4^2S_{1/2} \leftrightarrow 3^2D_{5/2}$ pulses can be adjusted to set phase and amplitudes of the qubit state. By addressing a tightly focussed laser beam on only one ion, single-qubit gates are realized.

Two or multiple-qubit gates are implemented via the common vibrational motion in the harmonic trap potential, which mediates interactions between individual qubits in the trap. Using the Mølmer-Sørensen entangling interaction (Sø99), two qubits have been entangled with more than 99% fidelity (Ben08), and entangled states of up to 14 qubits have been generated (Mon11b).

To determine which state the qubit is in, state readout is performed via the electron-shelving technique (Deh75, Nag86, Sau86). As for the imaging, 397 nm light plus repump light allows for the detection of fluorescence on the $4^2S_{1/2} \leftrightarrow 4^2P_{1/2}$ transition, and indicates which ions are left in the $4^2S_{1/2}$ state. All ions in the $3^2D_{5/2}$ states are not affected by the light fields and remain dark.

All these techniques make trapped ions a very successful system in which to study quantum information processing. The coupling of the ions to a cavity opens the possibility to connect the stationary ion-qubit system with photons, traveling qubits for quantum networks.

2.2 $^{40}\mathrm{Ca}^+$ inside a cavity

Our current ion-cavity system incorporates previous experience with $^{40}\mathrm{Ca}^+$ in CQED experiments. Christian Roos' thesis (Roo00) presents early ideas about the $^{40}\mathrm{Ca}^+$ ion coupled to a cavity. At that time, stably trapped ions presented themselves as ideal probes of a cavity field. Neutral atoms, in comparison, were challenging to confine stationary. Therefore, they were sent flying through microwave or optical resonators, investigating atom-cavity coupling (Goy83, Hei87).

In the first ion-cavity experiments in our research group, the cavity was resonant with the $4^2S_{1/2} \leftrightarrow 3^2D_{5/2}$ quadrupole transition of $^{40}\text{Ca}^+$ (Roo00, Mun03, Kre04a). With such a setup, the reduction of the spontaneous emission lifetime of the $3^2D_{5/2}$ level through the coupling to the cavity field could be shown (Kre04b). However, the coupling rate depends linearly on the atomic multipole moment. Through the weak atomic transition strength of a quadrupole transition, therefore, it is challenging to yield a high coupling rate, which is required for many high-fidelity quantum-network protocols.

The large dipole-transition moments, between the $4^2S_{1/2}$ and 4^2P levels, in contrast, offer access to the highest coupling rates in the $^{40}\text{Ca}^+$ level scheme. Parallel to the research in Innsbruck, these transitions were exploited in Herbert Walther's research group to probe the cavity field with a single ion and show deterministic ion-cavity coupling (Gut01, Kel03). The $4^2S_{1/2} \leftrightarrow 4^2P$ transitions are in the ultra-violet at a wavelength close to 400 nm. At such small wavelengths, it becomes increasingly challenging to produce low-loss mirror coatings, and a high cavity decay rate cannot be avoided, presenting a fundamental technological limit.

The $4^2P \leftrightarrow 3^2D$ transitions also offer large dipole moments but are in the infrared at around 860 nm. At this wavelength, low-loss mirrors are routinely produced. The cavity then couples one of the short-lived 4^2P states with one of the metastable 3^2D states. In this case, three electronic levels are relevant for the system; the two levels that are coupled via the cavity and the $4^2S_{1/2}$ ground state. The $4^2S_{1/2} \leftrightarrow 4^2P$ transition is driven by a laser field, and the $4^2P \leftrightarrow 3^2D$ transition is coupled via the cavity. This scheme describes a cavity-induced Raman transition in which two levels are coupled via a third one. In the pump arm, a photon is absorbed from the laser field, while in the other arm coupled by the vacuum field of the cavity, a photon is emitted. A theoretical description of such a Hamiltonian is presented in Chapter 3.1.2, and a derivation of the Raman process is found in Carlos Russo's thesis (Rus08).

Fig. 2.2 shows the level scheme of this cavity configuration, which we use in our setups. The Raman transition effectively couples the 4^2S and the 3^2D states via a drive field and the cavity. If both cavity and drive laser are detuned from the 4^2P state by the same frequency, population is transferred efficiently from $4^2S_{1/2}$ to 3^2D. In the process, a photon is coherently produced inside the cavity. This Raman process was first used to generate single photons in Herbert Walter's research group (Kel04). In practice, integrating the cavity on the $4^2P \leftrightarrow 3^2D$ transition offers various advantages, such as the possibility of adjusting the effective CQED parameters by detuning the cavity and drive fields (described in (Rus08)) or the possibility of employing a bichromatic driving scheme (described in Chapter 4).

The coating of the cavity mirrors of our setups are optimized at any of the three $4^2P \leftrightarrow 3^2D$ transitions, which have wavelengths of 866 nm, 854 nm, and 850 nm. For all the experiments described in this thesis, the cavity couples the $4^2P_{3/2}$ and the $3^2D_{5/2}$ states, and the $4^2S_{1/2} \leftrightarrow 4^2P_{3/2}$ transition is driven by the pump laser at 393 nm. This Raman process then defines the interaction of the ion with the cavity photon and is exploited as an ion-photon interface in quantum network protocols. The following chapter presents the Hamiltonian of this system together with simulations of quantum network protocols, which have been implemented experimentally in the past two years.

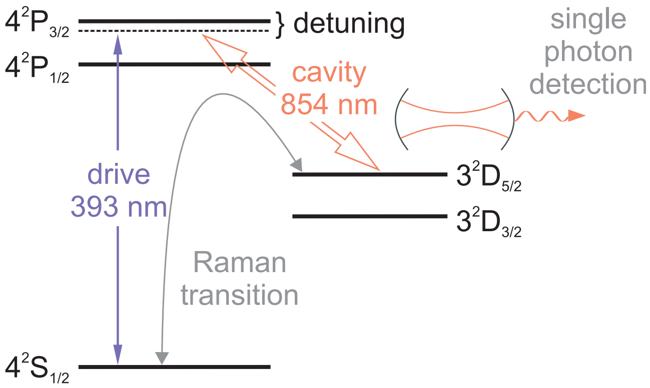

Figure 2.2: ^{40}Ca^{+} level scheme with the cavity-induced Raman transition used for quantum network protocols. A drive laser at 393 nm and the vacuum field of the cavity, which are detuned from the excited state $4^2P_{3/2}$, transfer population from $4^2S_{1/2}$ to $3^2D_{5/2}$ producing a photon inside the cavity. The photon leaves the cavity and is detected by single photon detectors.

3 Simulations of state-mapping and entanglement experiments in a ^{40}Ca^{+}-CQED system

This chapter presents the physical model and the results of simulations of one and two ^{40}Ca^{+} ions inside an optical cavity. The simulations are supporting experiments performed in our laboratory and are important for various reasons. First, they help in understanding the physics of our experiments in detail. Comparing the theory with the data, we learn if the calculations capture the full picture of the experiments, meaning that we understand how the quantum system evolves and interacts with the environment. Second, the simulations provide deeper insight into the dynamics of the experiments and show which parameters are important for optimizing the experimental results. Third, the simulations can be extended to a new set of parameters, providing important information for the system design of a future setup, such as the new fiber-cavity apparatus.

Three experiments performed within the last two years in our group are simulated: quantum-state mapping from an atom to a photon (Stu13), ion-photon entanglement (Stu12c), and two-ion entanglement (Cas13). The experiments are described in detail in the references above and in Andreas Stute's thesis (Stu12a). Therefore, the experiments are only outlined, and the focus lies on the results of the simulations, which are shown to describe our ion-cavity system accurately. Furthermore, the simulations are applied to a range of CQED parameters in reach with the new FFPC setup.

A set of programs to simulate a ^{40}Ca^{+} ion inside a cavity was written by Tracy Northup and Andreas Stute based on earlier code by Carlos Russo. I used these programs and further extended the code to simulate the three experiments mentioned above. The experiments were performed by Andreas Stute, Bernardo Casabone, Konstantin Friebe and Tracy Northup. I contributed to the analysis of the results. In this chapter, parts of Sec. 3.3 and Sec. 3.5 are adapted from (Stu13) and (Cas13), respectively.

3.1 Theoretical treatment of ^{40}Ca^{+} ions inside an optical cavity

Many of the concepts of CQED experiments can be understood with simple two-level or three-level atoms interacting with a single mode of the radiation field inside a cavity. The simplest model for an atom coupled to the light field inside a cavity is given by the Jaynes-Cummings formalism (Jay63). In this model, the atom is treated as an ideal two-level system, while the cavity field is described by a quantized harmonic oscillator.

In our experiments, a drive laser couples a ground state of the ^{40}Ca^{+} ion to an excited state. The cavity couples this excited state to a metastable state. Such a three-level system in a Λ-type configuration enables a cavity-driven Raman transition between the ground and the metastable state and the generation of single photons inside the cavity.

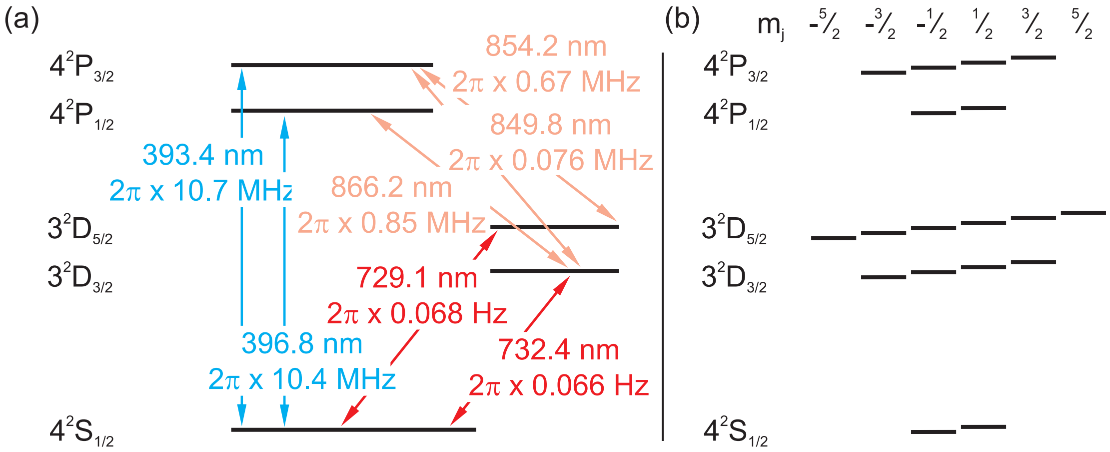

Figure 3.1: Lowest lying levels of ^{40}Ca^{+} with all electronic states that are relevant in our experiments. (a) Wavelengths and half-linewidths, representing the decay rates, of the transitions are taken from (Jin93, Jam98, Bar00) and are included in the scheme. (b) The presence of a magnetic field lifts the degeneracy of states with different magnetic quantum number m_j.

This simple three-level model, however, does not describe our ion-cavity system completely. A realistic model needs to capture all atomic levels that are populated during an experiment and an optical cavity with two orthogonal radiation modes. Furthermore, decoherent processes such as cavity decay, decay of excited atomic states, and finite laser linewidth have to be considered. Such a model, capable of describing the full physics, is presented in this section. The Hamiltonian of this system is derived, and dissipation is introduced, following Andreas Stute's and Kevin Birnbaum's theses (Stu12a, Bir05). Basic physical concepts about the interaction of light and matter inside an optical cavity are found in textbooks such as (CT98, Wal94, Lou73), and a theoretical derivation of decoherence in a quantum system is given in (Car93).

3.1.1 ^{40}Ca^{+}-level scheme

The ^{40}Ca^{+} ion has eighteen electrons bound in closed shells and a nineteenth electron in the valence shell. To describe the atom-light interaction of the calcium ion, it is sufficient to consider the electronic configuration of the valence electron and disregard all other electrons. Fig. 3.1 shows the levels of interest of ^{40}Ca^{+}. The states are labeled by the set of quantum numbers $n^{2\mathrm{s}+1}l_\mathrm{j}$, with the principal quantum number n, the spin multiplicity $2s+1$, the quantum number for orbital angular momentum l, and the total-angular-momentum quantum number j. For simplicity, the state will often only be denoted by l_j. The nuclear spin of the isotope ^{40}Ca is zero.

In the presence of a magnetic field, the degeneracy of states of different magnetic quantum number m_j is lifted, and each l_j manifold splits into $2j+1$ Zeeman states. The magnetic field provides the possibility to address individual transitions between these states. In total, there are eighteen electronic levels of interest.

The drive lasers address the $S_{1/2} \leftrightarrow P_{1/2}$ transition and the $S_{1/2} \leftrightarrow P_{3/2}$ transition, and the cavity couples the two P manifolds to the two D manifolds. If laser and cavity are detuned by the same amount from the transition, population will be transferred coherently from the S to the D manifold in a vacuum stimulated Raman transition, and a photon will be generated in the cavity. There are three possible Raman transitions: $S_{1/2} \leftrightarrow P_{1/2} \leftrightarrow D_{3/2}$, $S_{1/2} \leftrightarrow P_{3/2} \leftrightarrow D_{3/2}$ and $S_{1/2} \leftrightarrow P_{3/2} \leftrightarrow D_{5/2}$. The Raman transition $S_{1/2} \leftrightarrow P_{3/2} \leftrightarrow D_{5/2}$ coupling the qubit states is used for all experiments described in this thesis.

3.1.2 Hamiltonian

The Hamiltonian presented in the following describes a ^{40}Ca$^+$ ion that interacts with two degenerate, orthogonal modes of a resonator. All other modes of the resonator are separated in frequency from these modes and thus are neglected. The atom is driven by semi-classical external fields and experiences a magnetic field. An external field driving the cavity would be another possibility to drive the system. In all of the experiments described here, however, only the atom is driven. Therefore, a cavity drive is not included in the model. This term can be found in textbooks such as (Wal94).

The Hamiltonian can be written as the sum of the bare-atom and cavity Hamiltonian $\hat{H}_0$, the atom-cavity interaction $\hat{H}_{\text{atom-cavity}}$, the atom-laser interaction $\hat{H}_{\text{atom-laser}}$, and the magnetic field Hamiltonian $\hat{H}_{\text{B}}$. The individual terms are described below in detail.

$$\hat{H} = \hat{H}_0 + \hat{H}_{\text{atom-cavity}} + \hat{H}_{\text{atom-laser}} + \hat{H}_{\text{B}} \tag{3.1}$$

The ion is driven by a laser at frequency ω_{d}, and the Hamiltonian is described in a frame which rotates at this drive-laser frequency (Raman interaction picture). Only the parts $\hat{H}_0$ and $\hat{H}_{\text{atom-laser}}$ of the Hamiltonian are affected by this transformation to the rotating frame (see textbooks such as (Lou73)). Furthermore, the dipole approximation is used for all atom-field interactions. In the following, $\hbar = 1$, which means that energy has the same dimension as frequency.

1. **The bare-atom and the bare-cavity Hamiltonian $\hat{H}_0$**

   This part of the Hamiltonian describes the uncoupled cavity modes and the atomic levels of the ^{40}Ca$^+$ ion. The energy reference of the system is set to the $P_{3/2}$ state. The cavity supports two orthogonal cavity modes with photons of frequency ω_{c}. Using the annihilation and creation operators for the two linearly polarized electromagnetic field modes of the resonator ($\hat{a}$, $\hat{a}^\dagger$, $\hat{b}$, and $\hat{b}^\dagger$), the Hamiltonian is

$$\hat{H}_0 = \underbrace{\sum_{l_{\text{j}}} \Delta_{\text{l}_\text{j}} \hat{\sigma}_{\text{l}_\text{j};\text{l}_\text{j}}}_{\text{atom}} - \underbrace{\omega_{\text{d}} \hat{\sigma}_{\text{S}_{1/2};\text{S}_{1/2}}}_{\text{transformation}} + \underbrace{\omega_{\text{c}}(\hat{a}^\dagger \hat{a} + \hat{b}^\dagger \hat{b})}_{\text{cavity}} \tag{3.2}$$

   where l_{j} stands for all relevant orbital angular momentum states $S_{1/2}$, $P_{1/2}$, $P_{3/2}$, $D_{3/2}$, and $D_{5/2}$, and $\Delta_{\text{l}_\text{j}} = E_{l_\text{j}} - E_{P_{3/2}}$ gives the energy of each level. The operator $\hat{\sigma}_{\text{l}_\text{j};\text{l}_\text{j}} = |l_{\text{j}}\rangle\langle l_{\text{j}}|$ is the projector of the state $|l_{\text{j}}\rangle$. The term $\omega_{\text{d}} \hat{\sigma}_{\text{S}_{1/2};\text{S}_{1/2}}$ adds additional energy to the $S_{1/2}$ states and arises from the transformation to the Raman interaction picture.

2. **The atom-cavity interaction Hamiltonian $\hat{H}_{\text{atom}-\text{cavity}}$**

   The cavity couples the $P_{3/2}$ states to the $D_{5/2}$ states. The atomic dipole operators for these transitions are defined as

$$\hat{D}_{\text{q;PD}} = \sum_{m_{\text{j}}=-\frac{5}{2}}^{\frac{5}{2}} |D_{5/2}, m_{\text{j}}\rangle\langle D_{5/2}, m_{\text{j}}|\mu_{\text{q}}|P_{3/2}, m_{\text{j}} + q\rangle\langle P_{3/2}, m_{\text{j}} + q| \tag{3.3}$$

   where $q = \{-1, 0, 1\}$, and μ_{q} is the dipole operator for σ^{-}-, π-, and σ^{+}-transitions. The matrix elements $\langle D_{5/2}, m_{\text{j}}|\mu_{\text{q}}|P_{3/2}, m_{\text{j}} + q\rangle$ are the Clebsch-Gordan coefficients that describe the geometric component of the transition amplitudes.

   The quantization axis of the system is determined by the direction of the magnetic field, which is orthogonal to the cavity axis. The polarization of the mode corresponding to $\hat{a}^{\dagger}$ is defined to lie along the quantization axis, and the mode drives π-transitions in the atom. Positive and negative circularly polarized light drives the σ^{+}- and σ^{-}-transitions. Of this circularly polarized light, only the component with the wave vector along the cavity axis couples to the cavity. Therefore, the cavity mode corresponding to $\hat{b}^{\dagger}$ drives these σ transitions with $1/\sqrt{2}$ of the coupling strength. The atom-cavity interaction Hamiltonian is then:

$$\begin{aligned}\hat{H}_{\text{atom}-\text{cavity}} = & \underbrace{g_0(\hat{a}^{\dagger}\hat{D}_{0;\text{PD}} + \hat{D}^{\dagger}_{0;\text{PD}}\hat{a})}_{\pi\text{-transitions}} \\ & \underbrace{+ g_0\left(\frac{1}{\sqrt{2}}\hat{b}^{\dagger}(\hat{D}_{-1;\text{PD}} + \hat{D}_{+1;\text{PD}}) + \frac{1}{\sqrt{2}}(\hat{D}^{\dagger}_{-1;\text{PD}} + \hat{D}^{\dagger}_{+1;\text{PD}})\hat{b}\right)}_{\sigma^{+}\text{-, }\sigma^{-}\text{transitions}}.\end{aligned} \tag{3.4}$$

   The terms $\hat{a}^{\dagger}\hat{D}_{\text{q;PD}}$ and $\hat{b}^{\dagger}\hat{D}_{\text{q;PD}}$ correspond to a photon being generated in the cavity and the atom changing to the $D_{5/2}$ state. Accordingly, the terms $\hat{D}^{\dagger}_{\text{q;PD}}\hat{a}$ and $\hat{D}^{\dagger}_{\text{q;PD}}\hat{b}$ correspond to a photon being absorbed from the cavity and the atom changing to the $P_{3/2}$ state. In dipole approximation, the coherent atom-cavity coupling rate g_0 is

$$g_0 = \sqrt{\frac{3c\gamma\lambda^2}{Lw_0^2\pi^2}} \tag{3.5}$$

   for a cavity of length L and mode waist w_0. The transition addressed via the cavity has a wavelength of λ and a half linewidth of γ. c is the speed of light in vacuum.

   Using z as the cavity axis, the intensity profile of the Gaussian TEM$_{00}$ mode of the cavity field is

$$I(x, y, z) = I_0 e^{\frac{-(x^2+y^2)}{2w_0^2}} \sin^2\left(\frac{2\pi z}{\lambda}\right). \tag{3.6}$$

   The ion-cavity coupling g has the maximum value g_0 when the ion is positioned at the waist of the cavity in an antinode of the standing wave, where the amplitude of the electromagnetic field has its maximum value. It decreases as the ion is shifted from this position.

3. **The atom-laser interaction Hamiltonian $\hat{H}_{\text{atom}-\text{laser}}$**

   The atom-laser interaction is treated in a semi-classical way. The Hamiltonian describes classical fields which drive the atom. The light field of the drive laser is described by a coherent state. The amplitude is high, such that absorption or emission of a single photon does not change the state (Gla63), and the field operator is approximated by its expectation value. Lasers on the $S_{1/2} \leftrightarrow P_{3/2}$ transition drive the Raman transition.

   To address two Raman transitions simultaneously, we use a bichromatic field of frequencies $\omega_1 = \omega_{\text{d}}$ and ω_2 and Rabi frequencies Ω_1 and Ω_2.

$$\hat{H}_{\text{atom}-\text{laser}} = (\Omega_1 + \Omega_2 e^{i(\omega_2-\omega_1)t})(\hat{D}_{\text{q;SP}} + \hat{D}^{\dagger}_{\text{q;SP}})/2 \tag{3.7}$$

   using analogous dipole operators for the $S_{1/2} \leftrightarrow P_{3/2}$ transition as for the $P_{3/2} \leftrightarrow D_{5/2}$ transition above (Eq. 3.3). In the interaction picture, the coupling terms of the drive laser at frequency $\omega_{\text{d}} = \omega_1$ are time independent, while the terms of the drive laser that has the frequency ω_2 rotate at the difference frequency of the two components of the field $\omega_2 - \omega_1$.

   As the experiments described in this thesis end when the electronic population of the ion is in either of the two D manifolds, a repump field is not needed in the simulations. The interaction terms for the monochromatic repump fields from the $D_{3/2}$ and $D_{5/2}$ states to the $P_{1/2}$ and $P_{3/2}$ states are therefore not written out here.

4. **The magnetic field Hamiltonian $\hat{H}_{\text{B}}$**

   An external magnetic field B shifts the energy of the individual Zeeman states proportionally to the Landé factor g_{j} and the projection of the angular momentum m_{j}. Each orbital angular momentum state $S_{1/2}$, $P_{1/2}$, $P_{3/2}$, $D_{3/2}$, and $D_{5/2}$ is split into $2j+1$ substates. For each of those states described by the quantum numbers $(l_{\text{j}}, m_{\text{j}})$ the Zeeman energy level shift is calculated via

$$\hat{H}_{\text{B}} = \sum_{l_{\text{j}},m_{\text{j}}} B\mu_{\text{B}} g_{\text{j}} m_{\text{j}} \hat{\sigma}_{\text{l}_\text{j},\text{m}_\text{j};\text{l}_\text{j},\text{m}_\text{j}} \tag{3.8}$$

   with μ_{B} the Bohr magneton. Here, the projectors to the individual Zeeman states are used: $\hat{\sigma}_{\text{l}_\text{j},\text{m}_\text{j};\text{l}_\text{j},\text{m}_\text{j}} = |l_{\text{j}}, m_{\text{j}}\rangle\langle l_{\text{j}}, m_{\text{j}}|$.

3.1.3 Dissipation

Processes which cause dissipation are included in the theoretical model by treating the system as an open quantum system, interacting weakly with its environment. The dissipative processes in the system are spontaneous emission of the atom, decay of the cavity, and a nonzero linewidth of the drive lasers. Mathematically, they are described by the collapse operators, as shown in the following for the relevant processes of our system.

1. **Spontaneous emission of the atom**

   Populations in the electronic states $P_{1/2}$, $P_{3/2}$, $D_{3/2}$, and $D_{5/2}$ decay at rates $2\gamma_{\mathrm{l_j}}$. The atom emits a photon into the environment and is projected to the final state of the decay. The collapse operator for each decay can be written as

   $$\hat{\mathcal{C}}_{\mathrm{atom}} = \sqrt{2\gamma_{\mathrm{l_j}}}\ \hat{D}_{\mathrm{q;if}}, \tag{3.9}$$

   with the dipole operator $\hat{D}_{\mathrm{q;if}}$ for the initial and the final states of the decay. The decay rates $2\gamma_{\mathrm{l_j}}$ are given in Fig. 3.1.

2. **Decay of the cavity mode**

   The intensity of the cavity field decays at a rate 2κ. This dissipative process removes single photons from the cavity. The collapse operator for each mode $\hat{a}$ and $\hat{b}$ is

   $$\hat{\mathcal{C}}_{\mathrm{cavity,a}} = \sqrt{2\kappa}\ \hat{a} \tag{3.10}$$

   $$\hat{\mathcal{C}}_{\mathrm{cavity,b}} = \sqrt{2\kappa}\ \hat{b} \tag{3.11}$$

3. **Laser phase noise**

   The finite linewidth δ of the drive lasers introduces a phase noise. This is described via the collapse operator:

   $$\hat{\mathcal{C}}_{\mathrm{laser}} = \delta\ \hat{\sigma}_{S_{1/2};S_{1/2}} \tag{3.12}$$

   At the rate of the linewidth, the $S_{1/2}$ state is projected onto itself, thus destroying phase coherence (Car93).

The dynamics of the CQED system is determined by the three parameters g, κ and γ. Carlos Russo gives a detailed description of three parameter regimes in his thesis (Rus08). The case where the coherent evolution is dominant over the incoherent decay mechanisms $g \gg \kappa, \gamma$ is called the strong coupling regime. For the cases where $\kappa \gg g, \gamma$ (bad cavity limit) and $\gamma \gg g, \kappa$ (bad atom limit) dissipation dominates the system dynamics.

3.1.4 Multiple atoms

When two or more atoms are coupled to the cavity, the Hamiltonian is expanded by summing over all n atoms. The bare-atom bare-cavity Hamiltonian $\hat{H}_{0,\mathrm{n}}$ for n atoms then takes the form

$$\hat{H}_{0,\mathrm{n}} = \sum_{i=1}^{n} \sum_{l_{\mathrm{j}}} \Delta_{\mathrm{l_j}} \hat{\sigma}_{\mathrm{l_j,i;l_j,i}} - \sum_{i=1}^{n} \omega_{\mathrm{d}} \hat{\sigma}_{\mathrm{S_{1/2},i;S_{1/2},i}} + \omega_{\mathrm{c}}(\hat{a}^{\dagger}\hat{a} + \hat{b}^{\dagger}\hat{b}). \tag{3.13}$$

The projection operator of the atom i to the state $|l_{\mathrm{j}}\rangle$ is given by $\hat{\sigma}_{\mathrm{l_j,i;l_j,i}}$. The other Hamiltonian terms and the decay terms take analogue forms.

In our system, we have the ability to move the ions with respect to the cavity mode (Cas13). Therefore, the coupling constant g_0 is decreased to g as the ion is moved out of the cavity waist and the antinode of the cavity field. This effective coupling can be different for each ion.

3.2 Outline of the simulations

The simulations are based on the Quantum Optics Toolbox for Matlab (Tan99). Two techniques used to calculate the non-unitary evolution of the ion-cavity system, the master-equation formalism and the Monte Carlo method, are described below.

The Hamiltonian of the bichromatic drive field (Eq. 3.7) has an explicit time dependence, and the experiments that we wish to simulate are time-dependent problems. As a consequence, it is not possible to calculate steady-state solutions. While the master-equation formalism calculates the system density matrix as a function of evolution time, the Monte Carlo method mimics one probabilistic outcome of the experiment for each calculated trajectory. For the two-ion entanglement simulations (Sec. 3.5), it is convenient to have such probabilistic time information of the system decay terms. Therefore, this problem was simulated with the Monte Carlo method. For the state-mapping experiment (Sec. 3.3) and the ion-photon entanglement experiment (Sec. 3.4), this information was not required, and the master-equation formalism was used as the most convenient method.

3.2.1 Master-equation formalism

In the master-equation formalism (Car93, Gar04), the system is coupled to a reservoir of empty modes. Assuming that the environment has no memory (Markov approximation), that the interaction with the environment is weak (Born approximation), and that the initial states of the system and the environment are not correlated (product initial state assumption), the master equation for the system density matrix ρ is written as:

$$\dot{\rho} = \mathcal{L}\rho \tag{3.14}$$

with $\mathcal{L}$ the Liouvillian superoperator. The superoperator introduces incoherent processes into the system: phase randomization and the dissipation of energy to the environment. The Liouvillian superoperator combines the Hermitian Hamiltonian and the decay terms,

$$\mathcal{L}\rho = -i[\hat{H}, \rho] + \mathcal{L}_{\text{diss}}\rho. \tag{3.15}$$

The dissipative term in the Liouvillian $\mathcal{L}_{\text{diss}}$ contains the sum of all dissipation channels $\mathcal{L}_{\text{diss}} = \mathcal{L}_{\text{atom}} + \mathcal{L}_{\text{cavity}} + \mathcal{L}_{\text{laser}}$. The decay superoperator $\mathcal{L}_{\text{diss}}$ is written in the Lindblad form as the sum of the collapse superoperators

$$\mathcal{L}_{\text{diss}}\rho = \frac{1}{2}\sum_{\text{m}}(2\hat{\mathcal{C}}_{\text{m}}\rho\hat{\mathcal{C}}_{\text{m}}^{\dagger} - \hat{\mathcal{C}}_{\text{m}}^{\dagger}\hat{\mathcal{C}}_{\text{m}}\rho - \rho\hat{\mathcal{C}}_{\text{m}}^{\dagger}\hat{\mathcal{C}}_{\text{m}}), \tag{3.16}$$

which act on the density matrix ρ of the system. The sum over m indicates the sum over all decay terms: $\hat{\mathcal{C}}_{\text{atom}}$, $\hat{\mathcal{C}}_{\text{cavity}}$ and $\hat{\mathcal{C}}_{\text{laser}}$.

With an initial condition $\rho(0) = \rho_0$, it is possible to calculate the evolution of the system by integrating the master equation (Eq. 3.14) numerically to determine the system density matrix $\rho(t)$ at time t. From $\rho(t)$, expectation values of particular observables are calculated via the trace:

$$\langle \hat{o} \rangle = \mathrm{Tr}(\hat{o}\rho(t)), \tag{3.17}$$

for any operator $\hat{o}$. Observables of interest are ion-state populations, which are calculated via projection operators onto those states $\hat{\sigma}^\dagger_{\mathrm{l_j}}\hat{\sigma}_{\mathrm{l_j}}$, or the temporal evolution of photons exiting the cavity, calculated via the number operators $\hat{a}^\dagger\hat{a}$ and $\hat{b}^\dagger\hat{b}$.

In our Matlab code, the core routine of the program calculates the Liouvillian function of the CQED system. This Liouvillian function is called by higher-level simulation programs for specific problems. These simulation programs also call two separate routines which specify the input parameters for a given simulation. The first routine stores all experimental parameters, including drive-laser and repump-laser parameters, the CQED-system parameters g, and κ, the magnetic field, and the detection-path efficiency. In the second routine, the user determines the simulation parameters: the Hilbert space (and thus the Fock-state number), the numerical-integration parameters, and the initial density matrix, including the atomic input state. In our experiments each ion produces one or no photon in the cavity. For experiments with one ion, therefore, the Fock-state number is two for each cavity mode: no photon in the mode and one photon in the mode.

3.2.2 Monte Carlo method

In the presence of decay mechanisms, the wave function of the system collapses with a probability determined by the decay rate. The Monte Carlo method accounts for these collapse events by calculating a continuous evolution of the Schrödinger equation which is modified by the decay terms, allowing for quantum jumps. The modified Schrödinger equation with the state vector $\psi(t)$ reads

$$\dot{\psi} = -i\hat{H}_{\mathrm{eff}}\psi \tag{3.18}$$

with the effective, non-Hermitian Hamiltonian $\hat{H}_{\mathrm{eff}}$. It is calculated via the Hermitian Hamiltonian $\hat{H}$ and the collapse operators $\hat{\mathcal{C}}_{\mathrm{m}}$:

$$\hat{H}_{\mathrm{eff}} = \hat{H} - \frac{i}{2}\sum_m \hat{\mathcal{C}}^\dagger_{\mathrm{m}}\hat{\mathcal{C}}_{\mathrm{m}}. \tag{3.19}$$

Given the initial condition $\psi(0) = \psi_0$, the state $\psi(t)$ at time t is calculated. In contrast to the master-equation formalism, one Monte Carlo trajectory mimics the evolution of one experimental cycle with probabilistic decays. Observables are calculated by applying the operator of interest to $\psi(t)$, yielding a measurement result. Many trajectories of the same system are calculated, and an average over all measurement results gives an expectation value of the operator. In this respect, the Monte Carlo method is analogous to experiments in which expectation values are measured by averaging over a large set of individual measurement results.

A routine written in C, which is part of the quantum optics toolbox, carries out the Monte Carlo simulation, with the effective Hamiltonian and the initial condition specified by the Matlab routine.

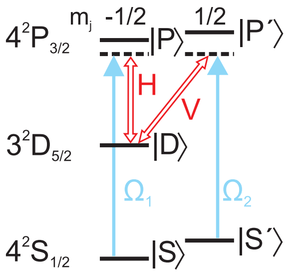

Figure 3.2: Diagram for the atom-photon state-mapping experiment (Stu13). The reduced $^{40}\mathrm{Ca}^+$ level scheme indicates the relevant levels. A coherent superposition of the $|S\rangle$ and $|S'\rangle$ is mapped onto a coherent superposition of the horizontal (H) and vertical (V) polarization of a cavity photon. Two Raman fields with Rabi frequencies Ω_1 and Ω_2 drive the transitions from the $4^2S_{1/2}$ states to $|D\rangle$ via the excited states $|P\rangle$ and $|P'\rangle$, generating the photon inside the cavity.

These simulation techniques are applied to simulate three experiments presented in the following.

3.3 Mapping a quantum state from an ion to a photon

In quantum networks (Kim08), quantum information needs to be transferred coherently between distant nodes. In our system, the trapped ion constitutes a node, and distant nodes would be connected via photonic channels. The cavity represents the interface between ion and photon. The state-mapping protocol introduced by Ignacio Cirac and colleagues (Cir97) allows a reliable transfer of quantum states among spatially distant ions and thus enables distributed quantum information processing and quantum communication in the network.

In an experiment performed in 2012 (Stu13), we have realized the deterministic transfer of a quantum state of an ion onto a cavity photon. Quantum information stored in the electronic state of the ion is transferred to the polarization of a cavity photon. Using the polarization degree of freedom as a qubit, in contrast to encoding the information in the photon number, makes the protocol robust against the loss of single photons. The bichromatic driving scheme provides the possibility to select any two final states in the level scheme. Furthermore, the phase of the generated photon state is independent of the detection time, which permits us to characterize the interplay between efficiency and fidelity of the CQED system in the presence of decoherence.

This section describes simulations of the atom-photon state-mapping and compares them with the experimental results from Ref. (Stu13).

3.3.1 Ion-photon state-mapping protocol

The goal of state mapping is to transfer the quantum state of an ion coherently to the state of a photon. The ion's quantum state is stored in a superposition of the electronic states $|S\rangle \equiv |4^2S_{1/2}, m_\mathrm{j} = -1/2\rangle$ and $|S'\rangle \equiv |4^2S_{1/2}, m_\mathrm{j} = 1/2\rangle$, whereas the photonic qubit is encoded in the polarization states $|H\rangle$ and $|V\rangle$ corresponding to the horizontally and vertically polarized modes of the cavity. The Zeeman states are split by a magnetic field orthogonal to the cavity axis. In this mapping process, the cavity acts as the interface that transfers the information, leaving the ion in the third electronic state $|D\rangle \equiv |3^2D_{5/2}, m_{\mathrm{j}} = -1/2\rangle$. Mathematically, the state mapping is written as:

$$\left(\cos\alpha|S\rangle + e^{i\varphi}\sin\alpha|S'\rangle\right) \otimes |0\rangle \longrightarrow |D\rangle \otimes \left(\cos\alpha|H\rangle + e^{i\varphi}\sin\alpha|V\rangle\right). \tag{3.20}$$

$|0\rangle$ is the vacuum state of the cavity. After the mapping, no information is left in the ion, whereas the superposition's amplitude α and phase φ are preserved in the photonic state, as indicated in Fig. 3.2. A phase-stable bichromatic field drives two Raman transitions from $|S\rangle$ and $|S'\rangle$ to $|D\rangle$ via the two intermediate states $|P\rangle \equiv |4^2P_{3/2}, m_{\mathrm{j}} = -1/2\rangle$ and $|P'\rangle \equiv |4^2P_{3/2}, m_{\mathrm{j}} = 1/2\rangle$. In free space, the $|S\rangle$ to $|D\rangle$ transition generates a π-polarized photon. This photon coincides with the horizonal mode of the cavity. The σ^--polarized photon that is generated in the $|S'\rangle$ to $|D\rangle$ transition is projected onto the vertical mode of the cavity. The photon is circularly polarized with respect to the magnetic field direction, and only half of this mode couples to the vertically polarized mode of the cavity. As a consequence, the coupling strength of the cavity-induced σ^- transition is a factor of $\sqrt{2}$ weaker than the π transition. The analogue effect holds for the σ^+ transition. Therefore, the terms in Eq. 3.4, which describe the σ^- and σ^+ transitions, are multiplied by the term $\sqrt{1/2}$.

The Clebsch-Gordan coefficient of the $|P\rangle \leftrightarrow |D\rangle$ transition is $-\sqrt{2/5}$, and the coefficient of the $|P'\rangle \leftrightarrow |D\rangle$ transition is $-\sqrt{1/5}$. Setting the relative Rabi frequencies to $\Omega_2 = 2\Omega_1$ compensates for the different Clebsch-Gordan coefficients and couplings to the cavity mode, such that both Raman transitions have equal strength.

Process fidelity

The quality of the mapping process is characterized via process tomography (Jam01). Process tomography extracts the process matrix χ, which parameterizes the map from an arbitrary input density matrix ρ_{in} to its corresponding output state ρ_{out} in the basis of the Pauli operators $\sigma_{0,1,2,3} \equiv \{\mathbb{1}, \sigma_{\mathrm{x}}, \sigma_{\mathrm{y}}, \sigma_{\mathrm{z}}\}$:

$$\rho_{\mathrm{out}} = \sum_{i,j} \chi_{\mathrm{ij}}\sigma_{\mathrm{i}}\rho_{\mathrm{in}}\sigma_{\mathrm{j}}. \tag{3.21}$$

As the ideal mapping process preserves the qubit, the overlap χ_{00} with the identity should be equal to one. We identify χ_{00} as the process fidelity, which quantifies the success of the mapping.

The mapping process is analyzed for four different initial states. For each input state, the single photon that is generated inside the cavity in the mapping process is coupled out and measured via state tomography.

State tomography is used to reconstruct the density matrix ρ of a quantum state. It characterizes an ensemble of identically prepared quantum systems (Jam01). For a single-qubit system, ρ has three free parameters that can be determined via measuring the expectation values of the Pauli operators σ_{x}, σ_{y}, and σ_{z}. Measuring in three settings thus completely defines ρ. To perform state tomography on the photon, its polarization is measured in each of the three orthogonal bases, H/V, D/A, and R/L. Here, the bases

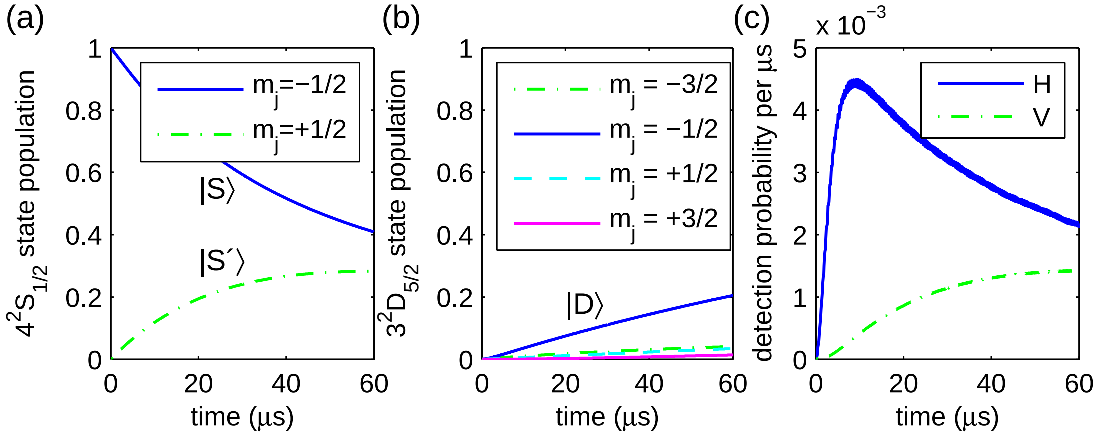

Figure 3.3: Simulated state mapping of $|S\rangle$ to $|H\rangle$. (a) Population of the $4^2S_{1/2}$ manifold and (b) the $3^2D_{5/2}$ manifold as a function of the interaction time. (c) Temporal shapes of the horizontally and the vertically polarized cavity photons. At $t = 0$, the ion is in $|S\rangle$, and no population is in $|S'\rangle$. The Raman field drives a transition to the state $|D\rangle$. While the population in $|S\rangle$ decreases, the population in $|D\rangle$ increases, and a horizontally polarized photon is produced. Over time, off-resonant excitation to the $4^2P_{3/2}$ manifold followed by spontaneous decay leads to a gradual increase in the population of the state $|S'\rangle$ and an increased probability to produce a vertically polarized photon.

are defined as antidiagonal polarization $A = (H - V)/\sqrt{2}$, diagonal polarization $D = (H + V)/\sqrt{2}$, right-circular polarization $R = (H + iV)/\sqrt{2}$, and left-circular polarization $L = (H - iV)/\sqrt{2}$.

3.3.2 State-mapping simulations

The simulations are carried out via the master-equation formalism. Starting with a specific initial state of the ion, the simulation calculates the ion's electronic state and the photon's polarization leaving the cavity as a function of time. Here, the state-mapping process is analyzed for the two input states $|S\rangle$ and $|S - S'\rangle$. The simulations are implemented with the following parameters: $g = 2\pi \times 0.9$ MHz, $\kappa = 2\pi \times 50$ kHz, magnetic field amplitude $B = 4.5$ G, cavity detuning of -400 MHz from the $|D\rangle \leftrightarrow |P\rangle$ transition, and Rabi frequency of the drive field $\Omega_{\text{tot}} = \sqrt{\Omega_1^2 + \Omega_2^2} = 2\pi \times 18$ MHz. The simulation assumes a detection-path efficiency without losses. To compare the simulations to the experimental data, these losses are introduced afterwards as a scaling factor.

Mapping $|S\rangle$ to $|H\rangle$

A simulation that maps the electronic state $|S\rangle$ of the ion to a photon in the state $|H\rangle$ is shown in Fig. 3.3. At the beginning of the process, the population of the ion is in $|S\rangle$. The bichromatic Raman field drives the transition to $|D\rangle$. Thus, the population of $|D\rangle$ increases over time as the population in $|S\rangle$ decreases; see Fig. 3.3(a) and (b). In

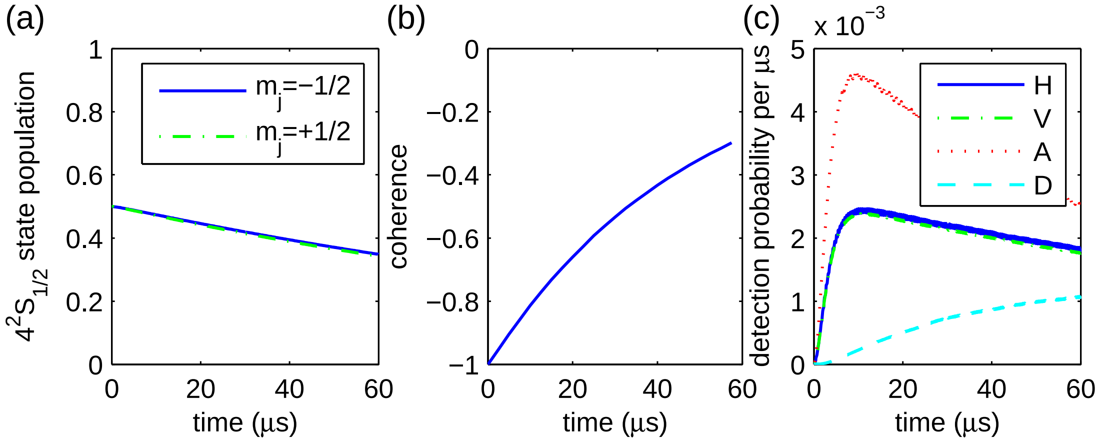

Figure 3.4: Simulation of the transfer of $|S - S'\rangle$ to $|A\rangle$. (a) Population in $|S\rangle$ and $|S'\rangle$ as a function of time. (b) Coherence of the superposition state $|S - S'\rangle$. (c) Probability of detecting a photon in $|H\rangle/|V\rangle$ and in $|A\rangle/|D\rangle$ as a function of time.

this process, a photon is produced. Fig. 3.3(c) shows the probability per microsecond to detect a horizontally or a vertically polarized photon as a function of time.

In an ideal process, only the target state $|D\rangle$ of the Zeeman manifold $D_{5/2}$ is populated. However, off-resonant excitation in the $P_{3/2}$ manifold and subsequent spontaneous decay slowly populate the rest of the $D_{5/2}$ manifold, as seen in Fig. 3.3(b). In case of such a spontaneous decay, no photon is produced in the cavity mode. Therefore, this effect does not compromise the fidelity of the mapping process and only decreases its efficiency.

After an off-resonant excitation, however, spontaneous decay of the ion to the $S_{1/2}$ manifold is sixteen times more likely than the decay to the $D_{5/2}$ manifold. A decay to the $S_{1/2}$ manifold leads to an increase of the population in $|S'\rangle$ over time. This state is also driven by the bichromatic Raman field, resulting in a vertically polarized photon inside the cavity. Thus, the probability to produce a $|V\rangle$ photon increases over time; see Fig. 3.3(c). As a result, with increasing detection time, it becomes less likely that the mapping process achieves its target result, i.e, the process fidelity decreases.

Mapping $|S - S'\rangle$ to $|H - V'\rangle$

A second simulation, in which the electronic superposition state $|S - S'\rangle$ is transferred to the polarization state $|A\rangle$ is shown in Fig. 3.4. At time $t = 0$, all electronic population is in $|S\rangle$ and $|S'\rangle$ (Fig. 3.4(a)) and distributed equally between the states. The coherence of the superposition state $|S - S'\rangle$ is maximum, where the coherence (Fig. 3.4(b)) of the electronic state is given by the density matrix element $\rho_{\mathrm{S,S'}} + \rho_{\mathrm{S',S}}$. As the Raman field drives the ion to $|D\rangle$, a photon in the state $|A\rangle$ is produced.

In this configuration, off-resonant excitation followed by spontaneous decay to the $S_{1/2}$ manifold does not change the balance of the population of the states $|S\rangle$ and $|S'\rangle$, resulting in the production of horizontally and vertically polarized photons with equal probability throughout the experiment (Fig. 3.4(c)). However, the decay destroys the coherence of the superposition state, which is shown in Fig. 3.4(b). As a consequence,

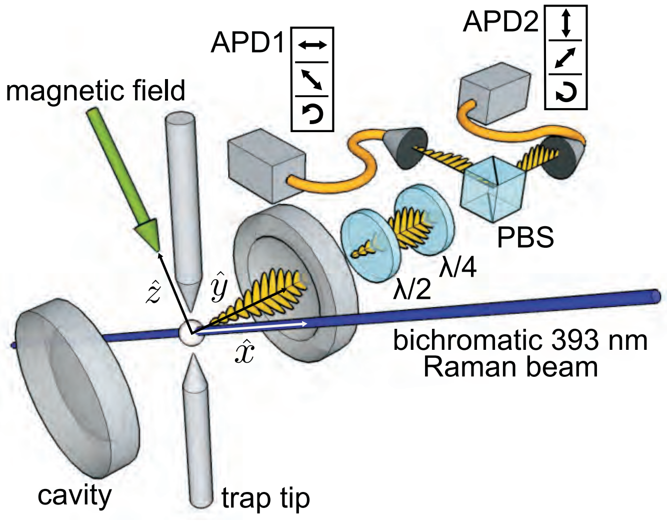

Figure 3.5: Experimental configuration of the state-mapping experiment. A Paul trap indicated by the trap tips confines the ion. It sits in an antinode of the cavity field and is driven by the bichromatic Raman field, generating single cavity photons. A magnetic field orthogonal to the Raman field defines the quantization axis and lifts the degeneracy of the Zeeman states. The photons exit the cavity, and their polarization is analyzed with waveplates ($\lambda/2$, $\lambda/4$) and a polarizing beamsplitter (PBS). Avalanche photodiodes (APD1, APD2) detect the photon. The polarization measurement basis is set by the waveplates and indicated in the tables at the APDs. Image reproduced from (Stu13).

while only anti-diagonally polarized photons should be produced, over time, the probability to produce diagonally polarized photons rises (Fig. 3.4(c)).

In the diagonal/antidiagonal basis, the result of the mapping sequence is analogous to the sequence before, in which $|S\rangle$ was mapped to $|H\rangle$; at the beginning, the probability to produce the correct photon $|A\rangle$ is high. Due to the decay process, the probability to produce $|D\rangle$ rises with time.

3.3.3 Experimental results

The experiment is performed with the apparatus that was set up by Carlos Russo (Rus08). Fig. 3.5 shows the experimental configuration. The ion is confined via the Paul trap, indicated schematically by two tip electrodes, and sits in an antinode of the cavity. A magnetic field of 4.5 G along $\hat{z}$ lifts the degeneracy of the Zeeman states. The cavity axis is oriented along the $\hat{y}$-axis, and the Raman beam enters along the $\hat{x}$-axis. The cavity and the drive field are detuned from the $P_{3/2}$ states by approximately -400 MHz. An optical setup of waveplates, polarization beam splitters, and avalanche photodiodes (APDs) is used to perform state tomography of the photons.

Experimentally, the four input states $|S\rangle$, $|S'\rangle$, $|S\rangle - |S'\rangle$, and $|S\rangle + i|S'\rangle$ are prepared via optical pumping to $|S\rangle$ followed by a laser pulse that transfers population from $|S\rangle$ to the $|3^2D_{5/2}, m_\mathrm{j} = -3/2\rangle$ level. The length and the phase of this pulse set the amplitude

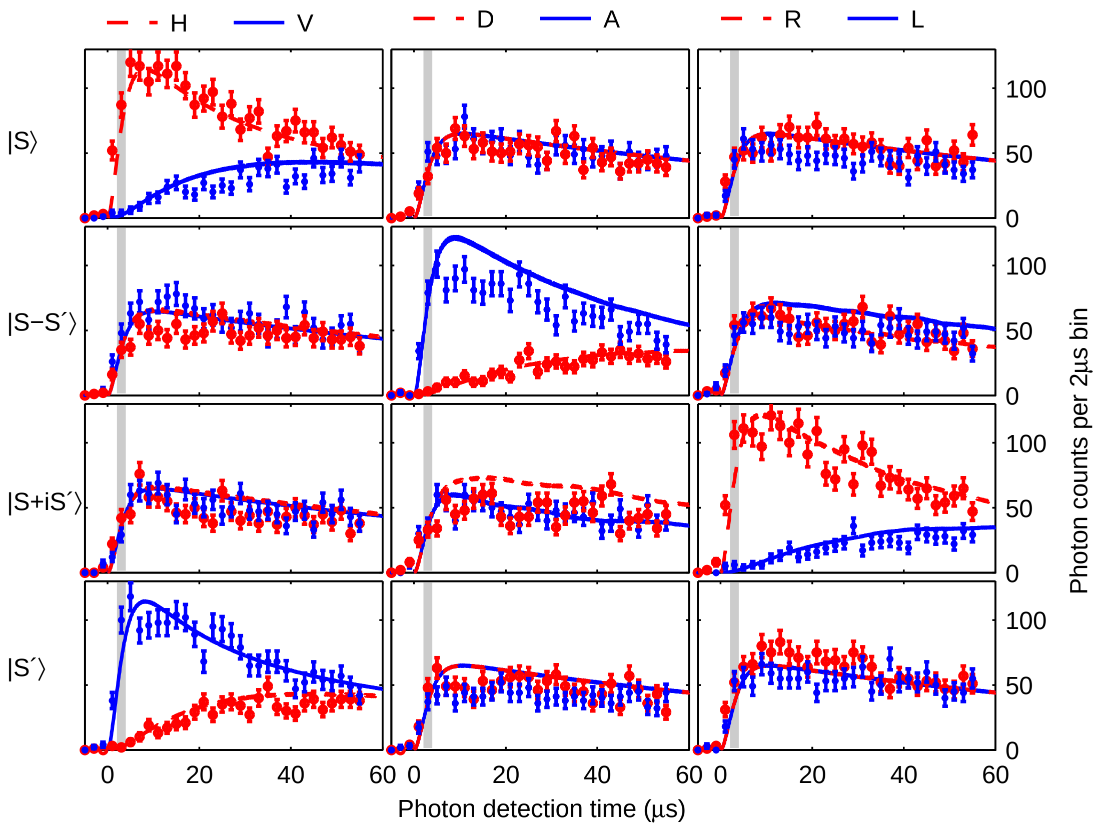

Figure 3.6: Temporal shape of the photons for the state-mapping experiment with the four different input states $|S\rangle$, $|S - S'\rangle$, $|S + iS'\rangle$, and $|S'\rangle$. The graphs show the photon counts per 2 µs time bin as a function of the time at which the photon was detected on an APD. The photon's polarization is analyzed in the three bases H/V, D/A, and R/L. The grey shaded area marks the time bin used to extract the maximum process fidelity. Error bars represent one standard deviation. The simulation results (solid and dashed lines) reproduce the experimental data. Image reproduced from (Stu13).

and the phase of the initial state. Subsequently, the population in $|3^2D_{5/2}, m_\mathrm{j} = -3/2\rangle$ is coherently transferred to $|S'\rangle$.

To characterize the mapping process, for each of the four input states, the polarization of the output photon is measured via state tomography, which corresponds to measurements in the three polarization bases H/V, D/A, and R/L. Fig. 3.6 shows the state tomography data of the photon polarization for each input state for all three polarization bases measurements. The mapping process is analyzed for a Raman drive time of 55 µs. The temporal shapes of the twelve single photons constitute the raw data for the process tomography.

The row one of Fig. 3.6 shows the map of $|S\rangle$ to $|H\rangle$. The ideal process would produce a polarized photon in $|H\rangle$. As discussed in Sec. 3.3.2, however, off-resonant excitation followed by spontaneous decay leads to the increased generation over time of $|V\rangle$. The

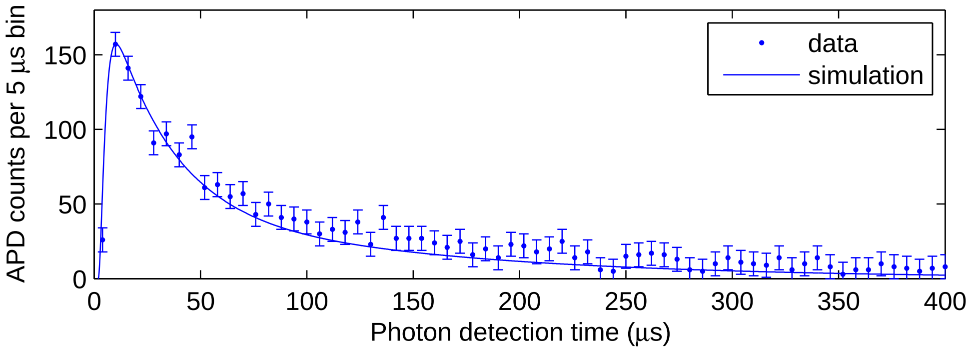

Figure 3.7: Photon counts as a function of time for a monochromatic Raman transition. The graph shows data and simulation, and the error bars represent one standard deviation. The parameters used in the simulations are $\Omega = 2\pi \times 16$ MHz and $g = 2\pi \times 0.9$ MHz.

map of $|S'\rangle$ to $|V\rangle$ (row four of Fig. 3.6) produces temporal photon shapes of inverted polarization due to the analogous effect. In the other two measurement bases, the shapes of the photons exiting the cavity for each polarization are the same.

Rows two and three of Fig. 3.6 show data and simulations of mapping $|S - S'\rangle$ to $|A\rangle$ and $|S + iS'\rangle$ to $|R\rangle$, respectively. Here, dephasing of the initial state leads to a slow rise of $|D\rangle$ and $|L\rangle$, as explained at the end of Sec. 3.3.2.

We find that the simulations reproduce the experimental data adequately. In row two, column three of Fig. 3.6, the simulation result for the R/L basis does not overlap exactly with the data. This effect is due to an accumulation of numerical errors for long integration times. The analogous effect is seen in the D/A basis of the map of $|S + iS'\rangle$ to $|R\rangle$ (row three, column two of Fig. 3.6).

Determining the experimental parameters

In the experiment, it is hard to perform an exact measurement of the Rabi frequency Ω_{tot} and the coherent coupling g. The Rabi frequencies are determined via a calibrated photodiode, a measurement which is accurate only within about 10%. The coherent coupling is inferred from measurements of the cavity length and its waist. Any motion of the ion decreases this coupling and an effective coupling can only be estimated. The results of the experiments, however, depend strongly on these two parameters. A larger coupling rate would speed up the Raman transfer process and would improve the fraction of coherent to incoherent evolution in the system. Similarly, a larger Rabi frequency accelerates the dynamics but also increases the probability of off-resonant excitation of the $4^2P_{3/2}$ states and the following spontaneous decay.

The Rabi frequency and the coherent coupling rate can be determined by fitting the simulations to the data. To that end, arrival time data of single photons from a monochromatic experiment are used. Monochromatic means that only one of the two Raman beams is switched on. In the data presented in Fig. 3.7, $|S'\rangle$ is transferred to $|V\rangle$. The data are taken for the full length of the photon until no population is left in $|S'\rangle$,

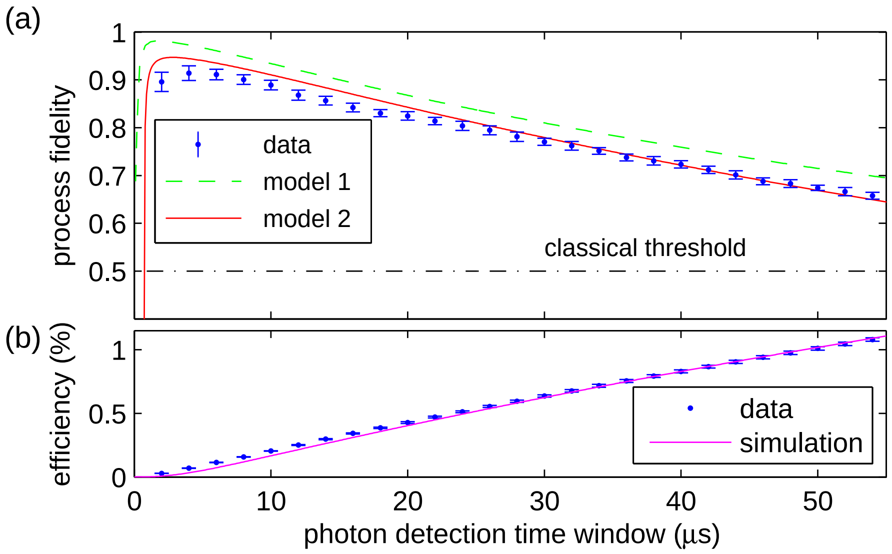

Figure 3.8: Process fidelity (a) and efficiency (b) of the state-mapping process. (a) The fidelity rises at the beginning and then decreases as a function of detection time. It takes its highest value, $(92 \pm 2)\%$, for a detection time window between 2 µs and 4 µs. For a 55 µs time window, it is still $(66 \pm 1)\%$. Model 1 (dashed line) shows the process fidelity of a simulation that does not include detector dark counts, imperfect state initialization, and magnetic field fluctuations. When these effects are taken into account (model 2), the simulation agrees well with the data. (b) The process efficiency increases as a function of detection time. After 55 µs, a photon is detected at the APDs in more than 1% of the mapping sequences. Image reproduced from (Stu13).

which for the parameter settings correspond to a detection time of 400 µs. A simulation with $\Omega_2 = 2\pi \times 16$ MHz ($\Omega_1 = 0$ MHz) and $g = 2\pi \times 0.9$ MHz fits well to the data set.

This monochromatic dataset is taken with the same Ω_2 as the bichromatic data shown in Fig. 3.6. For the bichromatic experiment, $\Omega_1 = \frac{1}{2}\Omega_2$ and $\Omega_{\text{tot}}^2 = \Omega_1^2 + \Omega_2^2$ are then calculated. Simulations with these values fit the bichromatic data well.

With this comparison of the simulations and data, we learn that the coherent ion-cavity coupling $g = 2\pi \times 0.9$ is considerably smaller than the expected maximum coupling rate $g_0 = 2\pi \times 1.43 \pm 0.01$ (Stu12b). This maximum value g_0 is calculated from knowledge of the cavity geometry ($L = (19.96 \pm 0.02)$ mm, $R = (10.02 \pm 0.01)$ mm, thus $w_0 = (13.2 \pm 0.8)$ µm). We attribute the smaller effective g to a displacement of the ion from the maximum of the cavity mode and to residual motion of the ion with respect to the cavity mode, which causes the ion to leave the place of maximum coupling (Eq. 3.6). This ion motion could be decreased by sideband cooling of the ion, which was not done in this experiment.

Process fidelity versus efficiency

Fig. 3.8(a) shows the process fidelity as a function of the time window in which the photon is detected. At first, the fidelity rises fast and then decreases as a function of the detection time window. Therefore, the maximum process fidelity is obtained by only taking into account photons which are produced in a narrow time bin shortly after the start of the experiment. However, using only a few photons leads to a very small number of photons detected in a single mapping sequence. This number of detected photons per sequence is described by the process efficiency. For the data in Fig. 3.6 in a time window of 2 µs to 4 µs, the process fidelity of the photon state is $(92 \pm 2)\%$, with a process efficiency of 4×10^{-4}. If all photons within the 55 µs of the experiment are considered, the process efficiency is 1.1% and the process fidelity decreases to $(66 \pm 1)\%$.

Model 1 in Fig. 3.8(a) shows the direct simulation result. Experimental imperfections were then added to the simulation results (model 2) to obtain quantitative agreement with the data. The relevant experimental imperfections that are taken into account are detector dark counts, imperfect state initialization, and magnetic field fluctuations. Detector dark counts of 5.6 Hz are included by calculating the probability of a dark count and adding these photons to the simulation result. Imperfect state initialization with a fidelity of 99% decreases the population in $|S\rangle$ and $|S'\rangle$ by this factor. Magnetic field fluctuations corresponding to an atomic decoherence time of $\tau = 110$ µs are included via an exponential decay $e^{-\frac{2t}{\tau}}$.

Fig. 3.8(b) shows the probability of detecting a photon on the APDs (process efficiency) as a function of the detection time window. After 55 µs, the measured process efficiency is 1.1%. The simulations show that this value corresponds to a photon being generated within the cavity in 16% of all attempts. In comparing the simulated and the experimental efficiency, the detection-path efficiency for this experiment is calculated to be 6.8%. This value agrees with previously measured values (Stu12b).

The rise of the process fidelity in the beginning was a surprising effect and was explained by the simulations. We found that the low fidelity is caused by off-resonant Raman processes that dominate the first half microsecond of the experiment and produce photons with the wrong polarization. Fig. 3.9 shows the simulation of the first microsecond of a map from $|S\rangle$ to $|H\rangle$ as an example to understand the underlying process. The Raman transition is set to drive population from $|S\rangle$ to $|D\rangle \equiv |3^2D_{5/2}, m_\mathrm{j} = -1/2\rangle$. Initially, however, the unwanted transitions $|S\rangle$ to $|D_{5/2}, m_\mathrm{j} = -\frac{3}{2}\rangle$ and $|S\rangle$ to $|D_{5/2}, m_\mathrm{j} = \frac{1}{2}\rangle$ are driven with almost equal strength, and we observe that the population in these two $D_{5/2}$ states rises along with the population in $|D\rangle$ (Fig. 3.9(a)). Both unwanted transitions produce vertically polarized photons in the cavity. Fig. 3.9(b) shows that at the beginning of the experiment $|H\rangle$ and $|V\rangle$ photons have almost the same probability to be produced in the cavity.

The slow decrease of the process fidelity over time was explained above by the off-resonant excitation followed by spontaneous decay of the ion to the $4^2S_{1/2}$ manifold, and the successive production of a photon with the unwanted polarization.

With a higher atom-photon coupling rate, process fidelity and efficiency of the presented state-mapping experiment could be increased. In Sec. 8.2.1, simulations of this experiment for a different set of CQED parameters are presented.

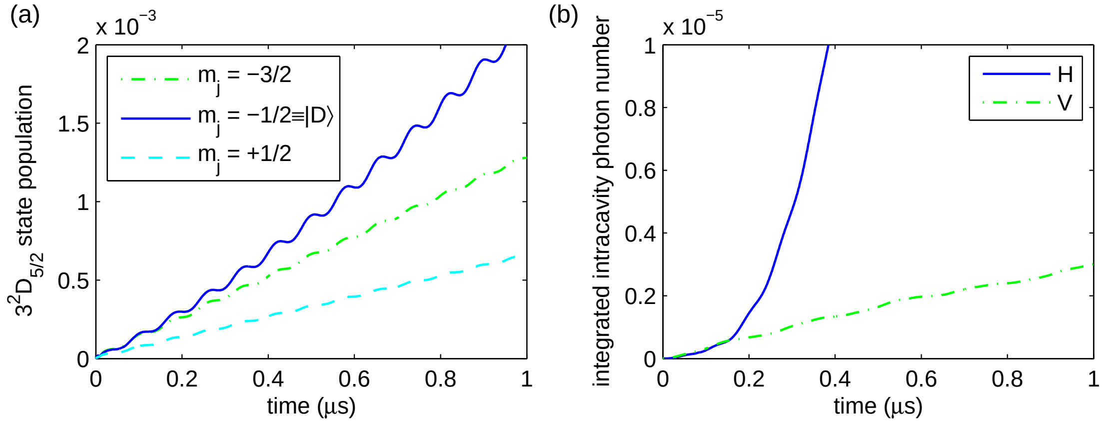

Figure 3.9: Simulation result of mapping $|S\rangle$ to $|H\rangle$ for the first microsecond of the experiment. (a) Atomic population of the $3^2D_{5/2}$ manifold as a function of time. At the beginning, the population of the target state $|D\rangle$ (solid line) increases only slightly faster than the non-target states $ketD_{5/2}, m_\mathrm{j} = -\frac{3}{2}$ (dash-dotted line) and $ketD_{5/2}, m_\mathrm{j} = \frac{1}{2}$ (dashed line). The oscillation at the difference of the laser frequencies is a result of the bichromatic driving scheme. (b) Integrated photon number of horizontally (solid line) and vertically (dashed line) polarized photons inside the cavity.

3.4 Ion-photon entanglement

A second experiment that realizes a quantum interface between atomic nodes and photonic channels in a quantum network is ion-photon entanglement. Recently, we have shown the successful implementation of tunable entanglement between an ion and a cavity photon (Stu12c).

In this experiment, an initial state of the ion is driven to two photon-ion states via a bichromatic cavity-mediated Raman transition. The bichromatic driving scheme in this experiment allows us to adjust phase and amplitude of the entangled state via relative phase and amplitude of the drive fields. The produced entangled state is independent of the time at which the photon is detected. This time independence is in contrast to previous experiments (Vol06, Bli04, Tog10), in which entanglement was generated via spontaneous emission along parallel channels. In these experiments, the relative phase of the state depended on the photon detection time, if nondegenerate Zeeman states were used. The coherent process in our bichromatic scheme, which generates time independence of the entangled state, is explained in detail in (Stu12a).

The experiment was carried out prior to the state mapping experiment of Sec. 3.3. For this ion-photon entanglement, however, simulations were not essential in helping to understand the physics of the underlying processes and were therefore not done until after the experimental results had been published. Simulations of the experiment became interesting once we started to analyze state-mapping data and found out that the coherent coupling rate in the state-mapping experiment was smaller than expected. Simulations of the ion-photon entanglement experiment were then used to confirm that the coupling rate of the state-mapping experiment had been determined correctly.

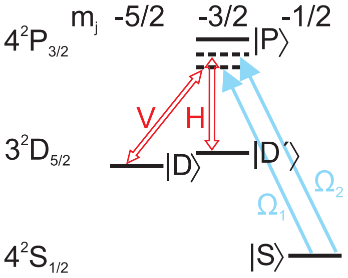

Figure 3.10: Relevant $^{40}\mathrm{Ca}^+$ levels for the ion-photon entanglement experiment (Stu12c). The ion is initialized in $|S\rangle$. A bichromatic field drives two simultaneous Raman transitions to $|D\rangle$ and $|D'\rangle$ via $|P\rangle$. While the transition to $|D\rangle$ produces a vertically polarized photon in the cavity, the transition to $|D'\rangle$ produces a photon with horizontal polarization. The Rabi frequencies of the bichromatic field are Ω_1 and Ω_2.

3.4.1 Ion-photon entanglement protocol

The experiment presented here produces entanglement between the electronic state of an ion and the polarization state of a single photon. In the experiment, the states $|D\rangle \equiv |3^2D_{5/2}, m_\mathrm{j} = -5/2\rangle$ and $|D'\rangle \equiv |3^2D_{5/2}, m_\mathrm{j} = -3/2\rangle$ of $^{40}\mathrm{Ca}^+$ are entangled with the photon polarization states $|V\rangle$ and $|H\rangle$.

As sketched in Fig. 3.10, the ion is initialized in $|S\rangle \equiv |4^2S_{1/2}, m_\mathrm{j} = -1/2\rangle$, and a bichromatic light field of Rabi frequencies Ω_1 and Ω_2 drives two Raman transitions to $|D\rangle$ and $|D'\rangle$ via the intermediate state $|P\rangle \equiv |4^2P_{3/2}, m_\mathrm{j} = -3/2\rangle$, producing a photon inside the cavity. The entangled state is

$$|\psi\rangle = \cos\alpha|DV\rangle + e^{\mathrm{i}\varphi}\sin\alpha|D'H\rangle. \tag{3.22}$$

The amplitudes $\cos\alpha$ and $\sin\alpha$ and the phase φ of $|\psi\rangle$ are set via the amplitudes and the relative phase of the two drive fields. The maximally entangled state

$$|\psi_\mathrm{m}\rangle = \frac{1}{\sqrt{2}}(|DV\rangle + |D'H\rangle) \tag{3.23}$$

is generated by setting the Rabi frequencies such that horizontally and vertically polarized photons are produced with the same probability inside the cavity.

3.4.2 Simulation and interpretation

Here, a simulation of the process that produces the entangled state of Eq. 3.23 is shown. Initially, the ion is in $|S\rangle$. As the bichromatic field drives the Raman transition to $|D\rangle$ and $|D'\rangle$ the population in these states rises and a single photon is generated. The populations of these states and the probability to detect a photon is shown in Fig. 3.11.

To produce the maximally entangled state, both photon polarizations have to be produced with equal probability. As a consequence, we expect that the populations of the target states $|D\rangle$ and $|D'\rangle$ should also be equal. However, we see that the population in $|D\rangle$ is higher than in $|D'\rangle$ (Fig. 3.11 (b)). This imbalance is a consequence of off-

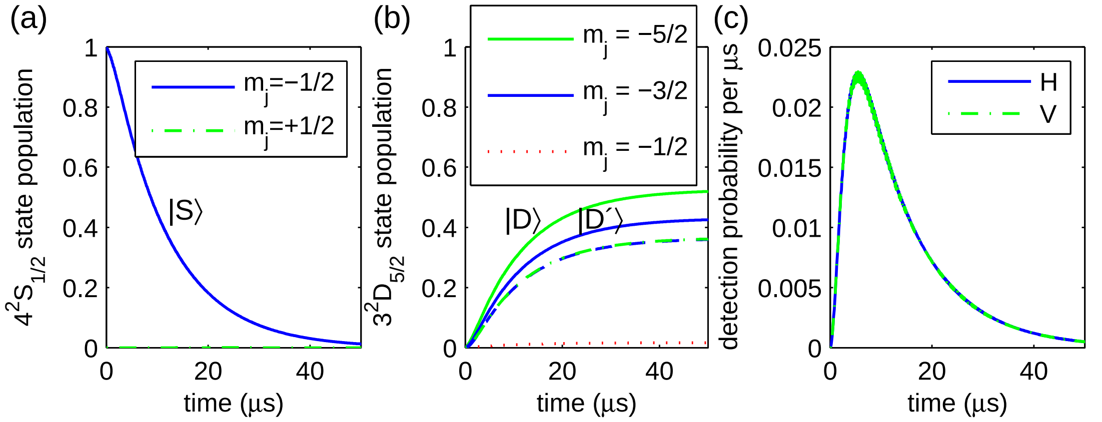

Figure 3.11: Entanglement of the electronic states $|D\rangle$ and $|D'\rangle$ of the ion with the polarization states $|H\rangle$ and $|V\rangle$ of a cavity photon. (a) Population of the $4^2S_{1/2}$ manifold. (b) Population of the $3^2D_{5/2}$ manifold. Over time, the Raman transition drives population from $|S\rangle$ to $|D\rangle$ and $|D'\rangle$. The dashed lines show the populations of $|D\rangle$ and $|D'\rangle$ without spontaneous decay. (c) Temporal shape of the cavity photon.

resonant excitation to the $P_{3/2}$ manifold followed by spontaneous decay to the $D_{5/2}$ manifold. The Clebsch-Gordan coefficient for the transition from $|P\rangle$ to $|D\rangle$ is $\sqrt{2/3}$, while the coefficient for the $|P\rangle \leftrightarrow |D'\rangle$ transition is $-\sqrt{4/15}$. Thus, the probability of the ion to decay to $|D\rangle$ is higher. A spontaneous decay to the $D_{5/2}$ state manifold does not produce a photon inside the cavity. Therefore, these scattering events do not decrease the fidelity of the entangled state but only lower the efficiency of the experimental process. To confirm that the imbalance of population in $|D\rangle$ and $|D'\rangle$ is only due to these scattering events, the population of $|D\rangle$ and $|D'\rangle$ generated only from the Raman process is calculated. In the simulations, these populations are obtained by changing the spontaneous decay to populate an auxiliary level, additionally included into the simulations. The dashed lines in Fig. 3.11(b) show that the populations without spontaneous decay are indeed equal.

Theoretically, spontaneous decay to the $D_{5/2}$ manifold limits the efficiency of the entanglement experiment; for the presented simulation, around 25% of the time, the atom decays into the $D_{5/2}$ manifold and does not produce a cavity photon. These decay events become less likely by choosing lower Rabi frequencies.

To create the maximally entangled state, the temporal shapes of the horizontally and the vertically polarized photons have to overlap precisely. A mismatch in the temporal shape of $|H\rangle$ and $|V\rangle$ would provide knowledge of which state $|D\rangle$ or $|D'\rangle$ has been produced with higher probability for a specific arrival time of the photon. The photon shapes are matched by setting the ratio of the Rabi frequencies of the two drive fields correctly ($\Omega_2/\Omega_1 = 0.75$).

The Raman fields are σ^--polarized and therefore only interact with $|P\rangle$. Any off-resonant excitation followed by decay to the $4^2S_{1/2}$ manifold is back into $|S\rangle$, which is the initial state of the experiment. Therefore, such a scattering event does not compromise the fidelity of the final state. Using this σ^--driving scheme, the fidelity of the final state can be close to 100% even for a system in which the atomic decay γ dominates over the coherent coupling g, and increasing the coupling parameter g would not improve the fidelity significantly. This fact is a clear advantage of this protocol over the state-mapping protocol, in which γ and g play an important role for the fidelity of the mapping process. However, a higher value of g makes the process faster, decreasing effects from experimental imperfections such as laser noise, magnetic field noise or detector dark counts.

The simulation neglects APD dark counts and imperfect state initialization and calculates 99.9% fidelity with respect to the maximally entangled state. The 0.1% infidelity is due to the Raman transition to the $|3^2D_{5/2}, m_{\mathrm{j}} = -1/2\rangle$ state. This Raman transition is driven off-resonantly and generates a vertically polarized photon.

3.4.3 Agreement with the experiment

The experiments were performed with the same apparatus as the state-mapping experiment. To be able to drive σ^- transitions, the beam geometry and the direction of the magnetic field were changed (Stu12a). The magnetic field was set to 2.96 G and the cavity detuning from the $|P\rangle \leftrightarrow |D\rangle$ transition was about −400 MHz.

To initialize the experiment, the ion is optically pumped to $|S\rangle$. Then, the bichromatic Raman field is switched on for 37 µs, generating a single photon that is entangled with the ion. The full ion-photon quantum state is analyzed via state tomography (Stu12a). Ion and photon are measured in all combinations of the three Pauli spin bases $\sigma_{\mathrm{x}}, \sigma_{\mathrm{y}}, \sigma_{\mathrm{z}}$ for the ion and the three polarization bases $H/V, D/A, R/L$ for the photon. In total, this corresponds to 9 measurement settings.

The entangled state is analyzed as a function of relative phase and amplitudes of the drive fields, proving that the produced state is fully tuneable. The details are given in the paper (Stu12c) and in Andreas Stute's thesis (Stu12a). The fidelity of the reconstructed density matrix with respect to the maximally entangled state (Eq. 3.23) is found to be $(97.4 \pm 0.2)\%$. The main effects that reduce the fidelity are APD dark counts, imperfect overlap of the photon pulse shapes, and imperfect state initialization.

The probability to generate a photon inside the cavity is 75% (see previous Sec. 3.4.2). In the setup, however, the combined mirror losses are (68 ± 2) ppm (Rus08), leading to an output coupling efficiency of only 16% of these photons (Stu12a). The remaining 84% of the produced photons are absorbed by the mirror coating and are not coupled out of the cavity. As a result of the imperfect detection path, a photon is detected in 5.7% of the experiments. A higher transmission of the outcoupling mirror as well as smaller mirror losses would increase the efficiency of the experiment considerably.

Fig. 3.12 shows the photon data of an experiment that produces the maximally entangled state of Eq. 3.23. Adjusting parameters in the simulations, we find that the temporal shape of the photons of the simulation agree well with the data for values of $g = 0.9$ MHz and $\Omega_{\mathrm{tot}} = 2\pi \times 39$ MHz. This result confirms that the value of $g = 0.9$ MHz for the state-mapping experiment was indeed correct. The Rabi frequency found in the simulation is smaller than an experimentally measured value of around $\Omega_{\mathrm{tot}} = 2\pi \times 60$ MHz. However, we believe that the experimental calibration is not very accurate and trust the simulated value. In the course of the simulations, we learned that the Rabi frequencies of the drive beams should be measured more precisely in the future. As g and Ω_{tot} both

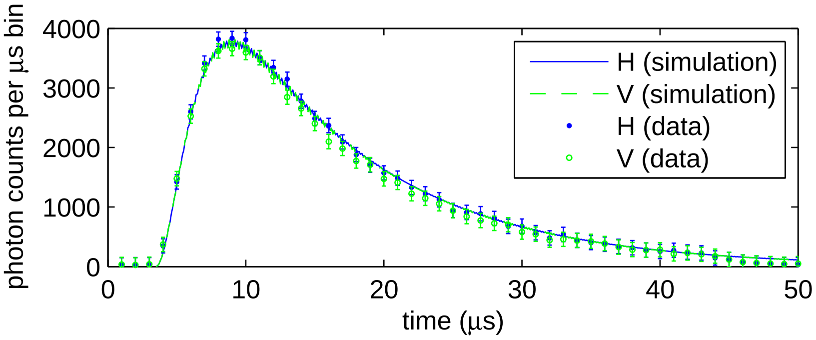

Figure 3.12: Temporal shape of H and V polarized photons. The plot shows data and simulation for the case of balanced Rabi frequencies of the Raman field. The process produces the maximally entangled state (Eq. 3.23).

change the temporal shape of the photons significantly, an accurate measurement of the Rabi frequency would allow us to narrow down the possible range of g.

Simulations in agreement with these data are the first step towards simulating the two-ion entanglement experiment, which is presented below. A two-ion experiment is considerably more complex and understanding the underlying processes is gained via simulations.

3.5 Cavity-induced heralded two-ion entanglement

While ions are routinely entangled with one another via shared motional degrees of freedom, a cavity-based entanglement scheme is useful to entangle remote ions or to generate entanglement in other local quantum registers such as neutral atoms. The probabilistic entanglement is generated via simultaneous detection of photons from both qubits. This process allows for transport of quantum information in a network via entanglement swapping. A cavity-based scheme may speed up the rate at which remote entanglement can be generated with respect to entanglement generated in free space, as was shown with Yb^{+} (Mau09, Moe07).

Furthermore, deterministic coupling of multiple ions to a cavity promises great advantages for quantum information science. Proposals show that multiple ions in a cavity can provide quantum error correction in networks (Enk97), improve quantum memories (Lam11), and help to achieve high-fidelity gates between registers for distributed quantum computing (Jia07).

Our scheme entangles two ions via a cavity and is similar to the scheme proposed in (Dua03). The ion-photon entanglement protocol described above (Sec. 3.4.1) is the basis for this experiment. Two ions are placed in the waist of the cavity such that they both interact with the cavity field and are driven by the same bichromatic Raman field. The detection of one horizontally polarized photon and one vertically polarized photon exiting the cavity heralds ion-ion entanglement. The results of this experiment are published in (Cas13). Here, the protocol and the experimental results are described briefly, and the focus lies on the interpretation of the results provided by the simulations.

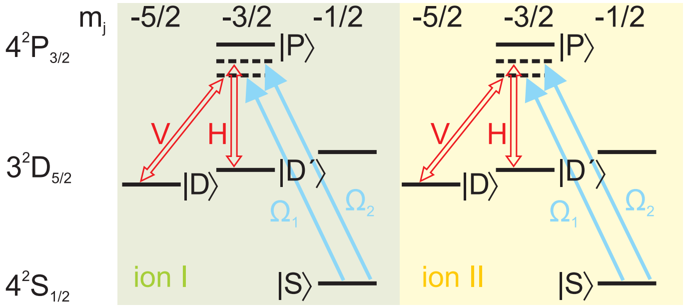

Figure 3.13: A bichromatic field of Rabi frequencies Ω_1 and Ω_2 drives two Raman transitions to the $|D\rangle$ and the $|D'\rangle$ states of ion I and ion II, generating two single photons in the cavity. The detection of a vertically and a horizontally polarized photon entangles ion I with ion II.

3.5.1 Ion-ion entanglement protocol

The electronic states used in this experiment are the same as in the atom-photon entangling experiment (Sec. 3.4.1): the initial state $|S\rangle \equiv |4^2S_{1/2}, m_\mathrm{j} = -1/2\rangle$, the intermediate state $|P\rangle \equiv |4^2P_{3/2}, m_\mathrm{j} = -3/2\rangle$, and the two target states $|D\rangle \equiv |3^2D_{5/2}, m_\mathrm{j} = -5/2\rangle$ and $|D'\rangle \equiv |3^2D_{5/2}, m_\mathrm{j} = -3/2\rangle$. As shown in Fig. 3.13, the ions are coupled with equal strength to the mode of the cavity, and a bichromatic Raman field drives both ions. The transition from $|S\rangle$ to $|D\rangle$ and $|D'\rangle$ produces a single photon of horizontal and vertical polarization from each ion. Thus, the ions are entangled with the photons produced inside the cavity. In the case of balanced Rabi frequencies Ω_1 and Ω_2, in which $|H\rangle$ and $|V\rangle$ are produced with equal probability, the final state is the following:

$$|\psi\rangle = \sqrt{\frac{1}{4}}(|DDVV\rangle + |D'DHV\rangle + |DD'VH\rangle + |D'D'HH\rangle). \tag{3.24}$$

Here, the four particle state $|\mathrm{ion_I}\ \mathrm{ion_{II}}\ \mathrm{photon}\ \mathrm{photon}\rangle$ describes the non-separable electronic states of ions I and II and the two cavity photons.

The detection of two photons, one with vertical polarization and one with horizontal polarization, heralds entanglement of the two ions' electronic states.

$$|\psi_\mathrm{heralded}\rangle = \sqrt{\frac{1}{2}}(|DD'\rangle + |D'D\rangle) \tag{3.25}$$

The entangled state is the two-qubit Bell state $|\Psi^+\rangle$. The entanglement is a consequence of the indistinguishability of the photons which are generated in the cavity. The ions are coupled to the same cavity mode with equal strength, and therefore both ions emit photons in the same spatial mode. A photon in the cavity has equal probability of being generated from either ion.

In contrast to the entanglement protocol (Sec. 3.4.1), in this heralded scheme, imbalanced Rabi frequencies do not decrease the fidelity of the produced state. If we consider a case in which one photon polarization is produced more often, the amplitudes of the two middle terms of Eq. 3.24 are nevertheless equal. These two amplitudes are the only relevant amplitudes of the state after the projection onto electronic states by detection of $|H\rangle$ and $|V\rangle$.

3.5.2 Simulation and Interpretation

Simulations of the ion-ion entanglement are implemented using the Monte Carlo method. One Monte Carlo trajectory of the simulation is equivalent to running the experiment once (one experimental cycle). Each cycle has a different outcome due to the stochastic nature of the decay mechanisms. Thereby, the simulation mimics different possible evolutions of the system.

The simulations consider two ions coupled to the cavity mode, and the level schemes of both ions are reduced to only five levels of ^{40}Ca$^+$. These levels are indicated in Fig. 3.13. Neglecting all other electronic levels is possible because their populations are not relevant in this experiment. This assumption was confirmed by comparison with simulations using the full level scheme.

In the simulation, the fidelity of the generated state with respect to $|\Psi^+\rangle$ is calculated via the the density matrix ρ.

$$\mathrm{F}_{\Psi^+} = \langle\Psi^+|\rho|\Psi^+\rangle = \frac{1}{2}(\rho_{\mathrm{DD',DD'}} + \rho_{\mathrm{D'D,D'D}}) + \rho_{\mathrm{D'D,DD'}} \tag{3.26}$$

The term $\frac{1}{2}(\rho_{\mathrm{DD',DD'}} + \rho_{\mathrm{D'D,D'D}})$ represents the population of the ions in states $|DD'\rangle$ and $|D'D\rangle$, while the term $\rho_{\mathrm{D'D,DD'}}$ represents the coherence between $|DD'\rangle$ and $|D'D\rangle$.

The electronic states of the ions are evaluated as a function of the arrival time differences of $|H\rangle$ and $|V\rangle$ which are obtained in the Monte Carlo simulation.

The effect of spontaneous decay

Triggering on detection of one horizontally and one vertically polarized photon guarantees that one ion is in $|D\rangle$ and the other ion is in $|D'\rangle$. This result is not influenced by spontaneous decay of the atom; due to the σ^--drive, the decay to the $4^2S_{1/2}$ manifold leads always back to the initial state, and the decay to the 3^2D states prevents the generation of a cavity photon and therefore only decreases the efficiency of the process. As a consequence, the population contrast $\frac{1}{2}(\rho_{\mathrm{DD',DD'}} + \rho_{\mathrm{D'D,D'D}})$ remains at the target value of 0.5 throughout the experiment. The coherences of the target state, however, are destroyed by spontaneous decay of the atoms. The result of the experiment is determined by the times at which decays happen and by the number of decays.

In the following, the outcome of the experiment for different numbers of decay and different decay times is presented.

No spontaneous decay: In an ideal case, there would be no spontaneous decay of the ion. The produced state then has a fidelity of close to 100 % with respect to the target Bell state. The process that limits the fidelity is the off-resonant Raman transition to $|3^2D_{5/2}, m_{\mathrm{j}} = -1/2\rangle$ (Sec. 3.4.2).

Fig. 3.14 shows a Monte Carlo trajectory of an experiment without spontaneous decay. Over time, the Raman lasers drive both ions from $|S\rangle$ to $|D\rangle$ and $|D'\rangle$, increasing the probability to detect a $|V\rangle$ and an $|H\rangle$ photon, respectively. For this trajectory, after 2.3 µs, a quantum jump occurs and a $|V\rangle$ photon is detected. The probability to detect

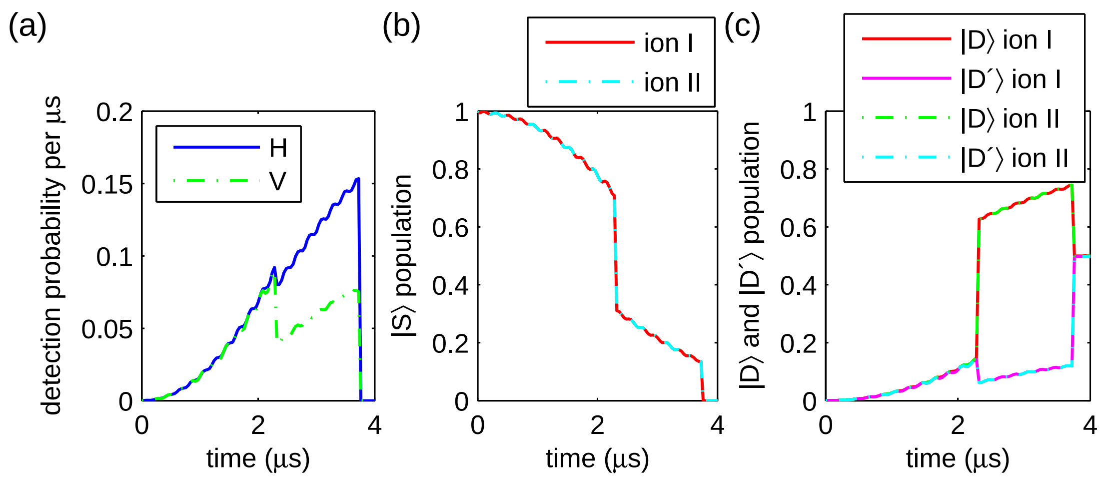

Figure 3.14: Monte Carlo trajectory of an ion-ion entangling experiment without spontaneous decay of the ions. (a) Probability to detect $|H\rangle$ and $|V\rangle$ as a function of time. (b) Population of $|S\rangle \equiv |4^2S_{1/2}, m_\mathrm{j} = -1/2\rangle$ of ion I and ion II. (c) Populations of $|D\rangle \equiv |3^2S_{5/2}, m_\mathrm{j} = -5/2\rangle$ and $|D'\rangle \equiv |3^2S_{5/2}, m_\mathrm{j} = -3/2\rangle$ of ion I and ion II.

another $|V\rangle$ photon decreases by half as only one ion that can emit a photon is left in the cavity. Both ions' electronic states are affected equally; the population of $|D'\rangle$ of each ion decreases by half its amount (less than 0.1). The same is true for the population of $|S\rangle$ of each ion, which decreases by more than 0.4, while the population of $|D\rangle$ of each ion increases by 0.5. Both ions have emitted the photon with equal probability and could now be in $|D\rangle$.

The evolution continues and the probabilities to detect $|H\rangle$ and $|V\rangle$ rise again. The second quantum jump after 3.7 µs is due to the detection of the $|H\rangle$ photon. As a consequence, the population of $|S\rangle$ decreases to 0 (and with this the probability to detect another photon), and $|D\rangle$ and $|D'\rangle$ both jump to 0.5. The final state is the Bell state $1/\sqrt{2}(|DD'\rangle + |D'D\rangle)$.

Spontaneous decay before $|H\rangle$ and $|V\rangle$: Fig. 3.15 shows a Monte Carlo trajectory of an experiment in which one ion spontaneously decays to $|S\rangle$ shortly before a photon is detected. As it is possible in principle to detect the scattered photon, it is known which of the two ions is in $|S\rangle$. Therefore, this ions' state is projected to $|S\rangle$. The trajectory shows that, while ion I evolves coherently, ion II decays several times to $|S\rangle$. The last projection of ion II is after 5 µs. A cavity photon $|H\rangle$ is detected 0.5 µs after this spontaneous decay event. This photon is most likely to come from the ion which has not previously decayed, ion I in this example. As a consequence, the population of $|D'\rangle$ of ion I increases to almost 1. It would increase to exactly 1 if the spontaneous decay occurred at the same time as the detection.

In the following 3 µs, ion II is driven via the Raman lasers. Predicated on our future detection of two orthogonally polarized photons, the second cavity photon is a $|V\rangle$ photon. It is now most likely produced by ion II, which is projected into $|D\rangle$. The two ion state is then $|\psi\rangle = \sqrt{1-\epsilon}\ |D'D\rangle + \sqrt{\epsilon}\ |DD'\rangle$, with $\epsilon \ll 1$. Again, the state would be

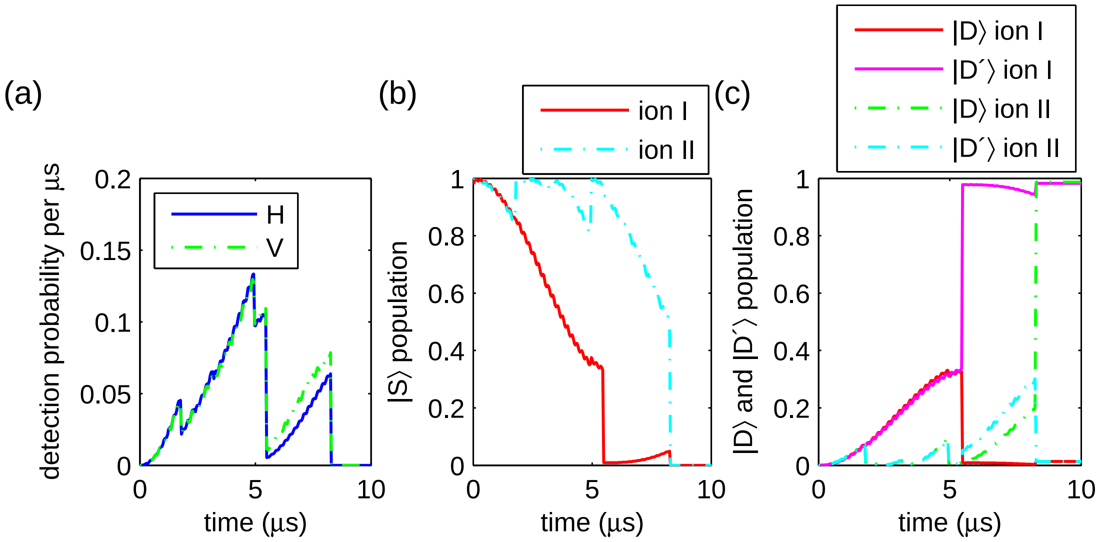

Figure 3.15: Monte Carlo trajectory of an ion-ion entangling experiment with spontaneous decays of the ions before $|H\rangle$ and $|V\rangle$. (a) Probability to detect $|H\rangle$ and $|V\rangle$ as a function of time. (b) Population of $|S\rangle$ of ion I and ion II. (c) Populations of $|D\rangle$ and $|D'\rangle$ of ion I and ion II.

exactly $|\psi\rangle = |D'D\rangle$ ($\epsilon = 0$) if spontaneous decay and photon detection had occurred at the same time. The spontaneous decay has destroyed the coherence of the entangled state from Eq. 3.25.

Generally, this example shows that the coherence terms decay as a function of the arrival time of the photons. The later the photons arrive, the more likely it is that a spontaneous decay has occurred before.

Spontaneous decay between $|H\rangle$ and $|V\rangle$: A decay of an ion after the detection of a first cavity photon also destroys the coherence between the two ions: after the decay it is known which ion produced this first cavity photon. After the second photon is produced, again, the system is in one of the two states, either $|\psi\rangle = |DD'\rangle$ or $|\psi\rangle = |D'D\rangle$, but not in a superposition of the two.

An example of a trajectory in which the coherence term $\rho_{\mathrm{D'D,DD'}}$ becomes negative is shown in Fig. 3.16. After 1.6 µs, a $|V\rangle$ photon is detected. Only 0.2 µs later, this detection is followed by a spontaneous decay of ion I. Now the system is in the state $|\psi\rangle = |SD\rangle$. We know ion I has decayed and is in $|S\rangle$, and therefore, the vertically polarized photon was produced by ion II, which now has to be in $|D\rangle$. In the following, while the system evolves ion I decays twice (at 5.7 µs and at 10.6 µs) projecting the system back to the state $|\psi\rangle = |SD\rangle$.

Following the last decay, the system coherently evolves without decay. We observe that the vertically polarized photon (produced inside the cavity by ion I) is reabsorbed by ion II in an inverse Raman process. The population of $|S\rangle$ of ion II increases with time. As an effect, the probability of detecting a horizontally polarized photon increases faster with time than the probability of detecting a vertically polarized photon. Thus, when after 18.3 µs, the second photon $|H\rangle$ is detected, it could have been produced by

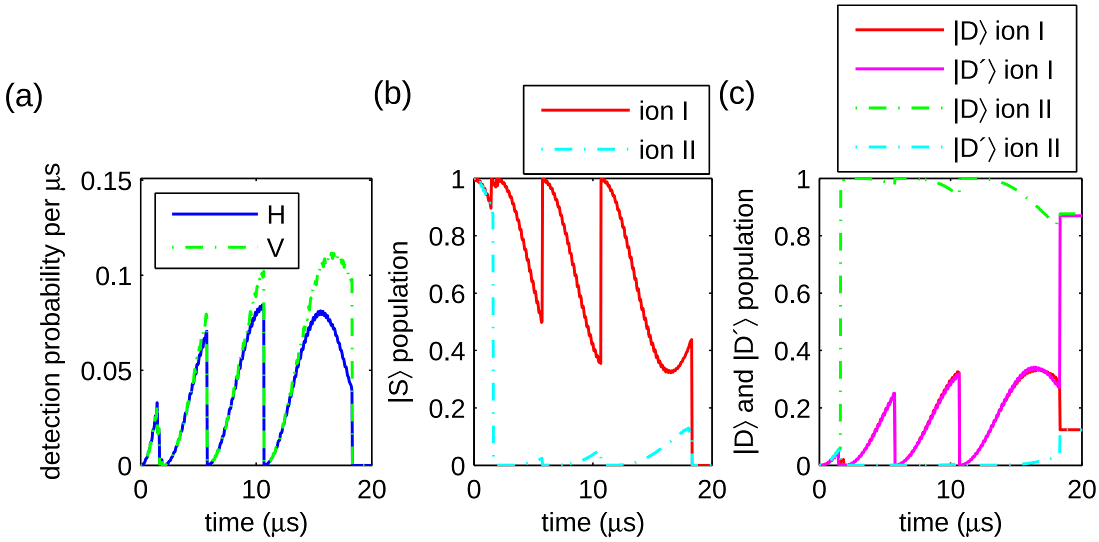

Figure 3.16: Heralded two-ion entanglement simulation. The trajectory shows several spontaneous decays of the ion between the detection of the two photons. (a) $|H\rangle$ and $|V\rangle$ photon detection probability as a function of time. (b) Populations of ion I and ion II in the initial state $|S\rangle$. (c) Populations of ion I and ion II in the target states $|D\rangle$ and $|D'\rangle$

either ion, ion I or ion II. The process of ion II reabsorbing a photon and emitting a second one adds a geometric phase of π. The interference of the two possible photon production processes results in a negative coherence between the two ions. In this example, $\rho_{\mathrm{D'D,DD'}} = -0.33$. However, if the evolution without decay was long enough, the system would be in the state $|\Psi^-\rangle = \sqrt{\frac{1}{2}}(|DD'\rangle - |D'D\rangle)$. In this case the fidelity with respect to the target state (Eq. 3.25) would be 0 %. If such events with spontaneous decays between the two photon detections are present, it follows that the state fidelity can drop below the classical threshold of 50%.

From these trajectories we learned about the effect of spontaneous decay events on the fidelity of the final state with respect to the target state. Due to spontaneous decay before either photon is detected, we expect the fidelity to decrease as a function of absolute photon detection time. If the photons are detected shortly after the beginning of the experiment, it is less likely that there has been a decay event prior to the detection. Due to spontaneous decay between detection of $|H\rangle$ and $|V\rangle$ photons, we expect the fidelity to decrease as the detection time difference of the photons increases. As this detection time difference increases, the probability of a scattering event occurring within this time window increases.

Knowledge about the effects described here, will help in the understanding of the experimental results presented in the following.

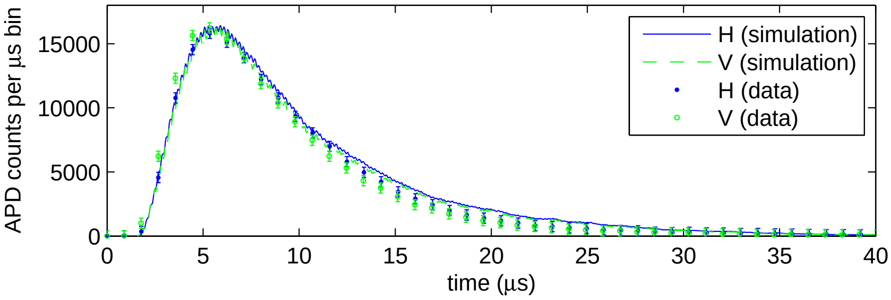

Figure 3.17: Data and simulation of the temporal shape of the photons exiting the cavity for the ion-ion entanglement experiment. The APD counts of horizontally and vertically polarized photons are plotted versus photon arrival time.

3.5.3 Experimental results

Determining the experimental parameters

In the experiment, the magnetic field is set to be $B = 2.96$ G, and the cavity detuning from the $|S\rangle \leftrightarrow |P\rangle$ transition is -400 MHz. The Rabi frequency and the coherent coupling rate are determined by matching the temporal shapes of the photons of the simulation to the experimental data. This shapes are displayed in Fig. 3.17. The total Rabi frequency Ω_{tot} is found to be $2\pi \times 55$ MHz ($\Omega_2/\Omega_1 = 1.6$), and $g = 2\pi \times 1.0$ MHz. In the experiments described before (Sec. 3.3 and Sec. 3.5), the coherent coupling rate was slightly smaller $g = 2\pi \times 0.9$ MHz. We attribute this effect to a slightly better alignment of the ions with respect to the cavity mode in the experiment described here compared to the other two experiments.

In comparing data and simulation, we find a detection-path efficiency of 3.5% for the ion-ion entanglement experiment. This value is smaller as in previous experiments (Sec. 3.3.3), an effect that is attributed to bad alignment of the output path.

Fidelity measurement

To evaluate the quality of the ion-ion entanglement experiment, the fidelity of the final state with respect to the Bell state (Eq. 3.25) is measured as a function of arrival time difference T of the two photons. In the simulation, the fidelity with respect to $|\Psi^{+}\rangle$ is extracted from the density matrix (Eq. 3.26). Experimentally, the full density matrix can be determined via state tomography as done for the ion-photon entangled state (Sec. 3.4.3). For the two-ion experiment presented here, however, state tomography would require single-ion addressing, which was not implemented at the time when the experiment was performed and was therefore not realized.

Parity measurements provide a possibility to estimate the fidelity of the two-ion state without reconstructing the full density matrix. This estimate is implemented in the experiment via a measurement of the population in the states $|DD'\rangle$ and $|D'D\rangle$ and a bound for the coherences between these two states. After mapping the ion population in $|D'\rangle$ to $|S\rangle$, the population is measured via fluorescence detection on the $S_{1/2} \leftrightarrow P_{1/2}$ transition. The coherence is estimated via the contrast of parity oscillations (Sac00,

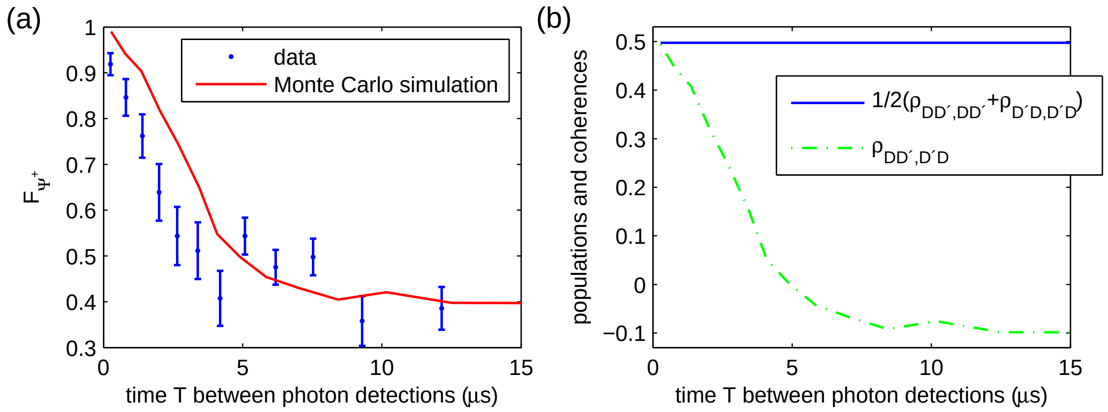

Figure 3.18: (a) Fidelity measurement with respect to the Bell state $|\Psi^+\rangle$ as a function of the arrival time difference T of $|H\rangle$ and $|V\rangle$ photons. The measured data give a lower bound on the fidelity. (b) Populations and coherences of the simulated entangled state as a function of photon arrival time difference. While the population term remains constant, the coherence term decreases as a function of T.

Lei03b, Slo13). Details about this technique will be presented in Bernardo Casabone's thesis and are found in (Cas13).

Fig. 3.18(a) shows the fidelity data and simulation with respect to $|\Psi^+\rangle$ as a function of photon arrival time difference T. Each time bin contains about 1750 entanglement events. The bin spacing increases with T as photon coincidence becomes less likely. The fidelity decreases as the photon arrival time difference increases. For photons with a detection time difference less than or equal to 0.5 µs, the measured lower bound for the fidelity is $(92 \pm 3)\%$. For a detection time difference of more than 5 µs, the fidelity decreases below the classical threshold of 50 %. This surprising effect is due to the reabsorption of a cavity photon and is explained above in the interpretation (Sec. 3.5.2). Fig. 3.18(b) shows simulated populations $1/2(\rho_{\mathrm{DD',DD'}} + \rho_{\mathrm{D'D,D'D}})$ and coherences $\rho_{\mathrm{D'D,DD'}}$ as a function of T. While the populations remain constant as T increases, the coherences decrease rapidly with increasing T.

In the experiment presented here, a non-classical state of $(55\pm2)\%$ fidelity with respect to the Bell state $|\Psi^+\rangle$ is produced at a rate of 4.3 events per second. The high-fidelity entangled state of $F_{\Psi^+} \leq (92 \pm 3)\%$ is produced at a rate of 0.2 events per second.

In the simulations, the fidelity of the entangled state from photons with $T \leq 0.5$ µs is 99%. We do not know exactly what produces the 7% lower fidelity in the experiment. Tentatively, we attribute this difference to faster decoherence rates in the experiment, which could stem from higher laser noise than assumed in the simulations. Other sources of experimental imperfections which may decrease the fidelity in the percent regime include imperfect state readout and state preparation, detector dark counts or atomic decoherence from magnetic field fluctuations.

3.6 Conclusion

This Chapter presented three experiments that realize quantum network protocols and shown that our simulations reproduce the data proving that we understand our CQED system. We learned that fidelities and efficiencies of the experiments are limited by the rate of spontaneous decay of the ion, which is considerably larger than the coherent coupling rate. This coupling rate could be increased substantially by implementing a cavity with a smaller mode volume. In the next chapters, the route towards this implementation of an ion-cavity system with small cavity-mode volume and high coupling rate is presented.

Chapter 8 then comes back to the experiments and simulations presented here to show simulations for CQED parameters of such a new ion-cavity system regime. I will show how efficiencies and fidelities can be improved with a coupling rate in reach with the apparatus presented in the following.

4 Simulations of ion-trap designs

Ions are trapped quasi-permanently and well isolated from environmental perturbations in RF Paul traps (Pau90) under ultra-high–vacuum conditions. For the purpose of implementing an FFPC with an ion trap, one can choose from a range of ion-trap designs. Possible designs include surface-electrode traps (Chi05), segmented linear traps based on microchip technology (Sch08b), 'endcap' (Sch93, Wil11) or stylus ion traps (Mai09), and linear blade traps (Gul03, Rie05).

For CQED experiments to enter the strong coupling regime for optical wavelength, dielectric mirrors are required. When considering the integration of dielectric mirrors into an ion trap, one should keep in mind the effects of dielectrics on the ion. Charges on dielectrics in vacuum are quasi-permanent and distort the ion-trap potential. They can be produced by UV light via photo-electron ionization (Har10) in a way that is not well understood and difficult to model. The best strategy is to avoid any charging of dielectrics and to minimize the influence of possible charges on the ion. As a solution, dielectric mirrors are either placed far away from the trap (Her08, Rus09, Gut01) or the dielectric components are well shielded (Bra11, Wil11, Van10, Kim11).

This chapter describes possible ion-trap designs for implementing an FFPC and elaborates on each design's advantages and disadvantages. Simulations of the trap potentials with and without fibers are shown, and I focus on the linear blade trap which we choose to implement in the experimental setup of this thesis work.

Parts of the Matlab code used for these simulations were written by Nikos Daniilidis, when he was a postdoc in our group.

4.1 Theoretical principles of Paul traps

Using a time-dependent electromagnetic field together with a static field, it is possible to generate a restoring force in three dimensions for a charged particle. In the case of rotational symmetry along the z-axis, the potential has the form of a quadrupole,

$$\Phi(t) = \frac{U_0 + V_0 \cos \Omega t}{2d^2}(x^2 + y^2 - 2z^2), \tag{4.1}$$

where U_0 is the static field, $V_0 \cos \Omega t$ the field oscillating with frequency Ω, and d a normalization parameter. This is the trapping potential of a Paul trap. Details about ion traps and specifically Paul traps are found in textbooks such as (Wer09, Gho95). The theory presented here follows (Wer09).

The equations of motion for all three dimensions $u = x, y, z$ are given by

$$\frac{d^2u}{dt^2} = \frac{Q}{Md^2}(U_0 + V_0 \cos \Omega t)u. \tag{4.2}$$

Depending on the mass M and the charge Q of the particle, these equations determine if the particle is trapped stably in the potential. Using the abbreviations

$$\tau = \frac{\Omega t}{2}; \; a_{\mathrm{x}} = a_{\mathrm{y}} = -2a_{\mathrm{z}} = -\frac{4QU_0}{Md^2\Omega^2}; \text{ and } q_{\mathrm{x}} = q_{\mathrm{y}} = 2q_{\mathrm{z}} = \frac{2QV_0}{Md^2\Omega^2}, \tag{4.3}$$

the equations of motion are written as

$$\frac{d^2u}{d\tau^2} + (a_u - 2q_u \cos 2\tau)u = 0. \tag{4.4}$$

These differential equations are of the homogeneous Mathieu type. Stable solutions of the Mathieu equation and thus stable trapping conditions of charged particles occur only for certain values of a and q; see, e.g., Fig. 2.6 of (Gho95) for a graphical representation. Unless the trap is operated at a point of common stability of the parameters a_u and q_u in all tree dimensions, stable trapping is not possible.

Trap depth and frequencies

The stability region used for ion trapping experiments is the region of $|a_{\mathrm{i}}| < 1$ and $q_{\mathrm{i}} < 1$ for $i = x, y, z$. In this region, the motion of the ion is approximated by two frequencies; a particle trajectory of slow motion with frequency ω and a fast motion with the trap frequency Ω with $\omega = \beta\Omega/2$. This adiabatic approximation is valid for a stability parameter $\beta_{\mathrm{i}}^2 \approx a_{\mathrm{i}} + q_{\mathrm{i}}^2/2 \ll 1$. The equations of motion are then simplified to

$$u_{\mathrm{i}}(t) = A\left(1 - \frac{q_{\mathrm{i}}}{2}\cos \Omega t\right)\cos \omega_{\mathrm{i}} t \tag{4.5}$$

The frequency ω is small since β is small, and the motion is called secular motion of the ion. Superimposed on this secular motion is a fast motion of the particle with frequency Ω, known as micromotion. For a case in which the DC potential and the RF potential are offset, the micromotion is responsible for ion heating by the trap drive. To avoid this heating, the minimum of the DC potential is adjusted via compensation electrodes to overlap its position with the minimum of the RF potential.

Neglecting micromotion, the particle is described as an harmonic oscillator of frequency ω_{i}. In the case $U_0 = 0$, that is, with the DC electrodes on ground, the trap frequency along the z axis is calculated as

$$\omega_{\mathrm{z}} = \frac{QV_0}{\sqrt{2}Mz_0^2\Omega} \tag{4.6}$$

inside the time-averaged pseudopotential with depth

$$\bar{D}_{\mathrm{z}} = \frac{QV_0^2}{4Mz_0^2\Omega^2}, \tag{4.7}$$

and similarly for the other two dimensions. z_0 gives the axial distance from the trap center to an endcap. For linear Paul traps, typical trap frequencies are on the order of Megahertz, and trap depths are on the order of tens of electron volts. This means that a particle at room temperature (which has a kinetic energy of millielectron volts) is trapped in such a trap.

4.2 Simulating ion-trap potentials with CPO and Matlab

For a given geometry of Paul-trap electrodes, one wants to know the shape of the trapping potential, trap frequencies, and the trap depth. For cases in which the electrodes do not form a perfect quadrupole geometry, this calculation is done by numerical simulations.

Here, simulations of ion-trap designs are performed using CPO[1] and Matlab. We specify the geometry of all trap electrodes in CPO, and the program solves the electromagnetic-field equations for each trap electrode numerically. The potential of each electrode is calculated by applying unit voltage on this electrode and zero on all other electrodes.CPO uses the boundary element method, a numerical computational method of solving linear partial-differential equations. Fibers are simulated in CPO as dielectric cylinders without charges.

The RF pseudopotential Φ_{RF} is calculated from the potential V_{RF} on the RF blades using Matlab. The field is calculated via the gradient of the potential.

$$\begin{aligned} E_{\mathrm{i}} &= \partial_{\mathrm{i}} V_{\mathrm{RF}}, \\ E^2 &= \sum_i E_{\mathrm{i}}^2, i = x, y, z, \\ \Phi_{\mathrm{RF}} &= \frac{Q^2 E^2}{4 M \Omega^2}; \end{aligned} \tag{4.8}$$

with the ion's charge Q and its mass M. The RF pseudopotential and the potentials of the DC-electrodes are then combined to give the net potential over the trapping region. The DC-electrode potentials are multiplied with the voltage that is applied on the electrode and all potentials are added (Spl09).

The shape of the potential is analyzed by finding the trap axes and generating plots. The trap frequencies and trap depth are calculated in Matlab from the net potential. To calculate the trap frequencies $\omega_{\mathrm{i}} = \sqrt{\frac{k_{\mathrm{i}}}{M}}$, a parabola is fitted to the trap potential for all three dimensions, and the parameter k_{i} is determined by the fit.

4.3 Trap design options

An important early step in this thesis work was the development of an ion-trap setup in which an FFPC could be integrated. In order to be able to choose the most promising ion-trap candidate from a variety of options, four realistic ion-trap designs were developed and the potentials were simulated. First, the results of the three designs which we did not choose for our experimental setup are presented. The simulation of the fourth design, which is implemented in the experiment, is presented later, in Sec. 4.4.

A reasonable trap depth and low ion-heating rates both contribute to long ion lifetimes and are therefore among the most important selection criteria. The heating rate increases with decreasing ion-electrode distance (Tur00). For comparable trap dimensions and applied RF voltages, three-dimensional traps are considerably deeper than two-dimensional traps. Furthermore, it is advantageous if the trap geometry is such that it shields the ion from any charges on the fibers, and additionally, it should be

---

[1] CPO Ltd. Charged Particle Optics programs - www.electronoptics.com

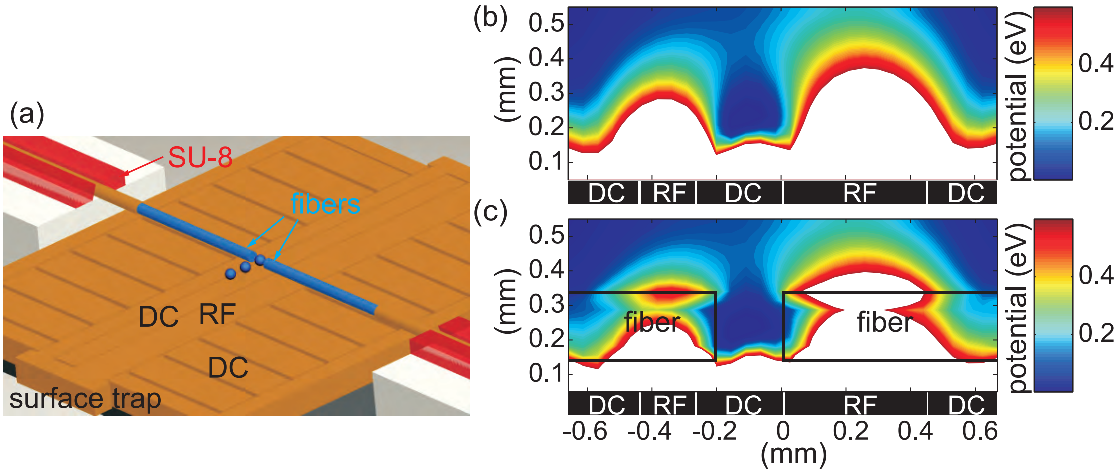

Figure 4.1: (a) Technical drawing of a surface ion trap with an FFPC integrated on the chip. The fibers are fixed on piezo actuators with SU-8 photoresist structures. (b) Effective trap potential of the planar trap. The RF electrodes have different widths to tilt the trap axes and thereby avoid having one of the axes orthogonal to the surface. The ions are stored 250 µm above the trap surface in a trap of roughly 0.2 eV depth. (c) Trap potential of the same surface trap along the axis of the dielectric fibers. The potential is distorted at the position of the fibers but the trap depth remains on the order of 0.2 eV.

possible to compensate for those charges, i.e., through the application of compensation voltages.

4.3.1 Planar trap with fibers parallel to the surface

Planar ion traps fabricated on microchips are promising candidates for scaling up ion-trap quantum computers (Sei06). Furthermore, multiple FFPCs can be integrated along the trap axis to couple different ions to different cavity modes.

In this first design, the fiber cavity is integrated with a planar trap, similar to the atom-chip design with an integrated FFPC of Ref. (Col07). The two RF electrodes have different widths. This geometry tilts the trap axes such that efficient cooling of the ion's motion with a laser beam parallel to the surface is possible. The various DC electrodes are used to compensate micromotion of the ion, move the ion along the trap axis, adjust the trap frequencies, and compensate for charges on the dielectric fibers.

As indicated in Fig. 4.1(a), the fibers are mounted parallel to the surface and orthogonal to the RF rails. Piezoceramic actuators stabilize the cavity length and also hold the fibers. The fiber mounts are fabricated on the piezos from SU-8 photoresist. Photoresist allows for precise alignment of the fibers via lithographic methods (Liu05). To avoid distortion of the ion's trapping potential from voltages on the piezo surface, the upper surface of the piezo actuator remains grounded, and high voltage is applied to the lower surface. The copper coating of the fibers would short the RF potential and is therefore etched back to 3 mm behind the fiber tip.

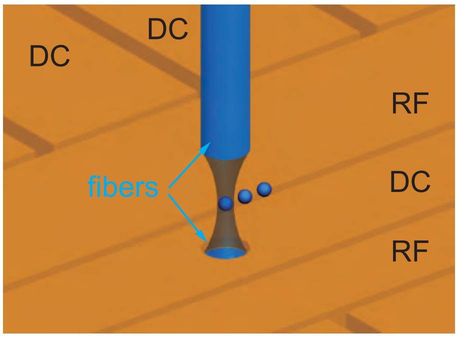

Figure 4.2: Technical drawing of a surface trap with an FFPC integrated orthogonally to the trap surface. The two RF electrodes, the center DC electrodes, and the segmented DC electrodes of the trap are shown. The first fiber sits inside a hole of the center DC electrode in the surface trap, and the second fiber is brought in from above.

Fig. 4.1(b) shows the potential of this planar trap without fibers. When the trap is driven with 100 V RF amplitude at a frequency of $2\pi \times 40$ MHz, the effective trap depth is on the order of 0.2 eV, and the ions are trapped 250 µm above the surface. This height is determined by the dimensions of the ion trap and is on the order of the width of the ground rail and the RF rails. Fig. 4.1(c) shows the simulated trapping potential of the same trap with an FFPC around the ion's position. While the potential shape is altered by the fibers, the depth remains on the order of 0.2 eV.

Advantages and disadvantages

With lithographic methods it is possible to produce precise and small planar trap structures with dimensions comparable to the fiber cavity. The technology to fabricate such surface traps is available in our laboratories. With this design, it is relatively easy to align the ions with respect to the cavity mode; the segmented DC electrodes in surface ion traps make it possible to steer an ion into and out of the cavity mode. However, the height of the RF minimum above the surface is determined by the trap geometry and cannot be moved. Therefore, the cavity mount must be adjustable along this axis, which could be achieved by adding piezo actuator stacks below the cavity mount.

Probably, the biggest disadvantage of this trap design is the shallow potential of only a fraction of an electron volt. Any additional charges on the fibers would shift the trapping potential and thus the ion's position significantly, especially because this trap geometry does not provide shielding of the ions from any charges on the fibers. Furthermore, the planar trap limits the optical access to the plane of the surface, and the fibers reduce this access further.

4.3.2 Planar trap with fibers orthogonal to the surface

The second design integrates the fiber cavity orthogonal to the surface of a small planar trap. The first fiber sits below a hole in the surface of the trap while the second fiber is mounted from above the trap, as shown in Fig. 4.2. The height of the ion above the surface of the trap should coincide with the waist of the cavity. Therefore, the ion should sit roughly 100 µm above the surface as our FFPCs can have lengths of up to 200 µm (Sec. 5.4.1). Thus, as the height of the ion above the trap surface is determined by the trap dimensions, the widths of the DC and the RF rails have to be on the order of 100 µm as well. To minimize the effects of the hole on the trap, its diameter at the surface is the same as the effective diameter of the fiber mirror (≈ 60 µm, Sec. 5.2.2), and the trap has an undercut with the same diameter as the fiber.

The dielectric upper fiber does not change the potential significantly. The hole in the rail, however, does. Therefore, it is advantageous to choose the dimensions of the trap such that the ion sits above a dielectric part of the trap, e.g., the gap between RF and DC electrodes. In this case, the cut-out for the fiber mirror would leave the potential unchanged.

Advantages and disadvantages

As stated in the first design, the surface trap allows for easy translation of the ions along the trap axis and thus into and out of the cavity mode. For this geometry, it needs to be possible to translate the fibers along the plane orthogonal to the trap axis. The direction of the cavity axis is controlled via the piezos which stabilize the cavity length. Along the second axis, the cavity mount needs to be transferrable via additional piezos.

The surface trap could be produced with high accuracy via lithographic methods in our laboratories. The technical challenges of this design, however, are the production of the hole through the trap as well as the stable mounting of the fiber from above. The undercut and the small hole could possibly be machined via laser machining, and the fibers could be mounted on a robust bridge. The main disadvantage of this design would then be the shallow trapping potential. Additionally, we expect the heating rates to be relatively high due to the small ion-electrode separation of only 100 µm. Furthermore, the trap surface and the fiber mount would limit the optical access.

4.3.3 Cylindrical tip trap

The design of the cylindrical tip trap is shown in Fig. 4.3(a). It is similar to the designs described in (Ste13, Wil11, Mai09). An ion is trapped halfway between two thin DC-electrode tubes. Two additional cylindrical electrodes around the DC electrodes are connected to an RF voltage. To isolate RF and DC electrodes, the two cylindrical electrodes have a small gap between them. Micromotion is compensated via additional rod-shaped electrodes around the RF cylinders. In this design, the fibers are threaded through the inner DC electrodes.

Fig. 4.3(b) shows the simulated potential for a trap in which the center DC electrodes have an inner diameter of 220 µm and an outer diameter of 320 µm, and the RF electrodes have an inner diameter of 400 µm and an outer diameter 700 µm. The DC electrodes are separated from one another by 200 µm, and the RF electrodes are shifted back by 50 µm with respect to the DC electrodes. When an RF voltage of 100 V amplitude at a frequency of $2\pi \times 40$ MHz is applied, the effective trap depth is calculated to be about 0.2 eV.

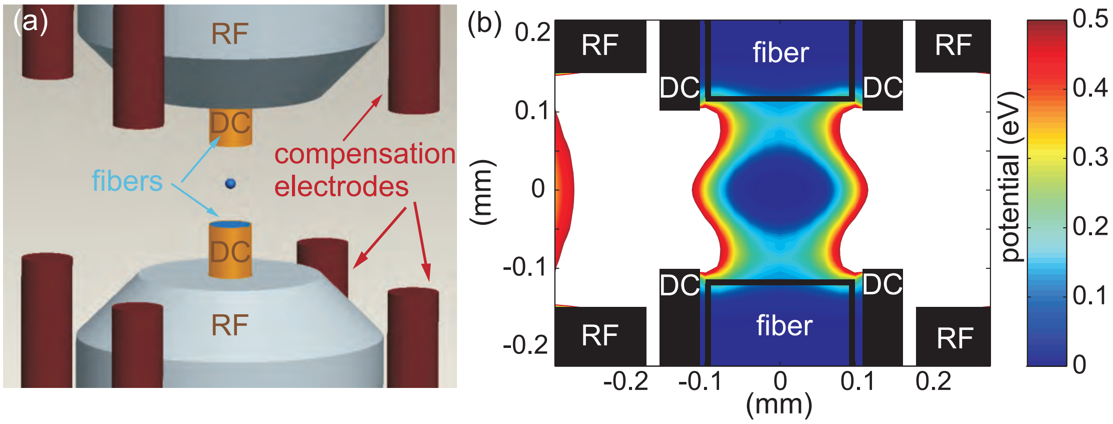

Figure 4.3: (a) Technical drawing of a cylindrical tip trap. The ion is confined via two RF and two DC cylinders, and a small gap between the cylinders isolates RF and DC electrodes. The fibers sit inside the DC electrodes. (b) Trapping potential simulated with CPO and Matlab. The trap has a depth of about 0.2 eV when driven with an RF amplitude of 100 V at $2\pi \times 40$ MHz frequency.

Advantages and disadvantages

One advantage of this design is that the center DC electrodes shield the ion from the fibers, which therefore do not change the trapping fields. Furthermore, the design offers good optical access. Additionally, the mirror surfaces can be recessed slightly behind the center electrodes to shield them from the calcium beam produced by the oven while loading ions.

In this trap, however, it is not possible to trap a linear chain of ions, and the ion's position is fixed by the trap geometry in all three dimensions. This fact suggests that the fibers need to be aligned independently of the electrodes in all three dimensions to ensure that the ion's position can be overlapped with the cavity mode. Furthermore, the fibers should be adjustable with respect to each other to guarantee that it is possible to align a cavity. This task is difficult due to the small dimensions of both fibers and electrodes.

4.4 Linear blade trap

The design that we have chosen to implement in the new apparatus is a linear blade trap. It consists of a trap similar to those described in (Gul03, Rie05), integrated with an FFPC orthogonal to the trap axis. The trap is set up from four blade-shaped electrodes which generate the pseudo potential in radial direction. Two endcap electrodes confine the ion along the trap axis, and four rod-shaped compensation electrodes parallel to the trap axis are used to compensate micromotion. The main differences of the new trap to the 'standard' design are that the trap is miniaturized and, instead of 90° angles, it has angles of 60° and 120° between the trap blades. The exact geometry is specified in Sec. 7.1.1. In this section, the trap potential of such a linear blade trap is discussed.

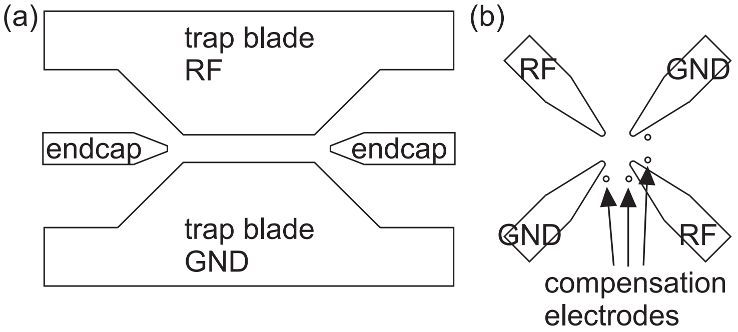

Figure 4.4: Schematic drawing of a linear Paul trap. (a) Side view of the linear trap. Two of the blades and the endcap electrodes can be seen. (b) View along the trap axis. The four trap blades and the two pairs of compensation electrodes are shown.

Advantages and disadvantages

The main advantage of a three-dimensional trap is its deep trapping potential. The 'standard' linear blade traps, with heating rates as low as a few quanta per second and trap depths on the order of tens of electron volts, are known to have ion lifetimes on the order of days or even weeks (Roh01, Ben08). Furthermore, the linear blade trap allows for trapping ion strings and for moving ions in and out of the cavity field along the trap axis. In the direction perpendicular to the fiber cavity and the trap axis, however, the cavity must be adjustable with respect to the ion to allow alignment of the cavity mode with respect to the ion.

A way to shield the ion from the fibers is to keep the fibers behind the trap blades. Therefore, the distance between trap blades should be comparable to the length of the fiber cavity (~ 200 µm). It is challenging to achieve low tolerances for such a small trap using standard machining tools for fabrication.

4.4.1 The 'standard' linear blade trap

Here, a 'standard' linear trap similar to the ones used in current experiments in our research group is simulated. The design is presented in (Gul03, Rie05) and shown in Fig. 4.5. The following trap parameters are used for simulations: the distance between two opposing blades is 1.6 mm, and the distance between the endcaps is 6.4 mm. The compensation electrodes are 1.5 mm away from the trap center.

The trap is driven with an RF frequency of $2\pi \times 24$ MHz at an amplitude of 1100 V (thus $q = 0.27$). The endcap electrodes are held at a potential of 500 V. Fig. 4.4(a) shows the trap potential in the plane orthogonal to the trap axis. The potential depth in this radial plane of the trap is 20 eV, and the radial trap frequencies are $\omega_{\mathrm{r}} = 2\pi \times 6$ MHz.

In Fig. 4.4(b), the effect of one pair of the compensation electrodes is shown. The figure shows the DC potential of 10 V applied to the compensation electrodes to the right of the trap center. When this potential is added to the total effective trap potential, the trap center is shifted to the left. Similarly, a positive DC potential on the compensation electrodes above the trap center would shift the ions down.

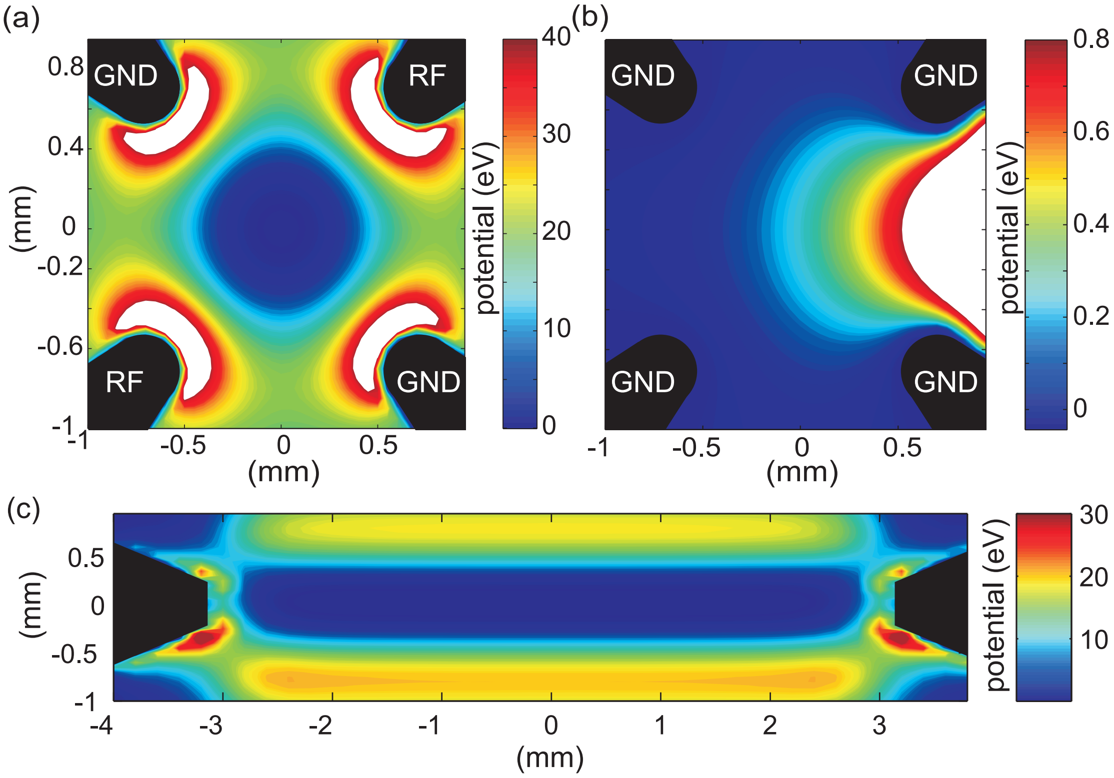

Figure 4.5: (a) Radial trap potential of the linear blade trap. In black, the tips of the blade electrodes are shown. Driving the trap at an RF frequency of $2\pi \times 24$ MHz and an amplitude of 1100 V, the trap depth is on the order of 20 eV. The trap frequency in radial direction is $\omega_\mathrm{r} = 2\pi \times 6$ MHz. (b) DC potential of 10 V applied to the compensation electrodes along the horizontal axis. The electrodes shift the DC minimum along the horizontal axis. (c) Effective axial trap potential with 500 V on the endcap electrodes. The endcap electrodes are shown in black. The axial trap frequency is $\omega_\mathrm{z} = 2\pi \times 2$ MHz

Fig. 4.4(c) displays the potential along the trap axis. In this direction, the trap frequency is $\omega_\mathrm{z} = 2\pi \times 2$ MHz.

4.4.2 The miniaturized linear blade trap

As the distance between the trap center and the blade electrodes is decreased, the stability parameter q increases according to Eq. 4.3. To maintain a stable trapping configuration, either the RF potential has to be decreased or the frequency of the RF has to be increased. Both changes lead to a decrease in trap depth. Therefore, the trap depth of a miniaturized blade trap is smaller than that of the 'standard' trap.

An ion trap with a separation of 340 µm between two opposing blades has a q-value of 0.32 when driven at a frequency of $2\pi \times 35$ MHz and an amplitude of 130 V. With an endcap electrode separation of 2.8 mm and a potential of 200 V applied to the electrodes, the calculated trap potential is then 2 eV deep. The radial trap frequencies are $\omega_\mathrm{r} = 2\pi \times 10$ MHz and the axial trap frequency is $\omega_\mathrm{z} = 2\pi \times 2$ MHz. The same trap drive values are used for all following simulations of the miniaturized linear trap.

4.4.3 Changing the angle between the blades

In the simulations described above, the four blades are positioned symmetrically, with 90° angles between RF and ground blades. Increasing the angle between neighboring blades in the direction of the FFPC adds additional space for the fibers, so that the fibers can be brought closer to the blades and thus shorter cavities are possible. In the setup that we have implemented, we use a trap with a 120° angle between the pairs of blades that shield the fibers. As a consequence, the angle between the blades along the orthogonal direction is 60°.

Fig. 4.6 shows the trap potential in the radial plane for traps with different angles between neighboring blades. The RF trap depth decreases as the angles become more asymmetric, but at the same time, the influence of the DC endcap potential increases. Therefore, the overall trap depth does not change significantly.

For a symmetric trap, in which all blades have 90° angles with respect to each other, the two radial trap frequencies are degenerate: $\omega_\mathrm{r} = \omega_{r1} = \omega_{r2}$. As this symmetry is broken by changing the blade angles, the radial trap frequencies are no longer degenerate. For the case of the 120°/60° angles, the trap frequencies differ by 3%. Table 4.1 summarizes the results of the simulations for the four trap configurations shown.

Furthermore, as the angles are changed to a more asymmetric configuration, the effect of the compensation electrodes changes. At the side, where the angle between the blade electrodes opens, the compensation electrodes have a larger effect on the ions, whereas on the side, where the angle closes, the compensation electrodes have less effect on the ions. This is due to shielding of the compensation electrodes by the blade electrodes.

4.4.4 Adding dielectric fibers

The mirror-coated fibers forming the Fabry-Perot resonator are made of fused silica. This material has a dielectric constant of $\epsilon = 3.8$, which is the same for the fiber core and the fiber cladding. The fibers have a diameter of 200 µm. Fig. 4.7 shows the change of the ion-trap potential introduced by these fibers for different fiber separations.

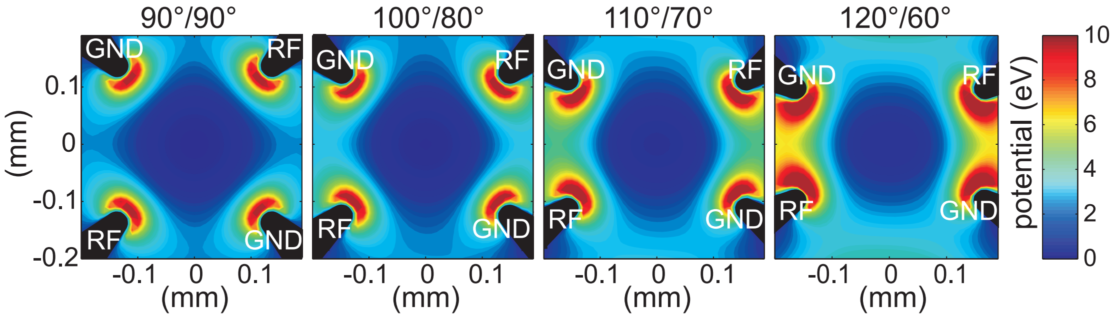

Figure 4.6: Trap potential for angles of 90°/90°, 100°/80° 110°/70°, and 120°/60° between the trap blades. While the depth of the RF potential decreases with increasing angle ratio, the influence of the DC potential from the endcap electrodes increases. Thus, the overall trap depth stays roughly constant for the four different geometries.

Table 4.1: Trap depth and trap frequencies ω_r and ω_z as a function of the angles between the trap blades. Furthermore, the distance between neighboring blade tips is calculated. While the distance d_f increases for the axis along which the FFPC is mounted, the distance d_nf along the second axis decreases.

angles	d_f (µm)	d_nf (µm)	RF trap depth (eV)	trap depth (eV)	ω_r (MHz)	ω_z (MHz)
90°/90°	240	240	2	2	$2\pi \times 10$	$2\pi \times 1.7$
100°/80°	260	219	1.2	2	$2\pi \times 10$	$2\pi \times 1.8$
110°/70°	279	195	0.9	2	$2\pi \times 10$	$2\pi \times 1.9$
120°/60°	294	170	0.7	2	$2\pi \times 10$	$2\pi \times 2.2$

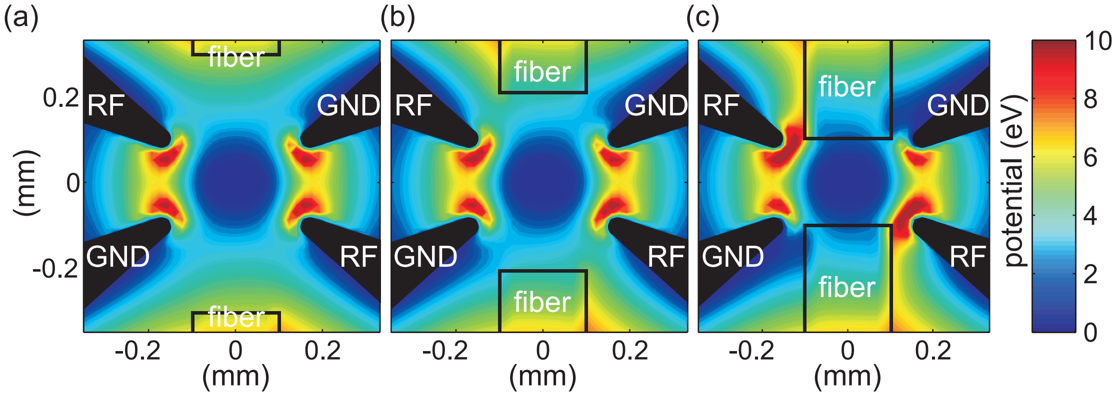

Figure 4.7: Trap potential for the miniaturized linear blade trap with a dielectric fiber pair at separations of (a) 600 µm, (b) 400 µm, and (c) 200 µm.

Table 4.2: Trap depth and trap frequencies ω_{r1}, ω_{r2}, and ω_z of the miniaturized linear blade trap for different cavity length L.

L (µm)	trap depth (eV)	$(\omega_{r1}, \omega_{r2})$ (MHz)	ω_z (MHz)
600	2	$2\pi \times (10, 10)$	$2\pi \times 1.9$
400	1.9	$2\pi \times (10, 10)$	$2\pi \times 1.9$
200	1.3	$2\pi \times (9.6, 9.9)$	$2\pi \times 1.9$

The asymmetry in the potential stems from the fact that the fibers shift the DC field from the endcap electrodes. Therefore, the trap depth in the radial plane decreases as the fiber separation decreases. In the axial direction, the potential is not altered significantly. Table 4.2 summarizes the results of the simulations for cavity lengths of 600 µm, 400 µm, and 200 µm.

These simulations only take into account the dielectric material of the fiber. Charges that accumulate on the dielectric under vacuum are not included in the simulations because, assuming such charges are present, the amount of and temporal stability of such charges are unknown.

4.4.5 Adding a coating to the fibers

The fibers in the experimental setup are coated with a protective layer of copper, which is grounded. The copper is etched back from the fiber tip by about 200 µm. Simulations show that the trap potential is influenced by this coating. As the distance of the copper from the fiber tip decreases, the change in the ion-trap potential increases. This is shown in Fig. 4.8(a) and (b). The coating of both fibers starts 200 µm and 100 µm behind the fiber tips, respectively. The copper coating acts as an additional ground electrode in the trap geometry and thus changes the trapping field. For the case that the fibers have an asymmetric coating, the potential change is asymmetric as well; see Fig. 4.8(c).

The simulations were done for a cavity length of 400 µm and distances of 200 µm and 100 µm between the fiber tip and the copper coating. Table 4.3 summarizes the

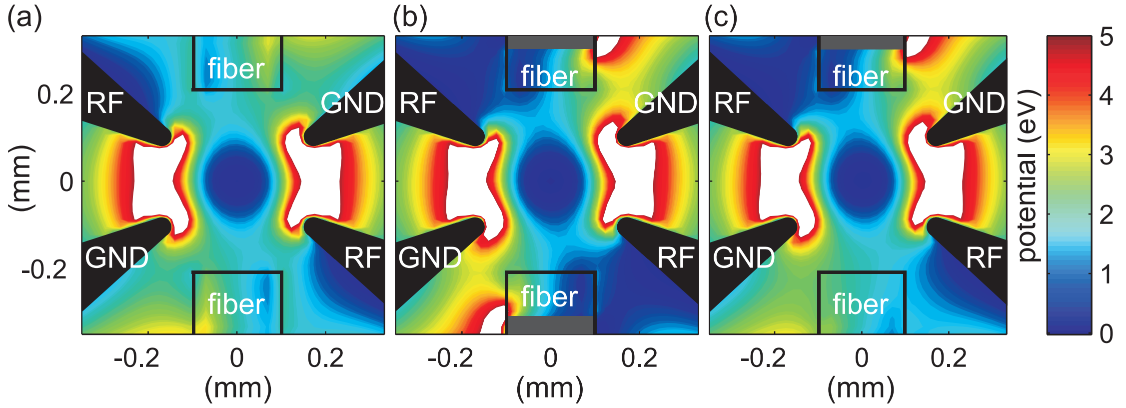

Figure 4.8: Ion-trap potential of the miniaturized linear blade trap including dielectric fibers with a conductive coating. The coating is indicated in grey. (a) The fiber coating starts 200 µm behind the fiber tips. (b) The coating starts 100 µm behind the tips. (c) The coating starts 200 µm behind the tip of the lower fiber and 100 µm behind the tip of the upper fiber.

Table 4.3: Trap depth and trap frequencies ω_{r1}, ω_{r2}, and ω_z for a miniaturized linear blade trap with a 400 µm long FFPC. The fibers have a copper coating which starts at a distance l_{c1} and l_{c2} behind the fiber tips of fiber one and two, respectively.

l_{c1} (µm)	l_{c1} (µm)	trap depth (eV)	(ω_{r1}, ω_{r2}) (MHz)	ω_z (MHz)
200	200	1.2	$2\pi \times (8.8, 11)$	$2\pi \times 2.3$
100	100	0.8	$2\pi \times (8.6, 11)$	$2\pi \times 2.5$
100	200	0.8	$2\pi \times (8.7, 11)$	$2\pi \times 2.3$

simulation results. One sees that the trap potential in the radial plane is decreased by the coating. The coating of the fibers changes both radial trap frequencies ω_{r1} and ω_{r2} by around 10%. Furthermore, the axial trap frequency increases.

For the case of a fiber separation of 400 µm, the simulation does not show a shift of the position of the trap center. A second set of simulations for smaller cavity length, however, shows that the minimum moves toward the fiber which has the coating closer to the fiber tip.

4.5 Conclusion and discussion

From these simulations, we learn that miniaturized linear Paul traps are well suited for the experiments with a fiber cavity. Such traps provide deep trapping potentials and offer flexibility for integrating a fiber cavity. The effect of changing the angles between the blades starts playing a role as soon as fibers and grounded coatings are considered. Furthermore, the influence of the compensation electrodes changes significantly for the two radial directions.

While the coating close to the fibers tips may reduce effects of charges on the dielectric, it influences the potential of the ion trap. Furthermore, asymmetric coatings on the two fibers lead to an asymmetry of the trap potential and therefore should be avoided.

The construction and performance of the miniaturized linear trap is presented in Chap. 7. In the following, fiber cavities, suited to be implemented with such a trap, are presented.

5 Fiber-based Fabry-Perot resonators

Microfabricated optical cavities have several advantages over conventional cavities in cavity-QED experiments. Microcavities offer access to small mode volumes and thus high interaction rates of atoms with cavity photons. Furthermore, they provide flexibility in experimental setups, in which small mirrors are often easier to implement than centimeter-scale mirrors fabricated on superpolished substrates. The small size also facilitates the integration of two or more cavities in one setup. In the future, it may be possible to construct microcavity arrays in scalable systems.

This range of advantages has motivated development of microcavities using various technologies. There are three main criteria for microcavity development: surfaces with small radii of curvature, surface roughnesses that are low enough to not contribute significantly to the mirror losses, and surfaces to which a low-loss mirror coating can be applied, i.e., by ion-beam sputtering. A measure of the mirror quality in a cavity is the finesse as defined in Sec. 5.1.1. Surfaces that fulfil these requirements are produced by silicon wet-etching (Tru05), by enclosing nitrogen bubbles in borosilicate and polishing away the bubbles' upper half (Cui06), or by transferring a coating produced on a microlens onto an optical fiber (Ste06, Mul09). All of these approaches have been used to produce cavities with moderate finesses of up to 6×10^3. Recent developments in the fabrication of glass microcavities by shaping surfaces with controlled re-flow of borosilicate glass yielded finesses of up to 3.2×10^4 (Roy11). However, the best microcavity finesse to date of 1.5×10^5 (Mul10) has been measured with a cavity constructed from coated, concave optical-fiber facets shaped by CO_2-laser ablation (Hun10).

In this process, a short pulse of focused CO_2-laser light is absorbed in the cleaved tip of a fiber and creates a depression by locally evaporating the material. A highly reflective coating is then applied to the shaped fiber surfaces by ion-beam sputtering in a high-vacuum environment. Fiber-based Fabry-Perot cavities produced in this way are currently used in atom-chip setups, in which strong coupling to a Bose-Einstein condensate has been shown (Col07). As these fiber cavities seem to be the most promising candidates for high-finesse microcavities, we decided to use this technology to produce microcavities suitable for the implementation with an ion trap. Both the production of FFPCs and the ion-trap implementation constitute my thesis work. Currently, implementations of FFPCs with solid-state emitters (Mul10), ion traps (Ste13, Wil11, Van10), and neutral atoms are being developed in several research groups worldwide.

Previous work on fiber cavities had focused on their implementation into atom-chip experiments (Col07). For neutral atoms, the presence of fibers does not influence the trapping potential seen by the atom, and so short cavities are favorable as they provide a small mode volume. To implement fiber cavities with ion traps, in contrast, it is crucial to separate the fibers and the ions sufficiently so that the ions' trapping potential is not distorted by the dielectric mirrors (Sec. 4.4.4).

This chapter reviews the theory about Fabry-Perot cavities necessary for understanding the presented results presented. The recent development of FFPCs suitable for integration with ion traps is shown, and the production process of the coated fibers as well as useful fiber-handling techniques such as a method for fiber-mirror cleaning are explained. In addition, cavity-alignment methods, finesse measurements, the active cavity stabilization, and alignment stability issues of long fiber cavities are described. Furthermore, the cavity losses due to surface roughness, the coupling efficiency between fiber and cavity, and the cavity birefringence are characterized.

The shaping of fibers with the CO_2-laser ablation process was done in collaboration with Jakob Reichel and his research group at the École Normale Supérieure in Paris. This setup is a second-generation apparatus developed by Christian Deutsch during his master's thesis work (Deu08). The fibers were coated by the company Advanced Thin Films in Boulder, Colorado. In the company's cleanroom, I helped with the fiber preparations for the coating process and made sure that the fibers remained clean and were handled correctly. The FFPC alignment setup and measurement routines were developed with the help of Tracy Northup. Andrew McClung helped with cavity tests and fiber splicing, and Klemens Schüppert developed the birefringence measurements with my help in the course of his master's thesis.

5.1 Cavity theory

Here, the theory of Fabry-Perot resonators and FFPCs is summarized. Further details about optical-resonator theory can be found in Ref. (Mil88), and more specialized theory on FFPCs is found in (Deu08, Hun10).

5.1.1 Fabry-Perot cavities

An optical Fabry-Perot resonator consists of two opposing mirrors that confine light to a defined volume between them. The cavity field forms a standing wave with intensity maxima and minima separated by one quarter of the wavelength λ. The resonance condition is fulfilled if the cavity length L corresponds to an integral multiple of half the wavelength: $L = n\lambda/2$. The free spectral range ν_{FSR} is defined as the frequency spacing between two successive longitudinal modes of the cavity and is given by $\nu_{\mathrm{FSR}} = c/2L$, while $\delta\nu$ is the full width at half maximum (FWHM) of a resonance peak.

Each cavity mirror can be characterized by its reflectivity $\mathcal{R}$, its transmittivity $\mathcal{T}$ and its losses $\mathcal{L}$, with $\mathcal{R} + \mathcal{T} + \mathcal{L} = 1$. The mirror losses are the sum of scattering and absorption losses of the reflective coating, and the total losses from the cavity $\mathcal{L}_{\mathrm{tot}}$ in case of identical mirrors are defined as the sum of both mirror losses $\mathcal{L}_{\mathrm{tot}} = 2(\mathcal{T} + \mathcal{L})$.

The finesse $\mathcal{F}$ of an optical resonator is defined by the free spectral range divided by the FWHM,

$$\mathcal{F} = \frac{\nu_{\mathrm{FSR}}}{\delta\nu}. \tag{5.1}$$

The finesse is a measure of the quality of the mirrors, and can also be written as a function of the total mirror losses $\mathcal{F} = \pi/\mathcal{L}_{\mathrm{tot}}$. For increasing losses, the finesse decreases. $\mathcal{F}$ is not a function of the length of the resonator. In contrast, the quality factor $Q = \nu/\delta\nu$ is a function of the resonant frequency ν and thus depends on the cavity length. A high quality factor indicates a low loss rate with respect to the amount of energy stored in

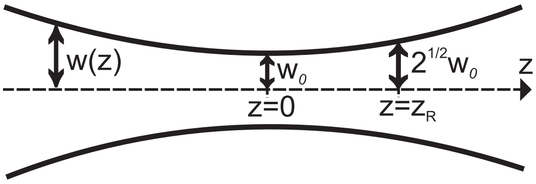

Figure 5.1: Variation of the beam radius $w(z)$ of a Gaussian beam. The Gaussian beam propagates along the z-axis. $z = 0$ corresponds to the position at which the beam has its minimum spot size w_0 called waist. At the Rayleigh length $z = z_\mathrm{R}$, the beam diameter is $\sqrt{2}w_0$.

the resonator.

An electric field inside the cavity is reflected back and forth between the mirrors. If the field driving the cavity is switched off, the field inside the resonator decays exponentially as a result of transmission and mirror losses. The damping rate κ for the electric field is defined as

$$\kappa = \frac{1}{2\tau} = \frac{\pi c}{2\mathcal{F}L}, \tag{5.2}$$

where τ is the cavity ringdown time.

Assuming a Gaussian mode for the light field in the resonator, it is possible to calculate the mode radius also called spot size. The mode radius $w(z)$ of a Gaussian beam represents the radius of the beam at which the field amplitude drops to $1/e$ of its maximum value. As shown in Fig. 5.1, the beam waist w_0 is the minimum value of $w(z)$. The Rayleigh length is defined as the distance z_R from the beam waist where the spot size $w(z_\mathrm{R}) = \sqrt{2}w_0$. The beam waist is calculated from the length L of the cavity and the radii of curvature R_1 and R_2 of the mirrors. For a symmetric cavity, in which both mirrors have the same radius of curvature R, the beam waist is

$$w_0 = \sqrt{\frac{\lambda}{2\pi}}(L(2R - L))^{\frac{1}{4}}. \tag{5.3}$$

Furthermore, it is possible to determine the spot size at each mirror by

$$w_\mathrm{m} = \sqrt{\frac{\lambda}{\pi}}\sqrt{\frac{LR}{\sqrt{(L(2R - L))}}}. \tag{5.4}$$

Knowing the length of a resonator and its waist, the mode volume of the resonator is calculated via:

$$V = \frac{\pi}{4}Lw_0^2. \tag{5.5}$$

The mode volume of the resonator determines the strength of the atom-cavity coupling (Eq. 3.5) and is therefore an important parameter in characterizing CQED experiments.

Clipping from the mirror edges

The field amplitude along the beam cross-section has a Gaussian profile, and thus, a considerable amount of the field is outside the mode radius $w(z)$. A Gaussian beam reflected off a mirror loses energy if it is clipped by the mirror's edge (Sie86). These clipping losses $\mathcal{L}_\mathrm{c}$ in a Fabry-Perot cavity are calculated from the mirror diameter $2\rho_\mathrm{m}$:

$$\mathcal{L}_\mathrm{c} = e^{\frac{-2\ \rho_\mathrm{m}^2}{w_\mathrm{m}^2}} = e^{-2\ \rho_\mathrm{m}^2 \frac{\pi}{L\lambda}\sqrt{1-\left(1-\frac{L}{R}\right)^2}}. \tag{5.6}$$

This equation is an empirical approximation to model the cavity losses. For cavities, these losses play a role as the beam spot size becomes comparable to the mirror size. For FFPCs, the mirror diameters are small, such that these losses might become relevant; see measurement in Sec. 5.4.1.

5.1.2 Coupling efficiency from a fiber to a resonator

The coupling efficiency from the Gaussian mode of a single-mode fiber with a concave mirror surface into the mode of a Fabry-Perot resonator is calculated as the overlap of the fiber mode with the cavity mode. The coupling efficiency ϵ_a is given by (Joy84)

$$\epsilon_\mathrm{a} = \frac{4}{\left(\frac{w_\mathrm{f}}{w_\mathrm{c}} + \frac{w_\mathrm{c}}{w_\mathrm{f}}\right)^2 + \frac{s^2}{z_{\mathrm{R_f}} z_{\mathrm{R_c}}}}, \tag{5.7}$$

with fiber mode waist w_f, cavity mode waist w_c and Rayleigh lengths $z_{\mathrm{R_f}}$, $z_{\mathrm{R_c}}$ of the beam exiting the fiber and of the cavity mode, respectively. The distance from the waist of the beam exiting the fiber to the waist of the cavity mode is denoted by s. In this formula, it is assumed that the mirror surface is orthogonal to the fiber core ($\theta = 0$) and that there is no mismatch between the core and the mirror center ($d = 0$). Here, $\theta = 0$ is the angle between the optical axes of the two beams, and d is the offset of the two beam axes with respect to each other; see also Fig. 2 of Ref. (Joy84).

A tilt of the fiber with respect to the mirror by a small angle θ reduces the coupling by a factor of $e^{-(\theta/\theta_\mathrm{e})^2}$. Similarly, a small displacement of the fiber core from the cavity axis reduces the coupling by a factor of $e^{-(d/d_\mathrm{e})^2}$, such that $\epsilon = \epsilon_\mathrm{a} e^{-(\theta/\theta_\mathrm{e})^2} e^{-(d/d_\mathrm{e})^2}$, where analytic expressions for angular tolerance θ_e and displacement tolerance d_e can be found in Ref. (Joy84). This calculation is plotted with realistic fiber parameters and cavity parameters in Sec. 5.4.2.

To calculate the coupling efficiency of a multimode fiber to the cavity mode, one has to compare the acceptance angle of the fiber with respect to the mode of the cavity. With typical numerical apertures of multimode fibers this coupling can be considered to be unity (Hun10).

5.2 Fiber handling and fiber-mirror production

The fibers we use to construct FFPCs are copper-coated single-mode and multimode fibers of 200 µm diameter. The use of this non-standard fiber size means that fiber connectors, cleaving tools, and splicing tools are harder to obtain. Here, techniques for fiber preparation and handling are summarized and the production process of the fiber mirrors is described.

5.2.1 Fiber preparation

As the fibers best suited for our vacuum requirements and for our cavity wavelength at around 860 nm, we chose copper-coated multimode (MM) and single-mode (SM) fibers of 50 µm and 6 µm core diameter[1]. To optimize the CO_2-laser ablation process (Sec. 5.2.2), the fibers have a cladding diameter of 200 µm.

Etching copper coating from fibers: The fibers need to be stripped properly before they are cleaved or connectorized. The copper is etched from the fiber over a length of a few millimeters with a 25% nitric acid (HNO_3) solution or an iron(III) chloride ($FeCl_3$) solution. The $FeCl_3$ is dissolved in water with a one to four mixing ratio and heated to 50°C, at which temperature the chemical process works fastest. We dip the fibers in the solution, and they are held in place by a jig sitting on the rim of the basin. The process is stopped once the coating is no longer visible, which usually takes a few minutes. The etching process with HNO_3 works faster but special care has to be taken with the strong acid.

Removing titanium from fibers: After the copper is etched, the glass fibers are still coated with a thin adhesive layer of titanium. This layer is not insulating, and if a fiber is in contact with multiple trap electrodes, the layer causes a short circuit between those electrodes. Furthermore, the titanium layer shifts the ion's trapping potential when it is brought close to the trap center. In Ferdinand Schmidt-Kaler's research group at the University of Mainz, the titanium layer of these fibers caused a short circuit between the RF and the DC electrodes of an ion trap[2]. In order to prevent short circuits, we scratch the titanium layer off mechanically with diamond paste[3] and then clean the fibers thoroughly with solvents.

Connectorizing fibers: Bare fiber ends are usually fixed inside fiber connectors which then provide the possibility to mount the fiber on a fiber-coupler lens system. Fiber-coupler lenses are needed to couple light in and out of a fiber. In the testing process, we often switch between fibers and thus prefer slide-on slide-off bare-fiber connectors[4] to connectors that needed to be glued. These connectors were custom-made for our non-standard 200 µm fibers. The drilling for the fiber in the connector, however, is 230 µm in diameter, 30 µm larger than the fiber diameter. This causes problems if the fiber needs to be aligned to the center of the ferrule, for example, for using fiber-to-fiber connectors. To avoid these problems, we also use permanent connectors[5], which are glued to the bare fibers.

Splicing non-standard 200 µm diameter fibers to standard 125 µm diameter fibers: At our institute, we have the possibility to splice fibers with a polarization maintaining fiber splicer[6]. The fiber splicer is used to merge two bare fiber ends. For this process, the fibers are aligned with respect to each other, heated via a filament, and pushed together. To be able to use standard fiber tools, such as vacuum feedthroughs or precise connectors, it is useful to work with 125 µm diameter fibers. We found that it was possible to splice the 200 µm diameter fibers to standard 125 µm diameter fibers of the

---

[1] IVG fiber, Cu800 − 200−custom and Cu50 − 200

[2] Ferdinand Schmidt-Kaler, personal communication

[3] Struers, DP-Paste P (1 µm)

[4] Bullet, Bare Fiber Adapter: NGB-FC230

[5] Thorlabs, 30126G2-205

[6] Vytran, FFS-2000

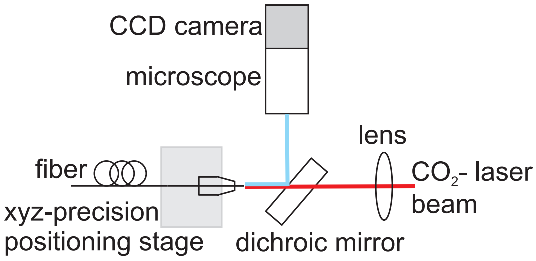

Figure 5.2: Schematic of the laser ablation setup (Deu08). The fiber is affixed to a v-groove that is aligned with respect to the laser beam by a three-axis micropositioning stage. The fiber facet is imaged via a dichroic mirror and a microscope onto a charge-coupled-device (CCD) camera. This image is used as an alignment tool to position the fiber in the center of the CO_2-laser beam. The CO_2 laser is focussed through a lens onto the fiber surface.

same core diameter. Properly performed splices showed negligible losses. In the splicing process, we accounted for the larger diameter of the 200 µm fiber by shifting the splice filament such that it preferentially heated this fiber. In the current experimental setup, however, we were able to use fibers which were not spliced because we have a home-built fiber feedthrough which can be used with non-standard diameter fibers (Sec. 7.3.1).

5.2.2 The CO_2-laser–ablation process

Reichel and his team have developed a method to machine concave surfaces on fiber facets using CO_2-laser ablation (Hun10). A short CO_2-laser pulse is focussed on the cleaved end of a fused-silica fiber. The pulse duration is around 10 ms, and the light has a wavelength of 10.6 µm. Most of the light is absorbed by the material, resulting in very efficient local heating and evaporation of the glass material. The shape of the structure that is generated is determined by the Gaussian intensity profile of the incoming laser beam. The radius of curvature and diameter of the depression are set by the pulse duration, power, and beam waist of the CO_2 laser. The surface that is created has a roughness of only (2.0 ± 0.1) nm (Hun10). Fig. 5.2 shows the CO_2-laser–ablation setup in Paris that was used to produce our fibers.

Ions are trapped more stably when dielectrics such as fibers are far from the ions and shielded from the trapping region. Increasing the separation L between the two mirrors of a cavity, however, increases the spot size of the cavity mode at the mirrors as a function of L and the mirrors' radii of curvature R (Eq. 5.6). If the mirror diameter $2\rho_\mathrm{m}$ is too small, the cavity mode is clipped at the mirror edge, which leads to losses $\mathcal{L}_\mathrm{c}$ at the edge of the cavity. For a conventional mirror, $2\rho_\mathrm{m}$ is the physical diameter of the mirror, whereas for a fiber mirror $2\rho_\mathrm{m}$, corresponds to the length scale of the depression created in the CO_2-ablation process. This length scale is bounded from above by the fiber diameter but is often much smaller.

One solution to the clipping problem is to try to produce large mirror structures on fiber tips. Thus, the focus of my work in Paris was to investigate ways to produce fibers with large mirror sizes and large radii of curvature. In order to produce larger

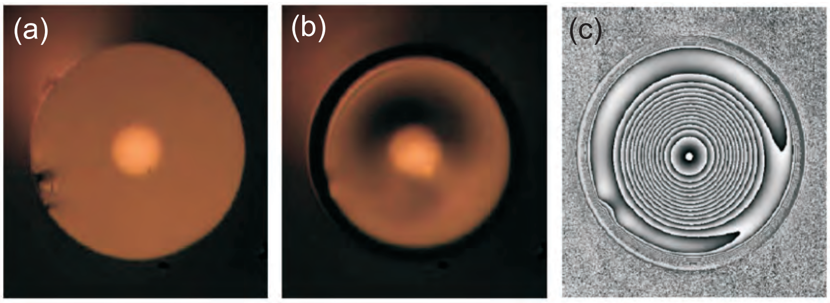

Figure 5.3: (a) Photo of a cleaved multimode fiber surface. (b) Photo of the same fiber after a CO_2-laser ablation pulse. The surface now has a concave depression. The photos were taken by the charge-coupled-device camera integrated in the ablation setup. (c) Phase profile of the fiber after ablation obtained from an optical profilometer. This phase profile is used to determine the mirror parameters, including ellipticity and radius of curvature.

structures, Deutsch and I found a new set of CO_2-laser parameters for the ablation process. Specifically, we increased the beam waist at the fiber tip and used higher CO_2-laser powers. Optimization of laser parameters is challenging because of a competition between two processes. On the one hand, the CO_2 light evaporates the fiber material, mapping the Gaussian beam profile onto a concave depression. On the other hand, the laser power is dissipated in the fiber tip, locally heating the material; the glass melts and forms a convex structure due to surface tension. To avoid the melting, heat needs to be conducted away efficiently by either cooling the fiber or creating a heat sink. Instead of standard 125 µm-diameter fibers, we used fibers of 200 µm diameter, where the additional glass functions as a heat sink.

Structures on the fiber tips were analyzed with an optical profilometer[7]. Fig. 5.3 shows a sample fiber surface before and after the ablation pulse as well as the profilometer image used to determine the structure parameters. In Fig. 5.4, the profilometer data are shown as well as fits to the data. The structure diameters $2\rho_\mathrm{m}$ and mirror depth z are extracted by fitting a polynomial to the profilometer data and finding its turning points. The radius of curvature R is extracted via the fit of a circle to the surface. The CO_2-laser–ablation structures are not spherical but have an elliptical shape. We determine the degree of ellipticity by identifying major and minor axis and comparing the radii of curvature. Note that R, $2\rho_\mathrm{m}$, and z are mean values of the fits to both axes.

For fibers previously machined in Reichel's research group, CO_2-laser waists between 18 µm and 80 µm and powers between 0.3 W and 1.1 W had been used, resulting in laser-machined structures with radii of curvature between 40 µm and 2 mm and structure diameters $2\rho_\mathrm{m}$ between 10 µm and 45 µm (Hun10). These fibers were used to produce short cavities, such as the 38.6 µm FFPC used to strongly couple a Bose-Einstein condensate to a cavity field (Col07). In contrast, during my stay in Paris, we produced fiber-mirror structures with a beam waist of 92 µm and a laser power of 4.6 W. The pulse duration was about 30 ms. As a result, the fiber surfaces had radii of

---

[7] Fogale: Microsurf3D

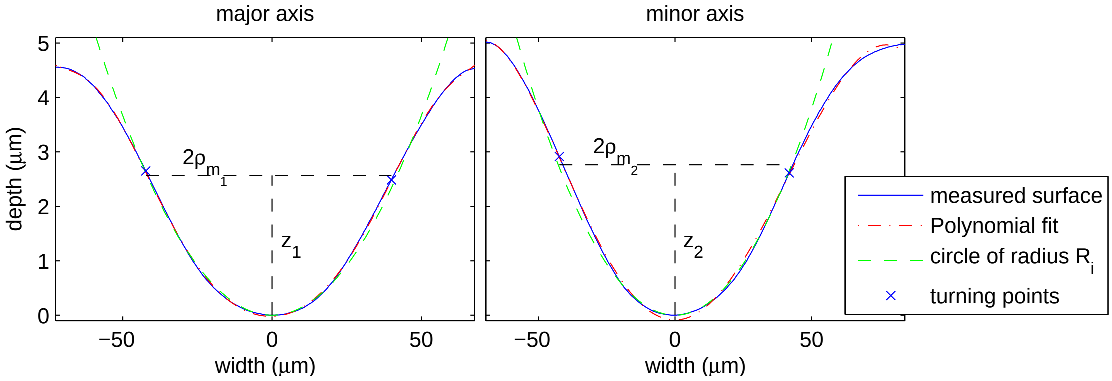

Figure 5.4: Fiber surface measured by optical profilometry; compare also Fig. 3 in Ref. (Hun10). The depression on the fiber surface is elliptical. Along the major and the minor axis ($i = 1, 2$) of the structure, we fit a polynomial and determine the structure diameter $2\rho_{\mathrm{m_i}}$ and the structure depth z_{i}. From a fit to a circle (note the different axis scales), we extract the radii of curvature R_{i}. Furthermore, the ellipticity of the depression and the mean values of the fit parameters R, $2\rho_{\mathrm{m}}$, and z are determined. For the surface in this figure, these values are: $2\rho_{\mathrm{m_i}} = (84, 82)$ µm, $z_{\mathrm{i}} = (2.8, 2.6)$ µm, and $R_{\mathrm{i}} = (332, 343)$ µm.

curvature of 180 µm to 420 µm and structure diameters of up to 80 µm. For a given set of production parameters, the structure parameters fluctuated on the order of 20%. With fiber mirrors produced with these parameters, we increased the length of the FFPCs up to 350 µm. Sec. 5.5 discusses possible improvements of the CO_2-laser ablation setup in order to produce shapes for even longer fiber cavities.

5.2.3 Mirror coating

After the ablation process, the shaped fibers were coated by the company Advanced Thin Films (ATF) with highly reflective mirror coatings optimized for the $4^2P \leftrightarrow 3^2D$ transition wavelength in $^{40}\mathrm{Ca}^+$. The coating is a multilayer dielectric stack produced via ion-beam sputtering. It consists of 37 alternating $\lambda/4$ layers of Ta_2O_5 and SiO_2, Ta_2O_5 being the first and the last layer. Fig. 5.5 shows the calculated transmission for the coating curve as well as a transmission measurement performed at ATF. The coating was designed to have maximum finesse at a center wavelength of 860 nm with a transmission of 15 ppm. Furthermore, the coating was chosen to correspond to a moderate finesse of 3×10^4 for 785 nm light, the wavelength at which the cavity length is actively stabilized. In total, 52 fibers and six superpolished reference substrates supplied by ATF were coated in the same coating run.

We chose a mirror coating with 15 ppm transmission. We had expected ~ 9 ppm scattering losses, and planned the transmission to dominate over these losses. Reichel's research group had calculated these scattering losses from a fiber-surface roughness of (0.2 ± 0.1) nm. This roughness had been measured in atomic-force-microscope measurements by Deutsch during his diploma thesis work (Hun10). Based on subsequent measurements, we now believe that the scattering losses due to surface roughness are

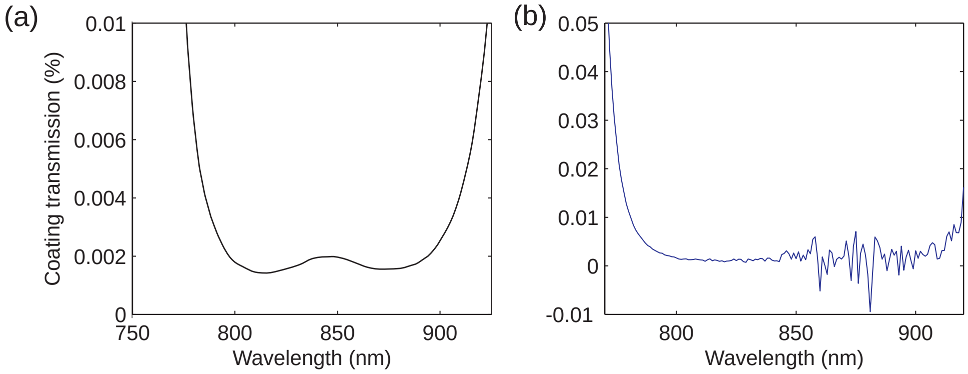

Figure 5.5: (a) Theoretical calculation of the mirror coating. The graph shows the design transmission versus the wavelength. (b) Spectrometer measurement of the coating's transmittance versus the wavelength. The noise in the spectrometer scan is due to a grating change at 861 nm. Courtesy of Advanced Thin Films.

only (3 ± 3) ppm (see Sec. 5.4.4) and would choose a less conservative coating with smaller transmission for the next coating run.

Highly reflective mirrors are typically annealed at 450°C to reduce defects in the coating that is, to reduce losses and increase the finesse. We did not anneal our fiber mirrors because the copper coating on the fibers oxidizes at those temperatures, which could possibly damage our fibers. Chap. 6 describes the annealing of mirror substrates and our attempts to anneal optical fibers.

A cavity constructed from mirrors with this coating show a finesse of 2.9×10^4 at 785 nm, which is the wavelength of the laser used for stabilizing the cavity length. The highest fiber-cavity finesse we have measured with fibers from this coating run was $(1.14 \pm 0.05) \times 10^5$ at 844 nm for a fiber cavity 70 µm in length. A finesse this high had not previously been observed for fiber cavities; the highest value of $\mathcal{F} = 3.7 \times 10^4$ had been measured in Reichel's research group (Col07). In the meantime, other groups have measured somewhat higher finesses of $(1.50 \pm 0.05) \times 10^5$(Mul10) by using mirror coatings of lower transmission.

5.2.4 Fiber mounting and transport

To protect the fibers from dirt or damage, they need to be mounted properly during every stage of the experimental process, e.g., in the coating chamber, during testing or in the vacuum apparatus.

We use two different kinds of holders for the fibers; the first is a brass cylinder with a slit in which the fiber is placed and is fixed by a spring[8]. Reichel's group uses holders with a similar design, although theirs are home-built. We mount the fibers in these holders after the laser-ablation process for storing and for the surface analysis (Sec. 5.2.2). In the coating chamber, however, the fiber holders need to be vacuum compatible, which brass is not. Therefore, a second holder was developed in which the fiber is protected

---

[8] Newport, FPH-S

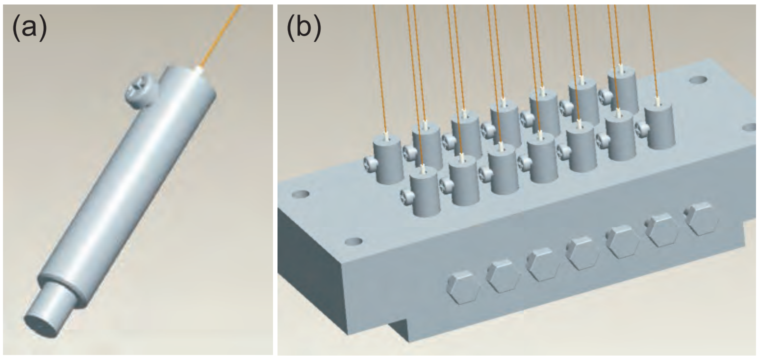

Figure 5.6: (a) Home-built fiber holder with teflon sleeve and screw for fixing the fiber. (b) Fiber jig for storage and transport of the fibers. Four of these fiber jigs fit onto the planetary mount of ATF's coating machine.

with a teflon sleeve and clamped with a screw inside an aluminum cylinder. Fig. 5.6(a) shows a drawing of such a holder. These holders were then used for the coating process and for fiber storage before and after coating. Care had to be taken not to break the fibers by tightening the screws too hard. For transport and storage, the fibers are fixed by their holders inside stainless-steel blocks which fit inside ATF's coating chamber (Fig. 5.6(b)). These blocks were mounted inside a box which protects the fibers from dirt at all times. During transport, handling, and storage, the fibers are always kept in cleanroom conditions. In the experience of the Reichel group, the coating of dirty fibers resulted in low finesses for the fabricated mirrors[9].

In setting up test cavities, the fibers should not be clamped rigidly with screws as it impairs the optical transmission. Therefore, in this case we do not use the fiber holders described above. Instead, we fix the fibers with magnets in stainless-steel v-grooves[10]; see also Fig. 5.7.

5.2.5 Cleaning fiber mirrors

To clean an ultra-low–loss mirror fabricated on a superpolished substrate, the mirror is rotated on a spin cleaner and its surface is swabbed successively with water, acetone and isopropyl alcohol during rotation (Nor08). The spin cleaner fixes the substrate with the mirror and rotates it. In our cleanroom, we use a spin coater[11] for this purpose. In contrast to macroscopic mirrors, fiber mirrors are too delicate to swab. The high-temperature gradient of the laser-ablation process makes the fiber tip brittle, and any stress or pressure usually breaks the tip.

One obvious strategy is to keep the fiber mirrors as clean as possible and to shield them from contamination. For this reason we store them in the cleanroom and usually mount them face down. Unfortunately, even in a clean environment, we have observed that the fiber mirrors sometimes decrease in finesse as they accumulate dust. To address this

---

[9] Reichel, personal communication

[10] Physik Instrumente (PI), F-010 Magnetischer Faserhalter

[11] SUSS, Delta 6 RC

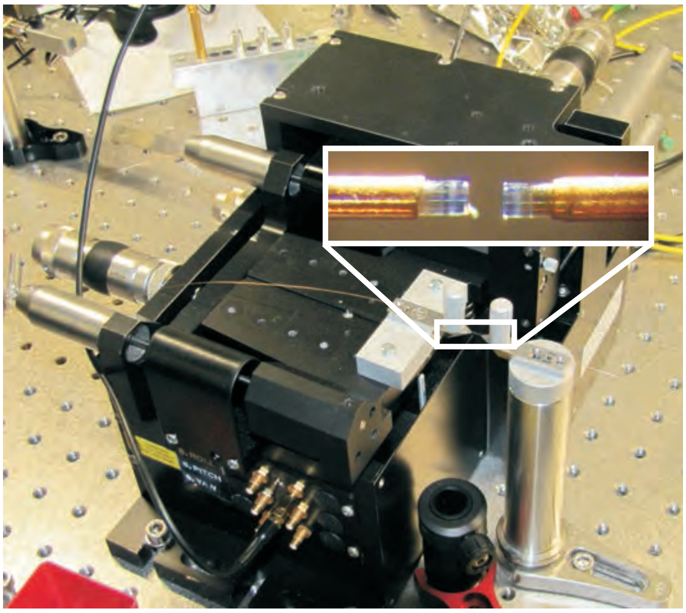

Figure 5.7: Photo of the six-axis positioning stage used to align FFPCs. One fiber (right) is fixed on a pillar post, while the other fiber (left) is aligned with micrometer precision in all three linear and all three angular degrees of freedom. The fibers are held by magnets inside v-grooves. The inset shows a magnified photograph of an FFPC. At the lower part of the left fiber, a small dust particle is visible. This particle, however, does not decrease the finesse as its distance from the mirror center is large enough.

problem, a cleaning procedure for ultra-low–loss fiber mirrors was developed. Holding them face-down in solvents from above, the mirrored fiber tips are cleaned in ultrasound for two minutes. We first use spectrophotometric grade acetone followed by methanol, both heated to 50°C. Immediately after taking the fiber out of the methanol, the mirror surface is dried by a flow of clean helium for at least half a minute.

There have been a few cases in which this method did not recover the initial finesse of a pair of fibers that had become dirty. However, typically, we see full recovery of the finesse by cleaning fiber mirrors with this procedure.

5.3 Building and measuring FFPCs

5.3.1 Aligning long FFPCs

Standard cavity-alignment techniques for cavities from conventional mirrors are not practicable for FFPCs as incoupling into the fiber is independent of cavity alignment. To obtain a cavity-transmission signal, it is usually sufficient to align the fibers by eye to form a very short cavity of about 30 µm in length. As the CO_2-laser ablation does not produce perfect surfaces — generally, the center of the depression is offset from the center of the fiber facet, and the mirror surface is not exactly orthogonal to the fiber core axis — the cavity has to be aligned further via optimization of the cavity transmission

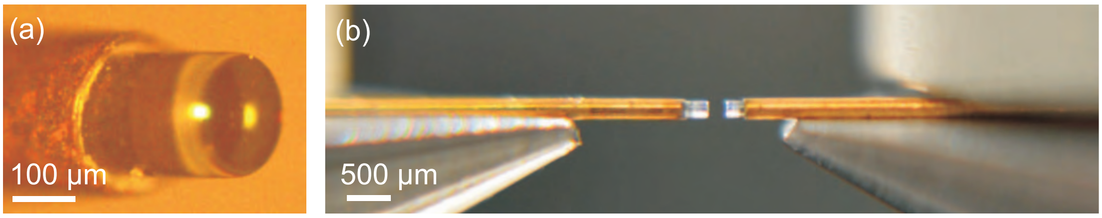

Figure 5.8: (a) Composite microscope photo of a concave fiber tip with mirror coating. (b) Photo of an FFPC. The fibers are copper-coated for ultra-high–vacuum compatibility and have a cladding diameter of 200 µm. The copper is etched back about 300 µm from the fiber facets. The glass cladding and the grey titanium layer around the cladding, which starts about 100 µm behind the facet, can be seen. The two opposing mirrors fabricated on the fiber facets form a Fabry-Perot cavity 200 µm in length. (Photographs taken by Klemens Schüppert)

signal. For aligning fiber cavities for test purposes in the laboratory, one fiber is fixed while the second fiber is mounted on a six-axis nano-positioning system[12] and positioned with respect to the first fiber. The positioning system is shown in Fig. 5.7. The cavity length is swept across a free spectral range with a piezo drive in the nano-positioning system. As light sources, we use single-mode 866 nm or 844 nm light from diode lasers[13].

In the few cases where aligning the fibers by eye to form very short cavities does not work, we coarsely position the fibers by coupling multimode 635 nm light from a fiber tester into the cavity. As the mirrors are highly transmissive at that wavelength, light is visible at the cavity output once the fibers are aligned. More specifically, the mirrors form a low-finesse etalon at this wavelength. Therefore, as the cavity length is changed continuously, maxima and minima of the transmission are visible at the cavity output. The cavity length is modulated by sweeping the voltage of a piezo integrated in the positioning stage. The transmission signal is then used to improve the fiber-to-fiber alignment. This method works well to align the fiber mirrors and to obtain a cavity signal with the 860 nm light. Fig. 5.8 shows a composite microscope picture of a coated fiber tip and a photo of an FFPC in our laboratory.

To build longer fiber cavities, the distance between the mirrors is then increased stepwise while optimizing the fiber alignment by maximizing the transmission signal. Using this technique, cavities of lengths up to 350 µm have been built. Generally, we observe that cavities of up to about 100 µm in length are robust to changes in mirror position or angle. As the fiber mirrors are separated further, however, very small changes misalign the cavity. As we use fibers with radii of curvature larger than 200 µm, (Sec. 5.2.2), this length is still far away from the edge of the cavity-stability region. Therefore, we attribute this sensitivity to the alignment to imperfect mirror shapes. A consequence of the cavity's susceptibility to small misalignments, for building long cavities, care has to be taken that the fibers are mounted very stably.

---

[12] Thorlabs Nanomax602D/M
[13] Toptica, DL Pro

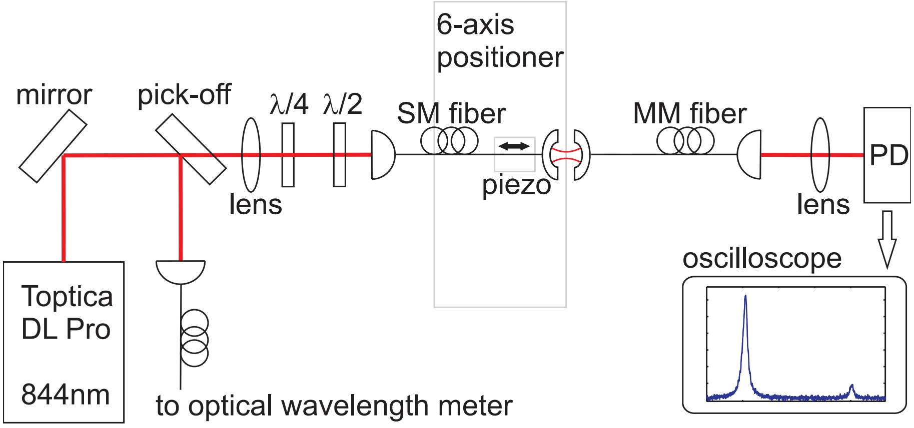

Figure 5.9: Setup to align FFPCs and measure their finesse. We use a grating-stabilized diode laser, the wavelength of which is measured with an optical wavelength meter. With a $\lambda/4$- and a $\lambda/2$-wave plate, we select the polarization of the light that is coupled into the cavity via a single-mode (SM) fiber. The cavity itself is aligned with a six-axis micropositioning system. The cavity length is tuned by a piezo actuator inside the micropositioning stage. We detect light through the cavity at the multimode (MM) fiber output with a 125 MHz photodiode (PD).

5.3.2 Measurement setup

We calculate the finesse $\mathcal{F}$ of the fiber cavities via Eq. 5.1. In order to do this, we measure the cavity's full width at half maximum $\delta\nu$ and its free spectral range ν_{FSR}. We use a diode lasers at 844 nm or at 866 nm. The laser is coupled into the single-mode fiber used as the cavity input. The cavity output light from the multimode fiber is detected with a 125 MHz photodiode. The laser wavelength is measured with an optical wavemeter[14]. A sketch of the measurement setup is shown in Fig 5.9.

Measurement of the free spectral range: The free spectral range is the spacing between two successive longitudinal modes of the cavity. To measure ν_{FSR}, we leave the cavity length fixed and adjust the wavelength of the laser by turning the grating angle while monitoring the wavemeter. When the cavity is resonant with the laser frequency, we see transmission through the cavity. We measure the wavelength separation between successive TEM$_{00}$ modes and calculate the cavity length $L = \Delta n \lambda_1 \lambda_2 / 2(\lambda_1 - \lambda_2)$ as well as $\nu_{\mathrm{FSR}} = c/2L$.

To estimate the measurement uncertainty of the free spectral range, we have to consider drifts of the fibers that change the cavity length. By comparing successive measurements, we see that short-term drifts are usually less than 5 µm. This uncertainty dominates the measurement uncertainty. In combination with our ion-trap setup, we plan to use a fiber cavity of 200 µm fiber-to-fiber distance. For this cavity, successive modes are separated by 2 nm, which corresponds to $\nu_{\mathrm{FSR}} \approx 750$ GHz.

Measurement of the cavity linewidth: The linewidth $\delta\nu$ of the cavity is determined from the full width at half maximum of the cavity transmission peak. We measure

---

[14] HighFinesse, WS7

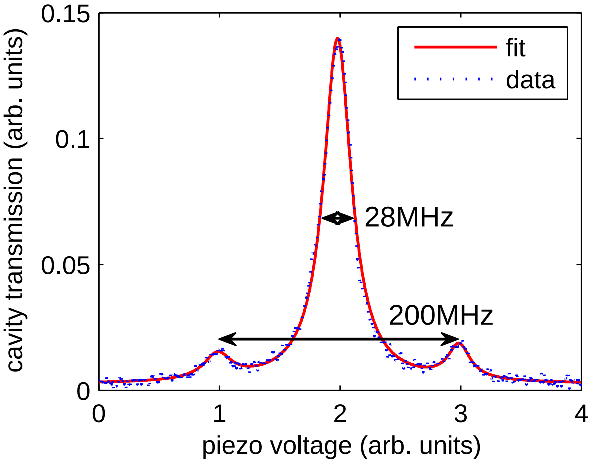

Figure 5.10: Cavity transmission peak of a test cavity using 844 nm light. 100 MHz sidebands are generated by modulating the laser current. The cavity length is modulated by scanning the voltage of the piezo stage to which one fiber is fixed. From a Lorentzian fit we determine $\delta\nu$, where the sidebands are used as a ruler to calibrate the piezo voltage axis.

it by adding frequency sidebands to the laser using a radio-frequency generator, which modulates the laser current in the 100 MHz regime. As we sweep the length of the cavity, instead of just one transmission peak, we see two additional sideband peaks; see Fig. 5.10. We fit this transmission function with Matlab using a linear combination of three Lorentzian functions (Sch12). The known sideband frequency is used as a ruler to determine the width of the central peak in units of frequency. In the example spectrum shown in Fig. 5.10, $\delta\nu = 28$ MHz. This value was measured for a cavity 50 µm in length.

Calculation of the finesse: Using the values for the free spectral range and cavity linewidth given above, the finesse is calculated to be $\mathcal{F} = \nu_{\mathrm{FSR}}/\delta\nu = 1.07 \times 10^5$ for this set of fibers.

5.3.3 Active length stabilization

In our ion-cavity system, we want the cavity length stabilized close to or on resonance with the atomic transition. However, we cannot use light at the transition frequency to stabilize the cavity length as it would interfere with our experiments. Instead, we use off-resonant light at 785 nm to stabilize the cavity to a double resonance (Rus08) of both, 785 nm light and the atomic-transition frequency. The 785 nm laser is frequency-stabilized to a temperature-controlled high-finesse cavity under vacuum. The FFPC is stabilized to this laser in transmission using the Pound-Drever-Hall technique (Dre83). A sketch of the setup is shown in Fig. 5.11. The 785 nm laser was set up by Carlos Russo to stabilize the cavity in the apparatus, which he constructed during his Ph.D. thesis work research. The laser system and subsequent changes are described in Carlos Russo's and Andreas Stute's theses (Rus08, Stu12a). We have installed a fiber into the optical path to bring the 785 nm light to our experimental table, that is to share the laser with

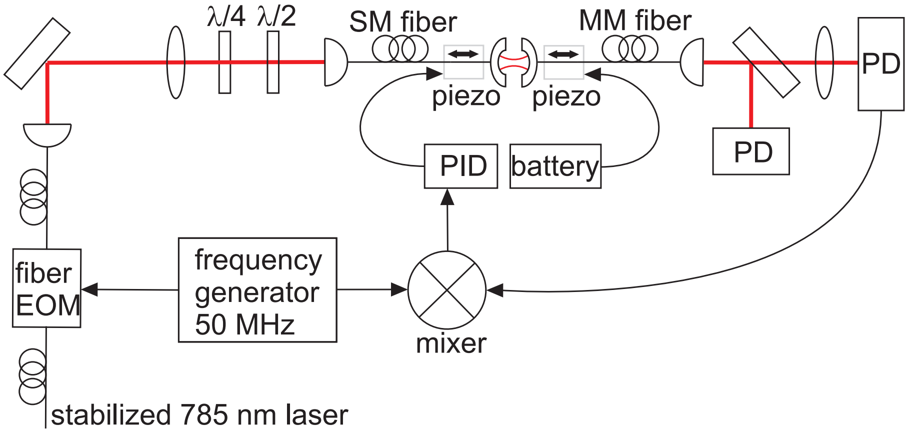

Figure 5.11: Pound-Drever-Hall lock to stabilize the FFPC length. A proportional-integral-derivative (PID) controller locks the cavity length to a 785 nm laser stabilized to a temperature-controlled high-finesse cavity under vacuum. A fiber-coupled electro-optical modulator (EOM) modulates the laser light, and the cavity transmission signal is detected on a photo diode (PD).

ongoing experiments currently led by Bernardo Casabone and Konstantin Friebe.

We modulate this laser light with a fiber-based electro-optic modulator (EOM)[15] at 50 MHz and detect the cavity-transmission signal with a photodiode (PD). This signal is mixed down at the modulation radio frequency, providing the error signal for a proportional-integral-derivative (PID) controller. The PID signal of up to 15 V drives fast sheer-mode piezos that holds both fibers. To modulate the cavity length by half a wavelength (around 430 nm), both piezos need to be driven by around 300 V. To guarantee a stable piezo voltage, such large potentials on the piezos are implemented via a stable battery circuit.

5.4 FFPC parameters and results

5.4.1 FFPC finesse as function of cavity length

We observe that the cavity finesse decreases as a function of increasing mirror separation, as was first presented in Fig. 9 of (Hun10) for short cavities. Fig. 5.12 shows this behavior for an FFPC consisting of a single-mode fiber mirror with diameter $2\rho_{\mathrm{m}} = 67$ µm and radius of curvature $R = 209$ µm and a multimode fiber mirror with $2\rho_{\mathrm{m}} = 80$ µm and $R = 355$ µm.

From ρ_{m} and R, the clipping losses due the mirror edges are calculated using Eq. 5.6 and plotted together with the data. The measured FFPC finesse starts to decrease at smaller mirror separations than Eq. 5.6 would predict. Also, the observed decrease is less steep than the simple model predicts. Because the clipping losses and thus the finesse depend exponentially on the mirror diameter and thus on L and R, the calculated finesse drops steeply as L approaches R. With this set of mirrors, this predicted drop in finesse

---

[15] Photline Technologies, NIR-MPX800-LN-05-P-P

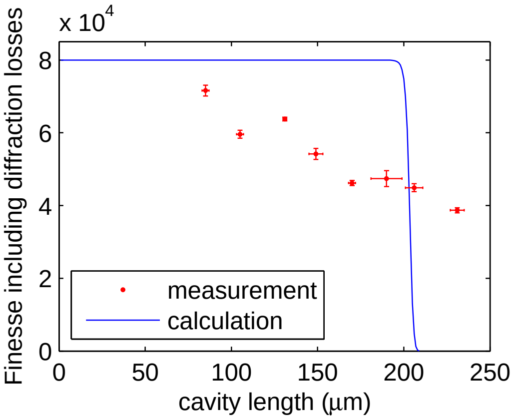

Figure 5.12: Fiber cavity finesse for 844 nm light as a function of the cavity length; compare also Fig. 9 in Ref. (Hun10). The red points are measurement values from the fiber mirrors specified in the text; the finesse decreases as the cavity length increases. The solid line shows a calculation of the finesse including scattering losses from the edge of the mirror. The disagreement of the data with the calculation suggests that other effects are responsible for the decrease in finesse.

would occur at a cavity length of about 200 µm. If clipping losses were the only reason for the finesse to vary as a function of cavity length, we would expect our data to agree with the theory plotted. The fact that it does not indicates the presence of an additional loss source that increases with cavity length.

One reason for the slow decrease in finesse might be a non-uniform thickness of the coating layers: for steep mirror surfaces, ion-beam-sputtered layers may be too thin (Roy11), shifting the coating wavelength towards wavelengths shorter than the target value. As the mode-field diameter at the mirror increases with increasing L, the mode may enter a region where the coating is no longer suited for the measurement wavelength. Ref. (Roy11) reports lower finesses for cavities using mirrors from the same coating run with smaller radii of curvature.

Note that the final data point in Fig. 5.12 corresponds to a cavity length of 231 µm. For the two radii of curvature determined from optical profilometry, this would not be a stable cavity configuration assuming that the mirrors are spherical. However, the real mirrors are not spherical and extend past the structure diameters. This geometry is difficult to model, but it is reasonable to expect stable resonators for lengths beyond the stability boundary of spherical cavities.

By increasing the mirror-structure size, it should be possible to produce longer cavities. To avoid the decrease in finesse due to clipping, we need to maximize the size of the depression created via the CO_2-laser process. Furthermore, care needs to be taken that the coating is uniform even for small radii of curvature.

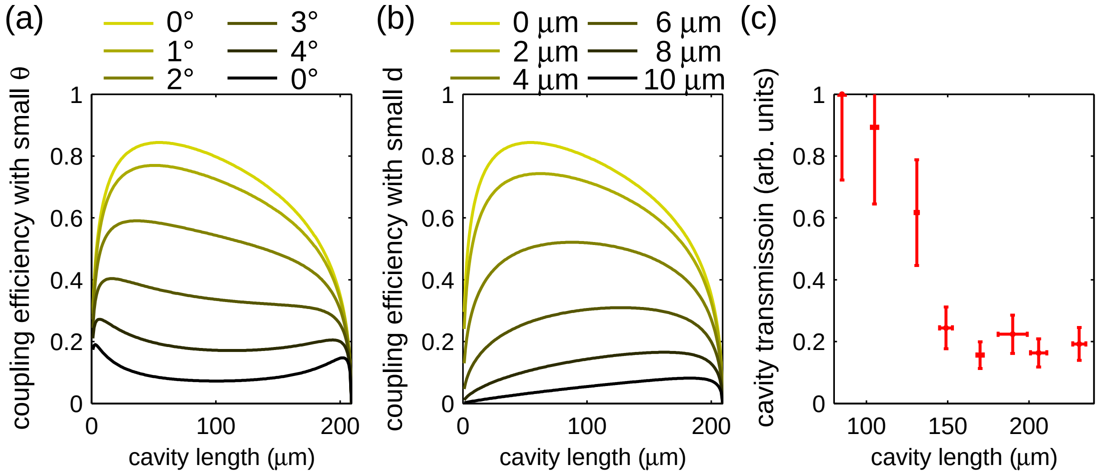

Figure 5.13: (a, b) Coupling efficiency from a single-mode fiber to the mode of a cavity as a function of the cavity length calculated from Eq. 5.7. The effects of small misalignment angles θ and displacements d are shown. The mirror radii of curvature are $R_1 = 209$ µm and $R_2 = 355$ µm. (c) Measurement of the transmission trough a fiber cavity as a function of the cavity length, referenced to the first data point.

5.4.2 Relative coupling efficiency between cavity and fiber

For free-space cavities, the incoupling mode is matched to the mode of the cavity by beam shaping and alignment. For FFPCs, in contrast, the cavity mirrors are built into the incoupling and out-coupling fibers. On one hand, this property makes the coupling robust against misalignment; on the other hand, the coupling is fully determined by mirror, fiber and cavity parameters. These differences make mode matching of fiber cavities an interesting topic to study.

The mode matching expresses the overlap between the cavity mode volume and the spatial mode of the single-mode fiber. This overlap depends on the radii of curvature of the mirrors, on the core diameter of the fiber, and on the cavity length (Sec. 5.1.2). In addition, either an offset of the mirror center from the fiber core or an angle between mirror and fiber core causes a mode mismatch which cannot be corrected. Ref. (Hun10) shows that this coupling efficiency can be as high as 85% for a short fiber cavity but calculates that it declines for longer cavities.

Fig. 5.13(a) and (b) show the calculated mode overlap ϵ for a single-mode fiber of 6 μm core diameter, considering non-zero values for θ and d as described in Sec. 5.1.2. The mirror radii are taken to be $R_1 = 209$ µm and $R_2 = 355$ µm. For $\theta = 0°$ and $d = 0$ μm, the mode matching between fiber and cavity increases steeply for short cavity lengths, has a maximum of 0.84% at length 54 μm, and decreases to half that value by 200 μm. Thus, we see that with proper alignment, it is possible to build long cavities with reasonable mode matching. As θ and d increase, the maximum value for ϵ drops, but ϵ becomes relatively insensitive to cavity length. The range of values for θ and d plotted in Fig. 5.13 reflects estimates of realistic errors in the fiber-mirror fabrication procedure. Over this range, and for all cavity lengths, these errors cause ϵ to decrease by almost an order of magnitude.

The theory predicts a steep decrease in mode matching as the cavity length approaches the smaller radius of curvature of the two mirrors, 209 μm. Therefore, when mode matching is important, cavity lengths close to the stability boundary should be avoided. As we have seen in Sec. 5.4.1, however, the stability boundary of a fiber cavity may not correspond to a calculation based on spherical mirror parameters.

Fig. 5.13(c) shows a measurement of the transmission through an FFPC. For the measurement, the same cavity as in Sec. 5.4.1 is used, with a single-mode fiber to couple light into the cavity and a multimode fiber to collect the light. Note that due to the large core diameter and acceptance angle of the multimode fiber, the collection efficiency is assumed to be unity for our cavity parameters (Hun10).

The measured coupling efficiency first decreases as a function of cavity length and then remains constant within the measurement uncertainty for cavities longer than 150 μm. Because the cavity output power was not calibrated with respect to the input power, the measured efficiencies are relative rather than absolute and cannot be compared directly with calculations. Furthermore, we cannot determine whether the decrease in transmission is due to increasing impedance mismatch or increasing mode mismatch. Therefore, an interpretation of this measurement in light of Fig. 5.13(a) and (b) is difficult.

In case optimal transmission for long fiber cavities is important, the coupling can be improved by minimizing cavity scatter and absorption losses and therefore optimize the impedance matching or by minimizing θ and d. Furthermore, modifying the single-mode fiber mode e.g. by expanding the fiber core at the fiber end would be an interesting improvement.

5.4.3 Birefringence of fiber mirrors

We have investigated the birefringent splitting of orthogonal polarization modes in FFPCs. We observe that our fiber cavities exhibit significant birefringence, whereas cavities built with the reference mirrors produced on superpolished substrates in the same ATF coating run do not exhibit measurable birefringence. Furthermore, we observed that the birefringent splitting of the fiber cavities varies as a function of the cavity alignment. In Klemens Schüppert's Master's thesis (Sch12), he presents our finding in detail together with a theoretical explanation for the observed phenomena. Here, only a brief summary of our measurements is given.

The interest to control the birefringence of the cavity mirrors has its origin in the idea of encoding quantum information in photon polarization. Several experiments then benefit from having the modes of orthogonal linear polarization degenerate in the cavity (Stu12c, Sch12). In a cavity formed from mirrors fabricated on superpolished substrates, birefringence is typically induced via uniform stress applied to the mirrors due to the mounting (Lyn03). In contrast, fiber mirrors are usually glued to a mount a few millimeters from the mirror surface, a length scale much greater than the surface diameter. Therefore, we assume that the stress is intrinsic to the coating and is created in the coating process.

To determine the magnitude of the birefringent splitting, we measure the transmission curve of a fiber cavity. With waveplates, we determine the polarization at the input of

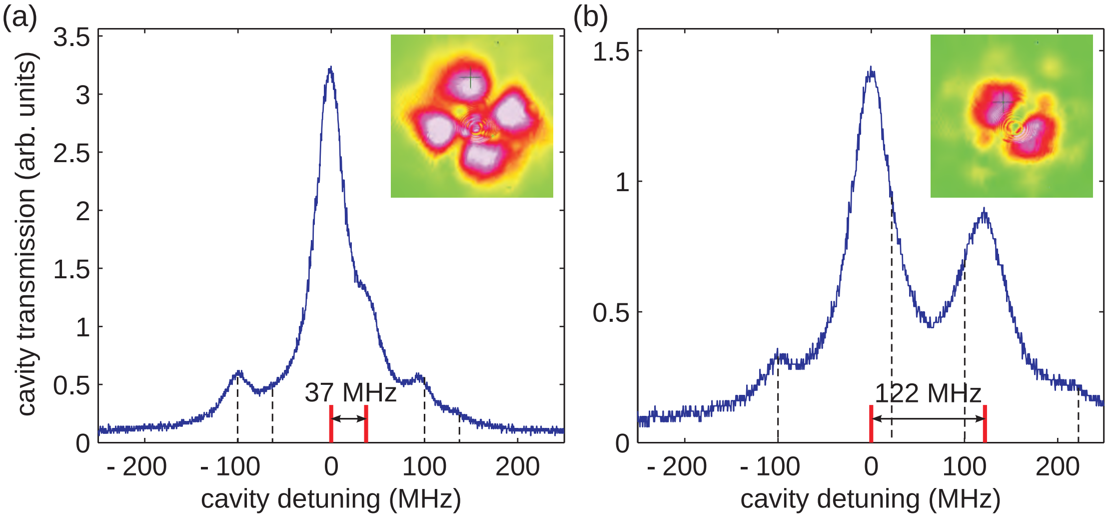

Figure 5.14: Birefringent splitting of orthogonal polarization modes inside the cavity. (a) Birefringent splitting of 37 MHz for the TEM_{11} and (b) of 122 MHz for the TEM_{01}. The dashed lines indicate 100 MHz sidebands of both modes on the laser frequency. The insets show CCD camera images of the cavity modes.

the cavity. To calibrate the frequency axis, we modulate the driving laser to produce frequency sidebands, similar to the measurement of $\delta\nu$ in Sec. 5.3.2. We measure the relative detuning between the polarization modes as a function of the cavity alignment and observe splittings that range from smaller than the FWHM ($\delta\nu \approx 30$ MHz) up to a few Gigahertz. The birefringent splitting of 200 MHz measured in Ref. (Hun10) is in agreement with these measurements. Furthermore, when aligning the cavity to support different TEM modes, we observed that these TEM modes have different birefringent splittings.

To image the TEM mode, we have modified the experimental setup, as the TEM mode of the cavity is not preserved inside the output multimode fiber. The multimode fiber was replaced by a mirror fabricated on a superpolished substrate. The TEM mode was then imaged with a camera in parallel with cavity transmission measurements of the birefringent splitting. The experimental setup is shown in Fig. 5.2 and Fig. 5.3 of Klemens Schüppert's Master's thesis (Sch12). For a test cavity, the measurement curves to determine the birefringent splitting of two different cavity modes are shown in Fig. 5.14. We measured a splitting of 37 MHz for TEM_{11} and 122 MHz for TEM_{01}, demonstrating that the birefringent splitting is dependent on the TEM mode and thus on the specific mirror region that the cavity mode samples.

We conclude that birefringence is not homogeneous over the mirror coating on the fiber. Thus, simply rotating two birefringent fiber mirrors with respect to one another will not necessarily eliminate cavity birefringence as we had initially hypothesized. However, by careful selection of fibers and proper alignment, we have built cavities which satisfy a target birefringent splitting, in our case, degenerate polarization modes.

5.4.4 Surface losses of fiber mirrors

The losses of highly reflective mirror coatings depend critically on the surface quality of the mirror substrate: surface roughness of the substrate material results in scattering losses of the mirror. In order to reduce the scattering losses to ~ 1 ppm at near-infrared wavelengths, the surface roughness needs to be less than 1 Å rms (Hun10). Mirror substrates with surface roughness less than 1 Å rms are referred to as superpolished. With superpolished substrates, we assume that all scatter and absorption losses come from point defects in the coating.

As CO_2-laser ablation is a novel technique for producing curved mirror substrates, it is of great interest to determine the quality of the shaped surfaces and the induced scattering losses. Fiber surface roughness σ has previously been measured with an atomic force microscope and linked to the scattering losses S via $S \approx (4\pi\sigma/\lambda)^2$, where $\sigma = (0.2 \pm 0.1)$ nm, corresponding to $S = (10 \pm 10)$ ppm for near-infrared light at $\lambda = 780$ nm (Hun10).

In contrast, we compared fiber mirrors with reference mirrors fabricated on superpolished substrates. We measured reference-mirror cavities to have a finesse of $(1.10 \pm 0.04) \times 10^5$, in comparison to a finesse of $(1.14 \pm 0.05) \times 10^5$ for the fiber-mirror cavities. The total mirror losses $\mathcal{L}_{\text{tot}} = \mathcal{T} + \mathcal{L}$, the sum of transmission $\mathcal{T}$ and losses $\mathcal{L}$, were calculated from the finesse via $\mathcal{L}_{\text{tot}} = 2\pi/\mathcal{F}$. The reference substrates and the fiber mirrors thus have identical total losses of $\mathcal{L}_{\text{tot}} = (28 \pm 1)$ ppm. Therefore, fiber-surface roughness is not associated with any additional scattering losses within a 1 ppm measurement error. This result suggests that it may be possible to construct fiber cavities with finesses as high as those achieved with state-of-the-art superpolished mirrors (Rem92). The measurement is the first direct comparison of the losses of fiber-mirror coatings (including losses induced by surface roughness) with losses of identical coatings fabricated on fused silica substrates.

5.5 Possible improvements for FFPCs

Fiber-based Fabry-Perot resonators are powerful tools for quantum electrodynamics experiments. However, the production technology is relatively young and still allows for further development. During my work with fiber cavities, I have learned which of their properties need to be improved and, moreover, can be improved further. In discussions with other researchers working with cavities, ideas have been developed of how it might be possible to change the fabrication processes for FFPCs. This section lists the most important points:

Increasing the fiber-mirror finesse

Annealing fibers: As described in Chapter 6, we would like to anneal our fiber mirrors in order to further reduce the coating losses. Despite attempts to anneal fiber mirrors in a clean environment, the mirrors always became dirty during the annealing process, and we were never able to build an FFPC with annealed mirrors. Most likely, the copper coating oxidized and contaminated the mirror surface in a way that could not be repaired by cleaning. We expect that gold could be a better coating material, due to its high chemical stability even under extreme temperatures. For a new production run of fiber mirrors, purchasing gold-coated fibers or coating our current fibers with an additional layer of gold via electroplating could make annealing possible.

Mirror coating with lower transmission: With the knowledge we have gained about the high fiber-surface quality, we would now produce fiber coatings with smaller design transmissions. Furthermore, having coatings with different transmission $\mathcal{T}_1$ and $\mathcal{T}_2$ fabricated on the incoupling and out-coupling fibers, would allow us to build asymmetric cavities, defining cavity input and output fibers. A cavity in which one mirror has a higher transmission as the other mirror almost all photons leave the cavity through the more transmissive mirror, thus optimizing the collection efficiency of the cavity photons.

Improving the mirror shape

Larger mirror diameters: A severe limitation of our fiber mirrors is their small diameter. We would like to use the full fiber diameter (125 µm for standard fibers or 200 µm for our custom fibers) as the mirror diameter. Therefore, one would need to improve the laser-ablation process, use another technology to produce concave structures on fiber tips, or even combine various technologies. A promising way to improve the ablation process is pursued by the late Wolfgang Lange's research group now led by Matthias Keller at the University of Sussex. In their setup, multiple pulses (several hundreds) are used to produce very large structures on the fiber tips. A second technology to shape glass surfaces is ion-beam milling. Here, a focussed beam of ions sputters away small amounts of material from a surface in a controlled way. To write large and deep structures as required for large mirror diameters, however, the precision of the process decreases while the roughness of the produced surface increases[16]. This problem could maybe be overcome by combining the ion-beam milling and the CO_2-laser ablation technologies.

Spherical mirrors: A drawback of the laser-ablation process is that it produces depressions of Gaussian shape by mapping the Gaussian beam profile onto the fiber surface. Ideal cavity mirrors have spherical surfaces. Producing shapes that are more similar to perfect spheres could be achieved by, e.g., changing the beam shape of the CO_2 laser or by a series of Gaussian-shaped pulses with beam centers at different positions.

Minimizing ellipticity: The laser-ablation process in Reichel's laboratory produces elliptical structures on the fibers. Possible reasons for this effect include abberations of the laser beam or gravity pulling the melted glass downwards. The second effect could be avoided by mounting the fiber vertically for the ablation process. In Keller's research group, mentioned above, they have found a method to eliminate ellipticity completely by rotating the fiber during the sequence of multiple CO_2-laser pulses[17].

Optimal coupling efficiency: The coupling from the single-mode–fiber mode to the cavity mode decreases if the mirror center is offset from the fiber core or if the mirror plane has an angle other than 90° with respect to the fiber axis. Such an additional angle could be avoided by measuring the cleave angle before the ablation process and only selecting fibers with 90° angles. To center the mirror structure optimally on the fiber, one could integrate a profilometer into the microscope of the ablation setup. The

---

[16] Roland Albrecht, Universität des Saarlandes, personal communication

[17] Hiroki Takahashi, University of Sussex, personal communication

microscope image could then be compared with the profilometer image while the fiber is being produced, and errors could be corrected immediately.

Other improvements

Mode matching of the fiber mode: The fiber-cavity coupling efficiency is determined by the overlap of the fiber mode and the cavity mode; see Sec. 5.1.2. The cavity mode is determined by the radii of curvature of the mirrors and the cavity length. Therefore, to improve the mode overlap, the fiber mode must be adjusted. By splicing a lensing section, e.g., a short piece of graded index multimode fiber, to the end of the single-mode fiber, the cavity mode is focussed as it exits the fiber, which would improve the mode overlap.

Single-mode cavities: Currently, we build FFPCs with single-mode fibers as the cavity input and multimode fibers as the cavity output. This design is used successfully in neutral atom experiments (Col07). The multimode fiber, however, removes information about the spatial mode and the polarization mode of the cavity. For experiments which require this information to be maintained, one would thus have to use single-mode fibers as cavity output (Mul10).

Stable mounting: We have learned that FFPCs longer than 150 µm are very sensitive to small misalignments of the fiber mirrors. To maintain alignment of a 200 µm long cavity in vacuum, we currently use an in-vacuum positioning system and position the mirrors precisely with respect to one another (Sec. 7.2.2). However, it is of interest to develop fiber mounts which are robust enough to maintain the cavity alignment passively.

5.5.1 A new CO_2-laser ablation setup

In Reichel's laboratories at the ENS, currently, an improved CO_2-laser ablation setup is under construction. The setup will be designed to use multiple ablation pulses to produce more symmetric shapes, similar to the setup in Keller's research group. Additionally, this procedure reduces the negative effects of melting the glass thus increasing the mirror surfaces. The fibers will sit on micro-positioning stages with piezo drives that translate the fibers in the plane orthogonal to the laser beam. A rotational piezo stage provides the capability to rotate the fiber. Furthermore, an optical profilometer will be integrated directly into the setup and will allow an in-situ analysis of the fiber surface. Thus, ellipticity and errors in the centering of the fiber could be corrected during the process.

Keller's group is able to produce fibers with radii of curvature up to 500 µm and mirror diameters that use almost the full surface of the fiber tip. Using one curved and one flat fiber end, the group was able to build cavities of up to 500 µm in length[18]. With the new technologies integrated in the ablation setup at the ENS, we expect to produce fiber mirrors with surfaces close to a spherical shape and thus be able to construct cavities close to the concentric regime. In this regime, the cavity waist becomes small, providing a high coupling rate. We expect to be able to produce fibers with considerably larger structure diameters on the order of the fiber diameter, which would allow us to build long cavities. Furthermore, due to the more symmetric structures and larger structure

---

[18] Hiroki Takahashi, University of Sussex, personal communication

diameters, we expect that the finesse would not decrease with the cavity length, as it is the case for the current fibers.

These improvements on the fiber Fabry-Perot resonators promise cavities which are more robust against misalignment and thus allow easier integration of the fibers into the ion-trap setup. Furthermore, optimized mirror shapes will allow us to construct cavities close to the concentric regime and therefore help us reach high coupling rates between cavity photons and ions. Asymmetric coatings and coatings of lower transmission are a first steps toward small cavity decay rates. Annealing, which is another important step to minimize coating losses, is discussed in the following section.

6 Annealing mirrors

Ultralow-loss mirrors at optical wavelengths are routinely employed in quantum-optics experiments. Using ion-beam sputtering, mirrors with transmission plus absorption and scatter losses as low as 1.6 ppm in the near infrared are fabricated (Rem92). In order to achieve such low losses in dielectric mirror coatings, it is a standard procedure to anneal the coatings after fabrication. Annealing leads to homogenization of the oxide layers and improves the stoichiometry of non-perfect oxides (Ata95), reducing coating losses typically by 10 ppm. This procedure is thus a key step in the process of manufacturing ultra-low-loss mirrors.

The recent development of fiber cavities raises the question of whether annealing fiber mirrors is possible. Since the surface roughness of CO_2-laser–ablated fiber tips is comparable to that of superpolished mirror substrates (Sec. 5.4.4), the finesse of fiber cavities can in principle reach the record values achieved with mirrors fabricated on substrates. To reach this high finesse, however, annealing would be essential.

In the following, annealing experiments performed with fibers and substrate mirrors are described. Andrew McClung was involved in the annealing tests, and Ramin Lalezari from ATF and Tracy Northup contributed to the analysis and interpretation of the experimental results. To perform X-ray photoelectron spectroscopy measurements, I collaborated with Frederik Klauser from the Institute of Physical Chemistry of the University of Innsbruck.

My initial efforts to anneal fiber mirrors have been unsuccessful. We attributed some of the difficulties to possible chemical reactions of the fiber-coating material with oxygen in the air. For this reason, we were interested in exploring annealing under vacuum. Furthermore, knowledge about the effects of baking mirrors under vacuum is essential for all experiments in which low-loss mirrors are placed under ultra-high vacuum (UHV), which requires a vacuum bake. The typical temperatures for a vacuum bake are lower than annealing temperatures, but the same chemical processes are at work. In various experiments, degradation of cavity mirrors under vacuum has been observed (Ref. (Cet13, Ste12) and references therein), but evidence of changes in mirrors under vacuum has been mostly anecdotal. Because the cavities are part of complex experimental systems, in which repeated bake-outs are impractical, a careful study of these effects has not yet been undertaken.

In order to study annealing and baking under vacuum systematically, we used reference mirrors which had been produced in the same coating run as the fiber mirrors (Sec. 5.2.3). These reference mirrors were fabricated on fused-silica substrates of half-inch and 7.75 mm diameters. They were coated with a highly reflective coating comprised of 37 alternating layers of Ta_2O_5 and SiO_2, where the inner- and outermost layers are Ta_2O_5. The layers were deposited using ion-beam sputtering, and each layer has a $\lambda/4$ thickness for peak reflectivity at $\lambda = 860$ nm. Using these mirrors, we systemati-

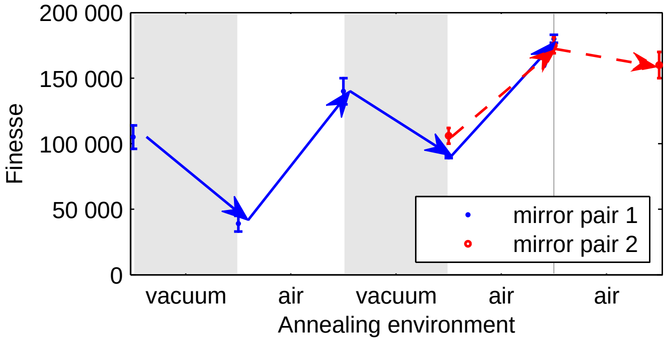

Figure 6.1: Finesse after annealing at 450°C under alternating air and vacuum environments. Annealing under vacuum shows repeatable losses in cavity finesse, and annealing under air repeatable gains.

cally measured effects from annealing under air and vacuum in a clean and controlled environment.

In this section, annealing refers to a 90 minute ramp from room temperature to 450°C, a 90 minute bake at 450°C, and a 90 minute ramp down to room temperature. Vacuum annealing consisted of placing the mirrors in a clean stainless-steel chamber, which was then pumped to pressures lower than 10^{-5} mbar by a turbo pump, after which the temperature ramp was started. For annealing under air, the mirrors were placed inside clean glass Petri dishes. Care was taken that the mirrors were properly cleaned before any finesse measurement (Nor08).

6.1 Repeated annealing under vacuum and under air

With a first pair of coated mirrors, a cavity with a finesse of $(1.05 \pm 0.09) \times 10^5$ was constructed prior to annealing. After an initial test in which the mirror pair was annealed under vacuum, the finesse had degraded to $(3.9 \pm 0.6) \times 10^4$. To investigate this unexpected result, a series of measurements was conducted, in which the annealing environment was alternated between annealing under vacuum and air. Annealing these mirrors under air resulted in a recovery of the finesse, that is, a decrease of the losses that had been induced by vacuum annealing. In fact, the new finesse of $(1.4 \pm 0.1) \times 10^5$ was higher than the initial value, indicating that annealing had removed intrinsic coating losses as expected. Two subsequent measurements showed that the losses when annealing under vacuum and gains when annealing under air are repeatable, and the maximum finesse for this pair of mirrors is $(1.80 \pm 0.03) \times 10^5$; these data are summarized in Fig. 6.1.

With a second pair of reference mirrors, the initial finesse of the first pair was reproduced: $(1.06 \pm 0.06) \times 10^5$. Annealing directly under air as the only step yielded a finesse of $(1.75 \pm 0.06) \times 10^5$, implying that the maximum finesse of this coating is independent of previous annealing cycles. Repeated annealing under air established the maximum finesse for this pair of mirrors. This finesse corresponds to total losses $\mathcal{L}_{\text{tot}}$

of (17 ± 1) ppm. We attribute 2ppm (Rem92) to scattering and absorption losses and (15 ± 1) ppm to transmission, consistent with the target transmission of the coating run.

Our finding that the change in finesse depends on the annealing environment suggests that annealing affects the chemical composition of the mirror coating. With the help of Ramin Lalezari, we hypothesized that during a vacuum bake, oxygen escapes from the outermost Ta_2O_5 layer, which leads to defects in the coating. Subsequent annealing under air gives the surface the possibility to regain the oxygen, thus removing these defects of the chemical structure. In order to test this theory of oxygen depletion, we conducted a series of X-ray photoelectron spectroscopy measurements in the chemistry department of University of Innsbruck.

6.2 X-Ray photoelectron spectroscopy measurements

X-ray photoelectron spectroscopy (XPS) is used to quantitatively determine the chemical composition of the Ta_2O_5 layer on the surface of the mirror coatings. Together with Frederik Klauser, we acquired the XPS data with a Thermo Multilab 2000 utilizing monochromatic Al Kα radiation at 1486.6 eV. The atomic composition of the samples was obtained from XPS survey scans taken with an overall resolution of 2.0 eV. The oxygen and tantalum content were determined from the O (1s) and the Ta (4d5) and Ta (4d3) lines, respectively, measured with a higher resolution of 0.1 eV. Measured intensity ratios were converted into atomic percentages using theoretical photo-ionization cross-sections of Scofield (Sco76), also taking into account the energy-dependent transmission of the electron-energy analyzer (Kla10).

6.2.1 XPS measurements of mirrors annealed under air and under vacuum

We acquire XPS spectra from two mirrors and compare their chemical composition. Prior to the measurement, one mirror was annealed in air, while the other was annealed in vacuum. To calculate the amount of oxygen and tantalum from the XPS spectra, we subtract the background and integrate over the O (1s) and Ta (4d5) and Ta (4d3) photoelectron lines. When weighted by the Scofield sensitivity factors, which represent the emission probability of an electron, these integrals give the relative proportions of the elements in the material. The sensitivity factor is 15.64 for the Ta (4d5) and Ta (4d3) line and 2.93 for the O (1s) line (Sco76).

Using this method, we compare the chemical compositions of the two mirrors. The oxygen concentration of the mirror annealed under vacuum is $(0.9 \pm 0.7)\%$ lower than the oxygen concentration of the mirror annealed under air. This difference would constitute a loss of every 90th oxygen atom from the surface of the mirror annealed under vacuum. The large error bars are due to the relative uncertainty of 0.5% between measurements on the same apparatus. To resolve the effect more clearly, we conducted a second experiment based on the measurement of a single mirror over time.

6.2.2 Continuous XPS measurement during vacuum annealing

To observe the effect of oxygen loss from the surface directly, we perform real-time XPS measurements during the process of annealing in vacuum on a mirror that has

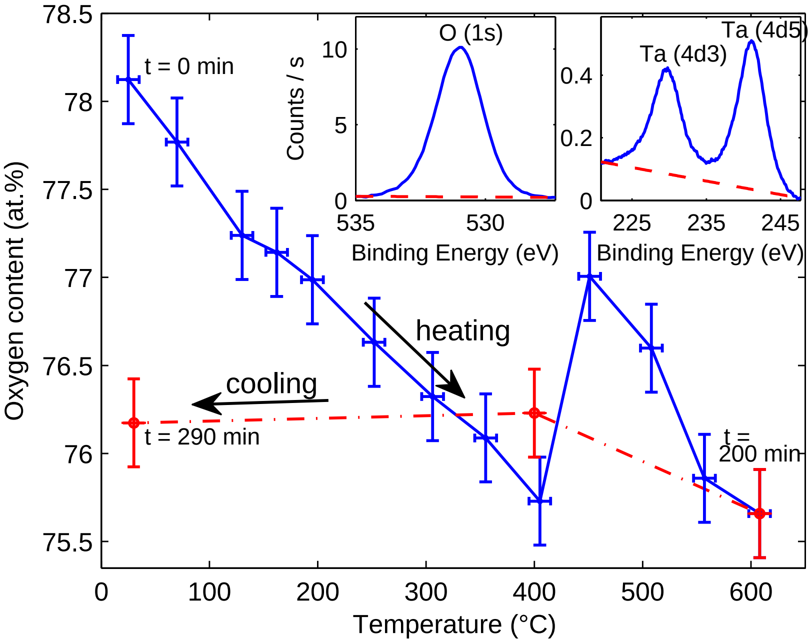

Figure 6.2: Oxygen content in the Ta_2O_5 layer on the mirror surface. The temperature of the mirror coating is increased stepwise and XPS measurements are taken at each temperature. The mirror has been annealed in air before the measurement. The solid line is taken during the heating process, the dash-dotted line during the cool-down of the substrate. The uncertainty of the temperature measurement is 20°C. The relative uncertainty of the oxygen content is 0.5%. The insets show sample XPS spectra of the O (1s) and the Ta (4d5) and Ta (4d3) lines (solid), including the background (dashed), at the starting temperature.

previously been annealed in air. The mirror is placed inside the XPS vacuum chamber and a reference XPS measurement is taken. Between subsequent XPS measurements, the mirror temperature is increased stepwise up to 608°C over 200 minutes. This procedure gives an exact chemical analysis of the mirror surface at each step of the annealing process. Integrating the area under the oxygen and tantalum peaks, we calculate the oxygen content in the surface of the mirror. The insets of Fig. 6.2 show the O (1s) and the Ta (4d5) and Ta (4d3) lines of one of the XPS spectra which we use for this analysis. The temperature of the mirror in this measurement is measured with a pyrometer (IMPAC) with a measurement uncertainty of 20°C.

Figure 6.2 shows the results of these measurements, in which the oxygen content decreases as the temperature increases. The atomic percentage of oxygen of the mirror before annealing is 78.2%; at 405°C it drops to 75.7%. The oxygen content briefly recovers between 450°C and 550°C, suggesting a phase transition (Ban94) or outgassing of oxygen. At 608°C, the oxygen content reaches its lowest point of 75.7%. The mirror cool-down lasts 90 minutes, during which the oxygen content neither decreases nor increases significantly. We note that the absolute uncertainty of the measurement is around 10%. The entire annealing process results in a (2.5 ± 0.7)% drop in oxygen content, supporting the hypothesis of oxygen depletion from the Ta_2O_5 layer.

The discrepancy between this result and our earlier measurement of Sec. 6.2.1 might be due to oxygen reuptake when the vacuum-baked mirror was in air before the XPS measurement. Both measurements show that we can attribute the lower finesse of the vacuum-annealed mirrors to the loss of oxygen of the Ta_2O_5-layer on the mirror surface.

6.3 Baking under vacuum

Up to now, only measurements of mirror annealing at temperatures of 450°C and higher have been presented. The depletion of oxygen observed at these temperatures suggests that this effect also takes place — in a moderate form — when baking mirrors at standard temperatures for a vacuum bake-out, typically 200°C to 300°C. The XPS measurement of Sec. 6.2.2 shows a linear decrease of oxygen when heating the mirror from room temperature up to 405°C in vacuum. At a temperature of 160°C one percent of the oxygen is already lost from the surface, and at 300°C 1.8% of the oxygen are lost.

We expect that if we bake mirrors under vacuum conditions at different temperatures, one would find decreasing mirror finesses as the temperature of the bake increases. This measurement would presumably show the same temperature dependence of oxygen depletion following a vacuum bake as the XPS measurements. We can calculate the mirror losses by linearly extrapolating the two vacuum-annealing measurements from Fig. 6.1 to lower temperatures. The first annealing under vacuum was performed with unannealed mirrors, while the second time, these mirrors had been pre-annealed under air. We observe a difference in losses from the unannealed mirrors and the annealed mirrors. According to these measurements, we would expect 15 ppm and 32 ppm of additional losses at baking temperatures of 150°C and 300°C for the unannealed mirrors. The annealed mirrors would only gain 4 ppm and 8 ppm of additional losses at these baking temperatures.

An annealed test mirror, baked under vacuum conditions at 300°C, showed a decrease of the finesse from 1.9×10^5 to 4×10^4 after baking. This decrease in finesse corresponds to 62 ppm losses due to baking and would extrapolate to 28 ppm losses for baking at 150°C. However, this mirror never recovered from the vacuum bake when subsequently annealed under air. The facts that the losses of this mirror increased by such a high value and that we were not able to repair the mirror with air bakes suggest that the mirror was damaged or underwent a phase transition in the baking process.

Due to the lack of more mirrors, the study could not be continued. However, both, the possibility of phase transitions and changes in finesse during vacuum bakes at moderate temperatures should be studied more carefully. To accumulate data for such measurements, one would need a larger set of coated mirrors and bake several mirrors under the same conditions to show reliable results.

6.4 Discussion

Annealing under vacuum decreases the mirror finesse rather than increasing it. As a consequence, fiber mirrors should not be annealed under vacuum.

Tests of annealing fiber mirrors under air have not been successful so far. Even when a clean annealing environment is established, the fiber mirrors seem to get dirty after baking in air and cannot be cleaned successfully. We suspect that contamination from the copper coating of the fiber damages the mirror coating. A way to remove this source of contamination is the use of chemically more inert fiber coating materials such as gold.

Furthermore, we expect the mirror losses to increase under a vacuum bake even at moderate temperatures. The XPS measurements of Sec. 6.2.2 show that the oxygen decreases linearly with increasing baking temperature, and thus the amount of defects in the mirror increases. Vacuum baking should therefore be done at the lowest possible temperatures, although baking at higher temperatures under oxygen atmosphere might be an alternative to a vacuum bake as it would not degrade the mirrors but still reduce the partial pressure of other gasses.

7 Experimental setup

This chapter describes in detail the experimental system of an FFPC integrated with an ion trap. In this system, the fibers are mounted on ultra-high–vacuum compatible positioners, enabling in-vacuum cavity alignment. In addition, these positioners allow us to pull back the fibers from the trap center, so that the ion trap can be tested without the ion seeing the influence of the fibers on the trapping potential. The ion trap is a modified version of the linear Paul trap presented in Refs. (Gul03, Rie05). It is currently the trap with the smallest ion-electrode separation operated in the Innsbruck Quantum Optics and Spectroscopy group.

The final decision to use a linear trap for our setup was reached in discussions with Tracy Northup, Rainer Blatt, and Andreas Stute. Most of the trap components and a first set of ceramic mounts were manufactured in the mechanical workshop of our institute by Andreas Reinalter. He also collaborated with me in designing the trap. Stefan Haslwanter from the mechanical workshop of the Institute for Quantum Optics and Quantum Information helped with small changes of the blade electrodes. Andrew McClung and Tracy Northup helped in assembling the vacuum apparatus and with testing the ion trap. Klemens Schüppert and I integrated the fiber cavity into the vacuum apparatus and tested the ion trap performance in presence of the dielectric fibers.

7.1 Miniaturized linear Paul trap

In designing the experiment, the trapping potentials under the influence of dielectric fibers for four different trap geometries were simulated (Chap. 4). A linear trap benefits from a deep trapping potential and an open geometry which allows for the integration of an FFPC. Here, the technical features of the ion trap used in the experimental setup, its assembly, and its advantages and disadvantages are described.

7.1.1 Ion trap dimensions

The design of the linear Paul trap is shown in Fig. 7.1. Four blade-shaped electrodes operated with radio-frequency (RF) and ground (GND) voltages confine the ion in the radial plane, and two tip electrodes with positive voltage add confinement along the trap axis orthogonal to this plane; compare Sec.4.1 and Sec. 4.4.

The trap creates a deep potential inherent to three-dimensional traps (Sec. 4.4), but in contrast to other traps in use in our research group (Gul03, Rie05), it is miniaturized in order to make its dimensions comparable to those of the FFPC. The distance between opposing blade tips on the diagonal is 340 µm, which means that the minimum ion-electrode distance is only 170 µm; in contrast, in the design of (Rie05), the ion-electrode distance is 800 µm. The distance along the trap axis between the two tip electrodes is

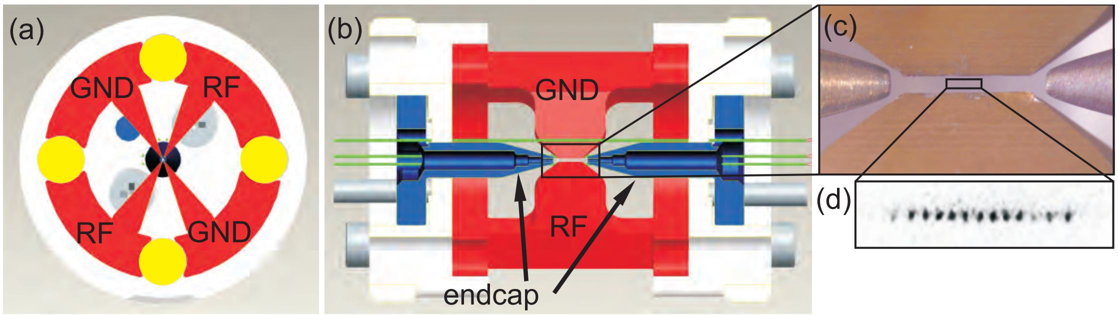

Figure 7.1: (a),(b) Miniaturized ion-trap design. Red: two radio-frequency (RF) and two ground (GND) blades of the linear Paul trap; the distance between two opposing blades on the diagonal is 340 µm. Blue: positively charged tip electrodes, 2.8 mm apart. Green: four rods parallel to the trap axis are used as compensation electrodes, 1.7 mm from the trap center. White: ceramic (MACOR) mount. Yellow: holes in which alignment rods are inserted during assembly. The plane for optical access, including laser cooling, manipulation, and fluorescence detection, is the vertical axis through the trap center in (a). 300 µm wide holes in the endcaps provide additional optical access in this plane. (c) Photo of the ion-trap center. (d) CCD camera image of a linear string of ions confined in the trap.

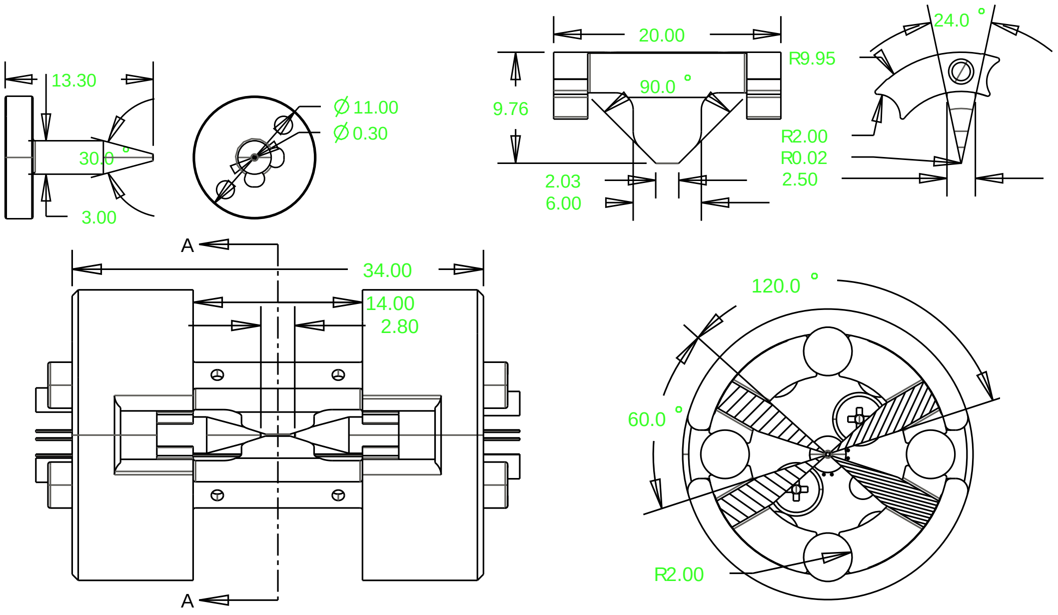

Figure 7.2: Relevant dimensions of the ion trap. Length values are given in millimeters. The endcap electrode, the trap blade, the fully assembled trap, and a cut through plane A of the assembled trap are shown. The blade separation between upper and lower neighboring blades is 150 µm, and between left and right neighboring blades it is 290 µm.

2.8 mm, about half the length of previous designs. These axial electrodes have 300 µm diameter holes for optical access along the trap axis, similar to the trap design in (Zäh12). All relevant trap dimensions are specified in Fig. 7.2.

Another significant change with respect to previous designs is that the angle between neighboring blade electrodes is not 90°. In order to provide space for the fibers while maintaining a small separation between them, the two angles between the blades shielding the fibers are increased to 120°. As a result, the other two angles between neighboring blade pairs are 60°. This change does not alter the trap depth significantly (Sec. 4.4.3). The trap has four additional rod-like electrodes, parallel to the trap axis, 1.7 mm away from trap center, and 200 µm in diameter. These electrodes are standard components of the Paul traps in our research group (Gul03, Rie05) and allow for compensation of ions' micromotion. This motion is due to imperfections in the geometry of the assembled trap and charges on surfaces. The imperfections and the charges cause a displacement of the center of the RF potential with respect to the DC potential, resulting in unwanted heating of the ion. We apply small DC voltages to the compensation electrodes to shift the center of the DC potential to the center of the RF potential. The rods are supplied with independent voltages, enabling compensation for charges on the dielectric fibers.

7.1.2 Fabrication and assembly

Such a small trap must be machined and assembled to tolerances within a few micrometers to guarantee stable ion trapping. The stainless-steel blade electrodes are aligned and fixed in place by two precision-machined glass-ceramic (MACOR) holders, shown together with all trap components in Fig. 7.3. The fabrication tolerance for the ceramic mounts is less than 50 µm, close to the limit of standard machining tools. The dimensions of the holders are measured after machining, and the blade electrodes are subsequently electron-discharge machined to fit the holders exactly. After production, all parts are carefully cleaned for ultra-high vacuum use and handled only with clean gloves during assembly.

To assemble the trap, first the endcaps are fixed to the ceramic mounts. Precision alignment of the blades with respect to the ceramic mounts and to one another is done with alignment rods, which are later removed. These rods also align the trap with respect to the whole mount. Next, the compensation electrodes are slid through the 200 µm thin holes of the ceramic mounts. The compensation electrodes are stainless steel rods of 200 µm diameter[1]. One end of the thin rods has a thickening to prevent the electrode to slide trough the hole in the trap mount. The electrodes are then tensioned via the compensation-electrode mount. A nut presses the thin rod against this mount; see Fig. 7.3(c). Care was taken to ensure that all the compensation electrodes are under tension, so that they do not make contact with one of the blades or the endcap electrodes. The fully assembled trap is shown in Fig. 7.3(b). After assembling the trap, we measure its dimensions under a microscope; see photos in Fig. 7.4. We find that the inaccuracy in blade-to-blade separation is less than 30 µm.

The holes in the ceramic mounts for the alignment rods and the trap blades are machined with almost no play in order to achieve our target precision. As a result, the trap mounting process is challenging because the rods get stuck easily and are difficult

---

[1] Polyfil AG

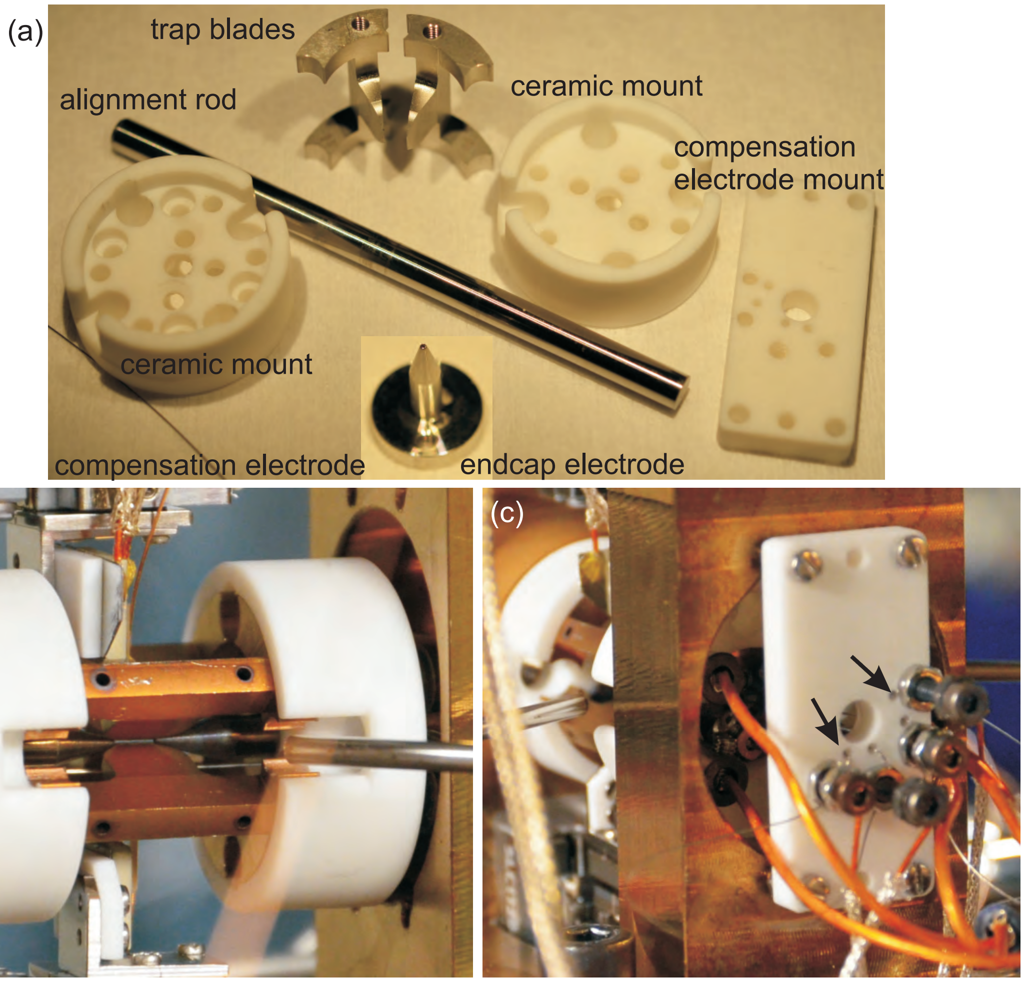

Figure 7.3: (a) Photo of the individual trap components, including trap blades, endcap and compensation electrodes, alignment rod, ceramic mount and compensation-electrode mount. (b) Photo of the assembled trap with the alignment rods already removed. (c) Photo of the compensation electrode mount. The four, thin electrodes (two of them are indicated with an arrows) are pressed against the ceramic mount with a nut and connectorized individually.

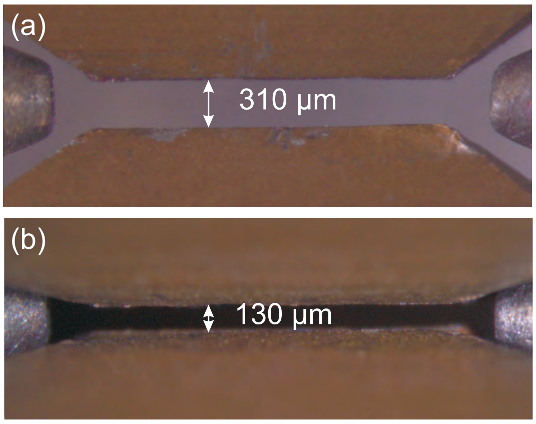

Figure 7.4: Microscope pictures of the assembled trap. (a) Photograph taken from the side where the fibers are mounted later. (b) Plane of laser access. We measure the blade distance and determine the accuracy of the trap alignment. We find that the blade distance has an uncertainty of less than 30 µm.

to remove. Furthermore, the ceramic mounts are brittle and break when too much force is applied. One solution to this problem was using clean methanol as a lubricant to facilitate the removal of the alignment rods. However, several ceramic mounts for our trap broke, and new ones had to be ordered. These were machined externally using the drawings from our workshop[2]. We were pleasantly surprised by the precision of the parts that the company delivered.

The trap is mounted on a CF150 flange; this is the top flange of the vacuum chamber. The flange also holds all electrical feedthroughs and the fiber feedthroughs. The connections between the trap electrodes and the electrical feedthroughs are made via vacuum-compatible BNC cables[3].

7.2 Integration of the FFPC

Under vacuum, the fiber cavity needs to be aligned with respect to the ion trap such that the potential minimum in which the ions are trapped overlaps with the waist of the cavity mode. Furthermore, the fiber mirrors need to be aligned precisely to form a Fabry-Perot resonator. Also, the length of the cavity has to be actively stabilized. Here, I describe the mount of the fibers under vacuum, which fulfills all these requirements.

7.2.1 First, unsuccessful version of the cavity mount

In the FFPC experiment of (Col07), the alignment of the fiber mirrors was done before the system was placed under ultra-high vacuum: one fiber was glued on a cavity mount carefully positioned with respect to an atom chip, and the second fiber was then aligned to form a cavity with the first fiber and attached to the chip with ultra-high vacuum

---

[2] WZW Optic AG

[3] LewVac LLP and MDC Vacuum Limited

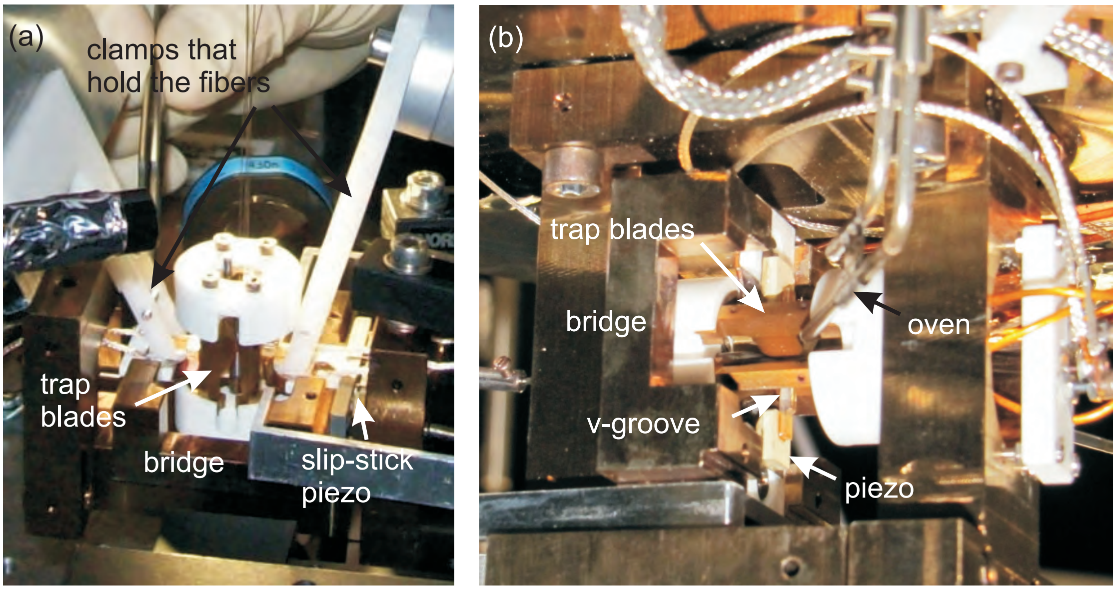

Figure 7.5: (a) Setup to align the fibers to form an FFPC around the ion trap. Both fibers are held with clamps and are moveable with respect to each other and the trap. The fibers are glued onto a stainless-steel bridge. (b) Photo of the glued fibers and the trap setup. Each fiber sits on a v-groove and a shear-mode piezo. Unfortunately, the mount was not stable enough to maintain the cavity alignment.

(UHV) epoxy[4]. While the glue cured, the fiber was continuously aligned by optimizing the cavity transmission signal.

We initially decided to use the same method in order to implement a fiber cavity into the ion trap. However, for neutral atoms on an atom chip, the trap minimum can be shifted along all axes via magnetic fields and trap currents. Using this method, the atoms are positioned in a cavity antinode. In contrast for ions, the ion position can only be varied along one axis, the trap axis. This is done via changing the endcap electrode voltages. For the other two axes, the radial trap axes, one needs to make sure that the FFPC can be positioned with respect to the ion instead. One of these axes is along the cavity axis. Along this axis, the position of the antinode of the standing wave can be aligned with the shear-mode piezos that stabilize the cavity length. In the second radial axis, however, the cavity needs an additional way of alignment. Therefore, the stainless-steel bridge which holds the FFPC was mounted on a vacuum compatible positioning system[5] which moves the cavity along this second radial axis. This bridge and the piezo, which works via the slip-stick principle, are shown in Fig. 7.5(a) and (b).

In order to assemble the cavity, we aligned each fiber with a six-axis micro-positioning stage and glued it to its precise position with respect to the trap. The setup is shown in Fig. 7.5(a). This positioning system allowed us to compensate for drifts of the fibers during the curing of the glue. We found that with short cavities of about 70 µm in length, this alignment and gluing method was successful. Unfortunately, long cavities need to

---

[4] Epo-Tek 301 and Epo-Tek 353ND

[5] Omicron, MS 5

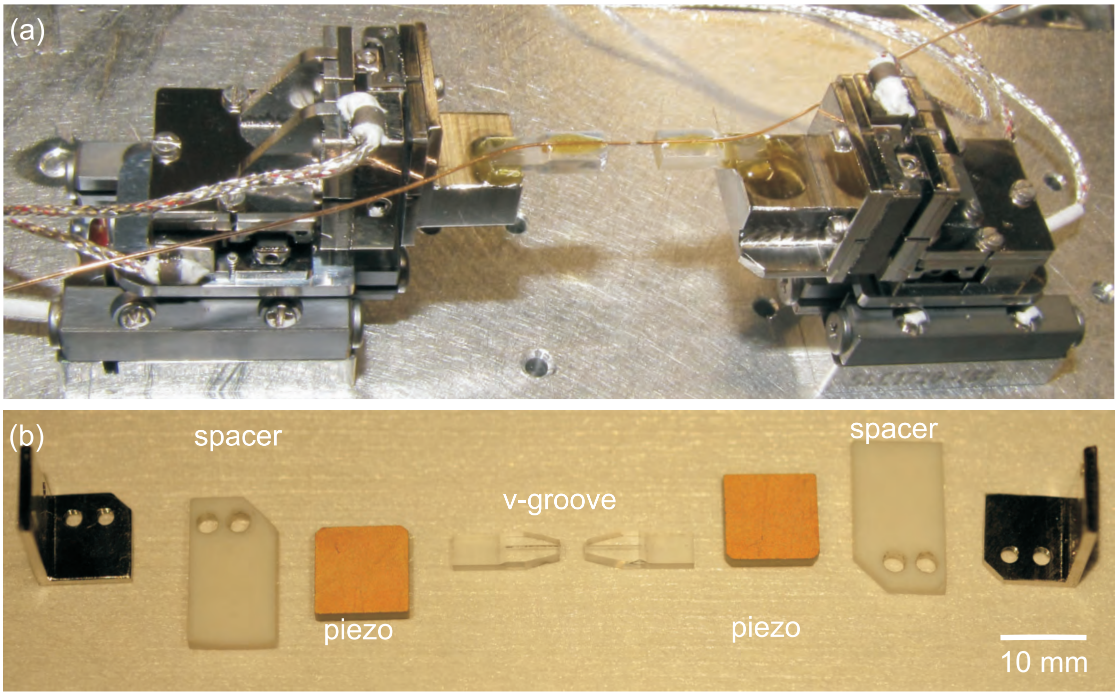

Figure 7.6: FFPC positioning system. (a) 3D nanopositioning setup for each fiber. (b) Each fiber is glued to a glass v-groove and mounted on a shear-mode piezoelectric crystal which allows active length stabilization of the cavity. The piezoelectric crystals are glued to insulating MACOR spacers which are screwed onto the nanopositioning stages.

be aligned with considerably higher precision, and small drifts of the fiber mirrors lead to misalignment of the cavity. Although it was possible to cure the glue while keeping the fiber cavity aligned, the cavity signal degraded over time after the glue had set. Despite our efforts to develop stable alignment methods and to find a UHV glue with suitable properties, the fiber cavities inevitably became misaligned before we could put the complete setup into vacuum. Furthermore, the cavity signal disappeared when the cavity assembly was moved or rotated. These effects may be caused by slight temperature changes or by tension in the cavity mount, and we expect that vacuum baking would also contribute to misalignment. This setup (Fig. 7.5(b)) was then used to test the ion trap without fibers. It may be possible to stabilize the fiber mirror position passively well enough to maintain alignment, but instead we decided on an active technique to mount the fiber cavity inside vacuum.

7.2.2 New version of the FFPC mount

For fiber cavities longer than 150 µm, a new technique was needed to align the cavity for the vacuum setup and to maintain the alignment. Therefore, the cavity mount was redesigned. Each fiber is mounted on a three-axis nanopositioning system compatible with ultra-high vacuum. Along the cavity axis, the fibers can be translated by up to

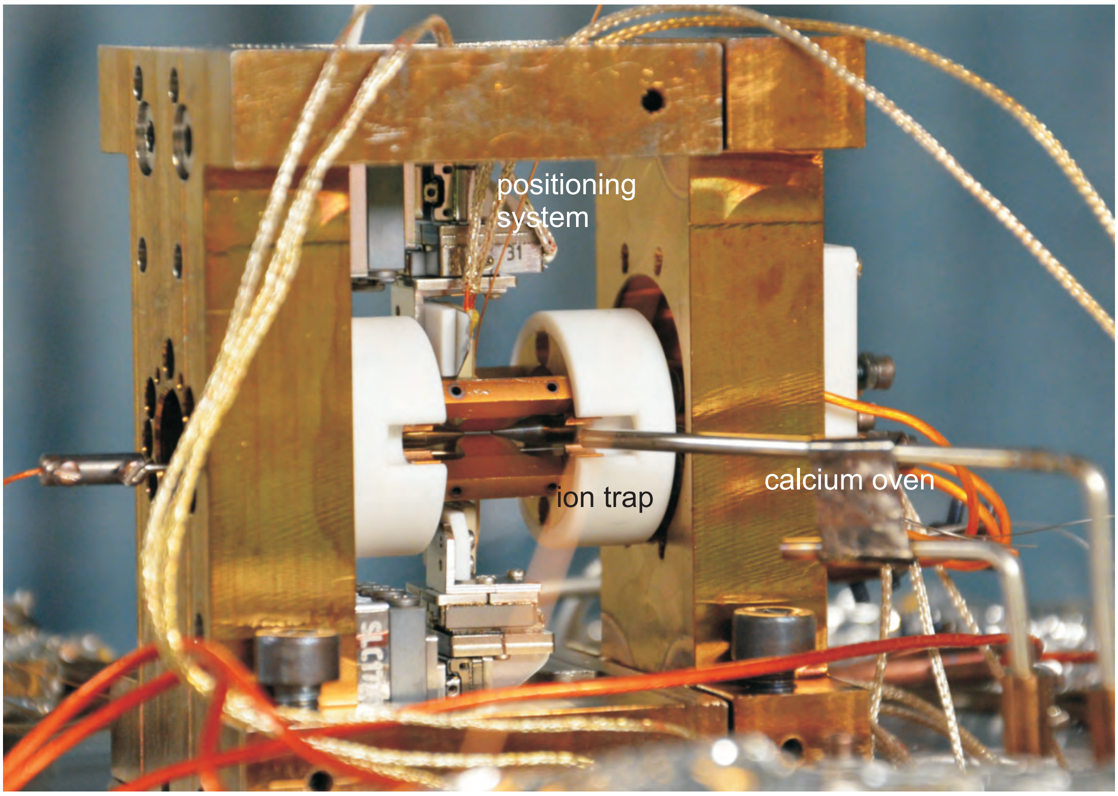

Figure 7.7: Photo of the linear Paul trap with an integrated FFPC. The trap axis is horizontal, and the fiber-positioning systems are visible above and below the trap. The calcium oven points towards the trap center from the right side. Vacuum-compatible BNC cables connect positioners and trap electrodes to vacuum feedthroughs.

12 mm[6]. Along the other two axes, smaller positioners[7] provide 4 mm of traveling range. The positioners operate on the slip-stick principle and have a minimum step size of 50 nm but can be moved with sub-nanometer resolution by charging the piezo actuators. The three-axis system for each fiber has dimensions of $(17 \times 22 \times 21)$ mm^3. Fig. 7.6(a) shows a test setup of an FFPC aligned with the positioning system.

Each fiber is glued to a Pyrex v-groove, which sits on a shear-mode piezoelectric actuator; see Fig.7.6(b). The additional actuator is needed to stabilize the cavity length actively as the bandwidth of the positioning system is too low. These actuators are fixed to the positioners.

To mount these positioners on the same holder as the ion trap, this holder needed to be changed. Therefore, the ion trap also had to be taken apart and be rebuilt afterwards, even though it had been stably trapping before. Fig. 7.7 shows a photo of the ion-trap setup together with the fiber cavity aligned by the micropositioning system.

The in-vacuum positioning system offers a range of advantages for the setup. First, it provides the option of realigning the cavity under vacuum in case of misalignment

---

[6] SMARACT SLC-20

[7] SMARACT SL-06

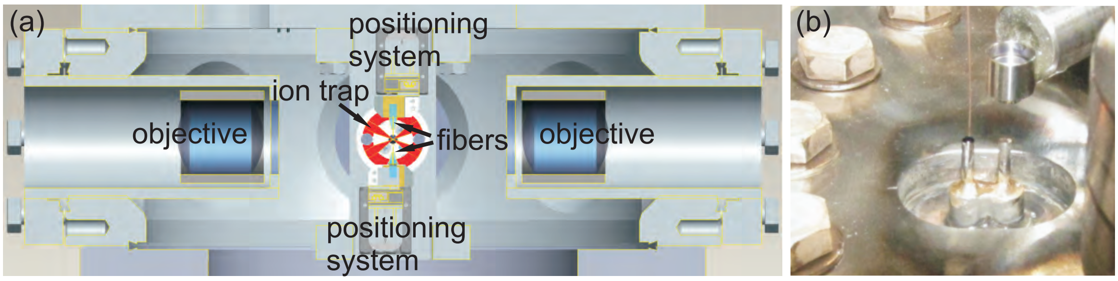

Figure 7.8: (a) Technical drawing of the vacuum vessel and the ion-trap fiber-cavity apparatus. The fibers are mounted from below and above the trap. Objectives which sit inside inverted viewports collect ion fluorescence. (b) Photo of the fiber feedthrough. The right fiber broke at the end of the stainless-steel tube. A lens above the fiber couples light into the fiber in free space.

due to baking or transport of the vacuum chamber. Second, it is possible to pull the fibers back by more than a centimeter from the trapping region, allowing the trapping of ions without dielectrics close and thus no distortion of the potential. Furthermore, in this configuration, the trap blades shield the fibers, and the fiber mirrors do not get coated with calcium while ions are loaded. Later, the fibers can be moved towards the trap center iteratively while compensating for charges on the dielectric mirrors via the compensation electrodes. Finally, the positioners allow us to change the mirror separation of the FFPC inside vacuum and thus build cavities of variable cavity length and waist, resulting in an adjustable coupling parameter g.

7.3 Other experimental tools

7.3.1 Vacuum apparatus

To avoid collisions of the ion with gas particles, the trap needs to be mounted under ultra-high vacuum. The vacuum chamber was designed to optimize vacuum conditions, optical access, and stability requirements for the ion trap and the FFPC.

The cavity fibers are integrated in the ion-trap setup, such that only one plane of optical access is available for lasers and for collection of fluorescence from the ions. We chose the cavity axis to be in the vertical axis of the physical system and mount the trap inside an octagonal vacuum chamber. The chamber then provides optical access from eight sides in the horizontal plane; see Fig. 7.8(a). The axis orthogonal to both the FFPC axis and the trap axis is used for fluorescence detection. Here, within two inverted viewports, high numerical-aperture objectives (Sec. 7.3.2) are installed that allow for efficient light collection and thus fast detection of the state of the ion.

The fibers are fed into vacuum with a home-made fiber feedthrough, comprising stainless-steel tubes brazed into the a vacuum flange (Fig. 7.8(b)). The inner diameter of the tubes is 0.5 mm, and the fibers were glued into the tubes with vacuum epoxy[8]. In contrast to commercial fiber feedthroughs, a home-made feedthrough is advantageous

---

[8] EPOTEC 353ND

as it is compatible with any fiber type, including non-standard cladding diameters.

When closing the vacuum chamber, the single-mode fiber at the air side of the fiber feedthrough brode. The single-mode fiber is used to couple light into the cavity, whereas the multimode fiber is used to detect the cavity signal. To couple light into the single-mode fiber, the broken fiber end was polished, and mounted a fiber-collimator lens above the fiber end. We now couple light into the fiber via this lens.

The trap was mounted together with the FFPC on the top flange of the vacuum chamber. This flange also supports all electrical feedthroughs, the fiber feedthrough, and the calcium oven. A vibration-isolating material[9] is sandwiched between that top flange and the trap mount. The vacuum chamber sits within a hole in an optical breadboard, which allows us to use short mounting posts for optical components, thus providing optimal stability.

7.3.2 Lasers and optics

All lasers used in our experiment are shared with the other experiments situated in the same laboratory. The lasers sit on separate optical tables, and their light is brought to the experimental tables via optical fibers. Details about the laser system can be found in (Bar10). We use lasers of the following four wavelengths to trap and cool our ions.

Doppler cooling and detection: We use the $4^2\mathrm{S}_{1/2} \leftrightarrow 4^2\mathrm{P}_{1/2}$ transition at 396.8 nm to cool and detect the ions. The light is generated from a frequency-doubled titanium-sapphire laser[10] which is pumped by a Verdi[11]. The wavelength is stabilized to a linewidth of about 300 kHz via a reference cavity. A double-pass AOM at 80 MHz is used to change frequency and intensity of the cooling light, and a second AOM at 80 MHz in single-pass configuration is used to switch the light on and off.

Repumping: Light at 866.2 nm is needed to repump the population from the metastable $3^2\mathrm{D}_{3/2}$ state to which the ion can decay from the $4^2\mathrm{P}_{1/2}$ state. The light is produced by a diode laser[12], which, again, is stabilized to a reference cavity. A double-pass AOM at 200 MHz is used for frequency and intensity control of the light field.

Photoionization: To load our ion trap, neutral calcium is ionized via a two-photon process. A laser at 422.6 nm resonantly excites the atoms from the $4^1\mathrm{S}_0$ state to the $4^1\mathrm{P}_1$ state. A second laser at 375 nm then drives a transition from the $4^1\mathrm{P}_1$ state to the continuum, ionizing the atom. Light of both wavelengths is produced by grating stabilized laser diodes[13]. They are coupled into the same optical fiber and brought to the experimental table.

Overlapping of all lasers: To trap and cool ions, it is convenient to have all lasers overlapped and coming in from the same direction. This way, it is easy to make sure that all beams are aligned to the ion simultaneously. We first overlap the beams with two interference filters[14], similar to the setup described in (Pau11). The combined beam is then coupled through the holes in the endcap electrodes of the trap. They provide apertures which align the beam on the ions.

---

[9] DuPont, Kalrez

[10] Coherent, 899 ring laser system, 794 nm

[11] Coherent, Verdi V10, 532 nm

[12] Toptica, DL pro

[13] Toptica, DL 100

[14] Semrock,FF01-395/11-25, Long wave pass 594

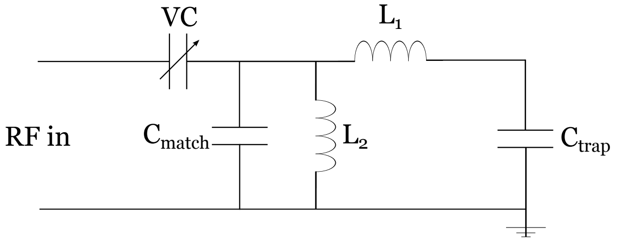

Figure 7.9: Layout of the resonance circuit that drives the trap radio frequency. The capacitance C_{match} is used to match the impedance of the circuit. Two inductances L_1 and L_2 are used. The capacitance of the trap C_{trap} is 16.5 pF.

The cooling beam through the endcaps, however, coincides with the axial direction of the ion trap and thus cools the ions only along this axis. To cool the ions in the other two axes, we use a second cooling beam.

We focus all laser beams on the ions. To minimize scattering from the trap electrodes, we use single-mode fibers to provide a good Gaussian mode. The beam in axial direction is focussed by an achromatic 150 mm lens system. The second cooling beam is focussed through a fiber-coupler lens[15] to a waist of around 15 µm.

Imaging of the ions: A custom designed objective[16] at 397 nm is used to image the ion string. The objective has a numerical aperture of 0.18 and is comprised of a precision cemented doublet with a meniscus lens. The lenses are coated with an anti-reflective coating at 397 nm. With a focal length of 50.5 mm, the objective has a magnification of 24 and is designed for a working distance of 44 mm. Furthermore, it corrects for the aberrations of the 4 mm thick vacuum window. We image the ions with an electron-multiplied charged-coupled device (EM-CCD) camera[17] and a photo-multiplier tube (PMT)[18].

7.3.3 Electronics and computer control

The RF for the trap blades is produced by an RF generator[19] and amplified with an LC resonator circuit (Gan12) and an RF amplifier[20]. Konstantin Friebe and Klemens Schüppert implemented the design of the LC circuit from (Gan12) for our setup; see Fig. 7.9. A tuneable capacity is used for impedance matching of the circuit. The resonance frequency of the circuit is at around 35 MHz with a voltage gain at resonance of 40. A capacitive pick-off measures voltage and frequency of the circuit. The voltage on the blades is 16 times the voltage of the pick-off. Typically we drive the trap with voltages on the order of 60 V RF amplitude.

The DC voltages for the trap electrodes are supplied by a stable, computer-controlled

---

[15] Schäfter Kirchhoff, 60FC-T-4-M60 − 33

[16] CVI Melles Griot, 99AS-200710

[17] Andor, Luca

[18] Hamamatsu, H10682-210

[19] Marconi 2023

[20] Mini Circuits, ZHL-1-2W

high voltage source[21]. These channels are controlled via the experiment control software Trics (Trapped Ion Control Software). The software is developed by Thomas Holleis in collaboration with Florian Zähringer. We use it to control the DC voltages for the ion trap, all our laser AOMs, and to read out the PMT.

Amplitude, frequency and phase of light fields are changed via AOMs. The RF signals to drive the AOMs are steered via Trics on the parallel bus developed by Florian Schreck and coworkers[22]. The data from the control computer are sent to analog and digital output boards via a PCI (Peripheral Component Interconnect) interface[23]. It controls the DDS (direct digital synthesizer) boards which supply the radio frequencies for the AOMs. The bus also provides analog signals and digital signals for switches.

We use the new version of the pulse sequencer box, which was designed an built in 2011 and 2012, to read out the PMT counts and provide digital signals for the experiment. It is controlled with Trics and the PCI interface[24]. Details about the box can be found in (Sch08a).

The positioning piezos which align the fibers are controlled by the software CU3D supplied from SMARACT. A magnetic field is generated via home-built coils that are supplied with a current from a standard power supply[25].

7.4 Results

7.4.1 Ion trapping and trap performance

With the first version of the fiber-cavity mount, we were not able to assemble a stable cavity which could be integrated in the vacuum chamber (Sec. 7.2.1). While developing a redesign, we had time to test the ion trap alone without fibers and characterize its performance. We successfully loaded strings of ions and single ions in the trap (Fig. 7.1 (d)). This test also helped to eliminate the risk of setting up a complicated fiber-cavity system around a non-functional trap or a trap with high heating rates. However, we could not perform heating-rate measurements with this setup as one of the compensation electrodes was found to have an electrical contact with an endcap electrode. Nevertheless, we showed that we were able to trap ions successfully with a lifetime on the order of an hour without compensating for micromotion. Based on this result, we then set up the FFPC around the ion trap.

As the ion-electrode distance is very small, we expect faster ion heating in comparison with larger traps, so that it may be difficult to work with ions in the motional ground state. However, the advantages of this design are manifold: the trap has a deep trapping potential, while the electrode distances are comparable to the size of the fiber cavity. Small traps do not need RF voltages as high as those of large traps and can be driven by simple RF resonators (Gan12). The blade-to-blade separation parallel to the cavity axis is only 150 µm and thus shields ions from the dielectric fibers. The small diameter of the holes in the tip electrodes helps us to align laser beams on the ions.

---

[21] Iseg, EH080 − 20

[22] Details: http://iqoqi006.uibk.ac.at/users/c704250/indexprivate.html

[23] National Instruments, NI PCI-6534

[24] National Instruments, NI PCI-6733

[25] Elektro-Automatik, EA-PS2332-025

We were pleased about the stable performance of this trap, as it was initially unclear whether a miniaturized trap could be fabricated with the precision required to allow stable trapping.

7.4.2 Effects of fibers on ions

After these tests, we opened the vacuum chamber again and installed the fiber cavity together with the redesigned mount. Furthermore, we were able to eliminate the short circuit between compensation electrode and endcap electrode. With the fibers recessed by around a centimeter from the trap center, we were able to trap ions again.

Moving the fibers slowly towards a string of ions, we observe first effects when fibers are at around 1 mm distance to the ions. We observe, that the ions move towards the multimode fiber as it approaches the trap center from below the ion trap. As we decrease the single-mode fiber separation from the trap center, we observe the opposite effect: that the ion move away from this fiber. This effect corresponds to our expectations; that the dielectric material is charged positively and repels the ions. A possible explanation for the fact that the multimode fiber attracts the ions would be that the copper coating begins close to the fiber tip and therefore shorts the RF potential, dragging the ions toward the fiber (Sec. 4.4.5).

These first effects of the fibers on the ions are easy to compensate via the compensation electrodes. As the fibers are moved closer to the ions, however, it becomes increasingly difficult to trap the ions stably and keep them crystalized. We try to compensate for changes in the trap potential by maximizing the fluorescence signal of PMT and CCD camera while adjusting the voltages applied to the trap electrodes. At a fiber-ion separation of around 400 µm, however, the ions are already lost from the trap within minutes and reloading is hardly possible. When moving the fibers even closer, the effects from the fibers prevent us from trapping ions. This fiber-ion separation would correspond to a cavity length of 800 µm. Similar maximal ion-fiber separations are reached, when only one fiber is approached and the second fiber is kept at the maximum distance of more than a centimeter.

One problem that could cause insufficient compensation of charged-induced micromotion is the weak influence of the compensation electrodes orthogonal to the cavity and the trap axis. In this direction, the trap blades open at the small angle of 60° and therefore shield the potential of those electrodes from the trap center.

7.4.3 Discussion

As we were not yet able to trap ions between the cavity fibers successfully, we investigate several possible routes on how to solve the current problems and show coupling between an ion and the fiber cavity.

We work on implementing the 729 nm laser to improve the ion cooling and use the laser as an analysis tool for determining temperature and heating rates of the ions. This knowledge could help us to improve micromotion compensation and trap the ions more stably even with the fibers close to the ions. If we then find that the maximum voltages, which we can apply on the compensation electrodes, are not sufficient to trap the ions stably, we would have to rewire the trap electrodes. By connecting each trap blade separately, DC bias voltages on the blades could be used for additional micromotion compensation.

The setup as it is now already permits us to trap ions and align fibers around them at a fiber-fiber separation of 800 µm. Therefore, we pursue the development of an improved CO_2-laser ablation setup in collaboration with Jakob Reichel's research group that would allow us to build longer cavities (compare Sec. 5.5.1). With this new setup, we expect that it will be possible to overcome current limitations and build FFPCs in the range of millimeter length. The production of such new fibers and their integration into the system should thus allow for larger ion-fiber separations.

8 A new set of CQED parameters for an improved quantum interface

The experimental design of the integrated ion-trap cavity apparatus was introduced in the previous chapter. Here, a perspective on a range of possible experiments with such a setup is provided, and the possibilities for an atom-photon interface in a new parameter regime are presented. This chapter returns to the three experiments presented in Chapter 3 and evaluates their results for this new set of CQED parameters.

Furthermore, this chapter addresses the question of which CQED parameters are optimal for which experiments and if the parameters are in reach with the new fiber-cavity setup. Finally, the thesis concludes with an outlook on future experiments accessible with the new setup and with a combination of both cavity–ion-trap setups in the laboratory.

8.1 The CQED-parameter regime for fiber cavities

The relevant rates of the $^{40}\text{Ca}^{+}$-cavity system are the rate g of oscillatory exchange of excitation between atom and cavity, the cavity damping rate κ, and the atomic decay rate γ of the $P_{3/2}$ state. It is often presumed that experimental protocols all have the ideal result when the system is in the strong coupling regime, for which $g \gg \kappa, \gamma$. However, this is not the case. Generally, the situation is more complicated, and the optimal parameter regime depends on the choice of experiment. Sometimes it is very important that the photon exits the cavity quickly, and a high value of κ is advantageous. For example, in experiments with multiple ions in the cavity (such as heralded two-ion entanglement), a transfer of the excitation back to the ions should be avoided (Sec. 3.5.2). However, with large cavity decay rates of several tens of Megahertz, it becomes impossible to address individual Zeeman substates, unless a very high magnetic field is applied. The addressability of individual Zeeman states is required for all three interface protocols described in Chap. 3. High magnetic fields, however, cause more fluctuations of the Zeeman state energies, leading to decoherence. Furthermore, up to now, we have observed difficulties in cooling the ions properly with magnetic fields exceeding several tens of Gauss.

One advantage of the fiber-cavity setup is the possibility to adjust the cavity length via piezo stages over several hundreds of micrometers and thereby to change both cavity length L and waist w_0. As a consequence, the coherent coupling rate can be adjusted over a wide range, providing the opportunity to set the experimental parameters to optimized values for each specific experiment.

Tab. 8.1 lists the ion-cavity system parameters for various FFPC configurations. The atomic decay γ rate of the $P_{3/2}$ state is $2\pi \times 11.4$ MHz, including all possible decay channels to the $S_{1/2}$, the $D_{3/2}$, and the $D_{5/2}$ manifolds. The single-atom cooperativity is given by $C = \frac{g^2}{2\kappa\gamma}$.

Table 8.1: System parameters for several configurations of ^{40}Ca$^+$–FFPC setups. Mode waist w_0, cavity decay rate κ, coherent coupling rate g, and single-atom cooperativity C are calculated from cavity length L, radii of curvature, and finesse.

(a) Parameters for the FFPC characterized in Sec. 5.4.1:

L (m)	w_0 (m)	$\mathcal{F}$	κ (MHz/2π)	g (MHz/2π)	C
85	5.1	7.16×10^4	15	41	7.5
131	5.4	6.38×10^4	11	31	6
206	3.2	4.49×10^4	10	41	11.6

(b) Parameters for a radius of curvature for both fibers of 500 µm:

700	7.9	1.5×10^5	1.4	14	6.7
800	7.4	1.5×10^5	1.3	14	7.9
900	6.4	1.5×10^5	1.1	16	10.2

(c) Parameters for radii of curvature of 1 mm:

1700	9.9	3×10^5	0.3	7.4	8.6
1800	9.1	3×10^5	0.3	7.8	10.3
1900	7.8	3×10^5	0.3	8.9	14.1

The system parameters for the FFPC characterized in Sec. 5.4.1 are shown in Tab. 8.1 (a). The finesse and the cavity length have been measured, and w_0 and g are calculated from the radii of curvature, which were measured interferometrically. From the table, we see that g is larger than κ and γ over the range of measured cavity lengths.

The cavity decay rate decreases for increasing finesse and cavity length, as $\kappa \propto (\mathcal{F}L)^{-1}$; see Eq. 5.2. The measurement presented in Sec. 5.4.1 shows that the finesse decreases with increasing cavity length. This decrease, however, is small enough that κ still decreases as a function of the cavity length. Furthermore, the cavity waist decreases as the stability limit is approached. Both tendencies lead to higher cooperativities for longer cavity length.

In the case that further efforts still do not allow us to trap ions within the current fibers, we plan to integrate new fibers with longer fiber-fiber separations and thereby reduce the effects of charges on the fibers on the ion. As we have seen in experiments with the actual apparatus, the ions are trapped more stably and influenced less for fibers recessed further from the trap center (Sec. 7.4.2). Therefore, longer cavities clearly offer advantages over short cavities.

Tab. 8.1(b) and Tab. 8.1(c) list parameters for increased cavity lengths and radii of curvature of fibers produced with the new CO$_2$-laser ablation setup (Sec. 5.5.1). The first set of parameters (Tab. 8.1(b)) assumes fiber-mirror radii of curvatures of 500 µm, a cavity length of around 800 µm, and a finesse of 1.5×10^5. The coherent coupling rate for this cavity is slightly higher than the atomic decay rate and considerably higher than the cavity decay rate. The second parameter set (Tab. 8.1(c)) assumes a symmetric cavity constructed from mirrors of 1 mm radius of curvature and even longer cavity length of around 1.8 mm. The finesse is assumed to be 3×10^5. Such a high finesse and a long

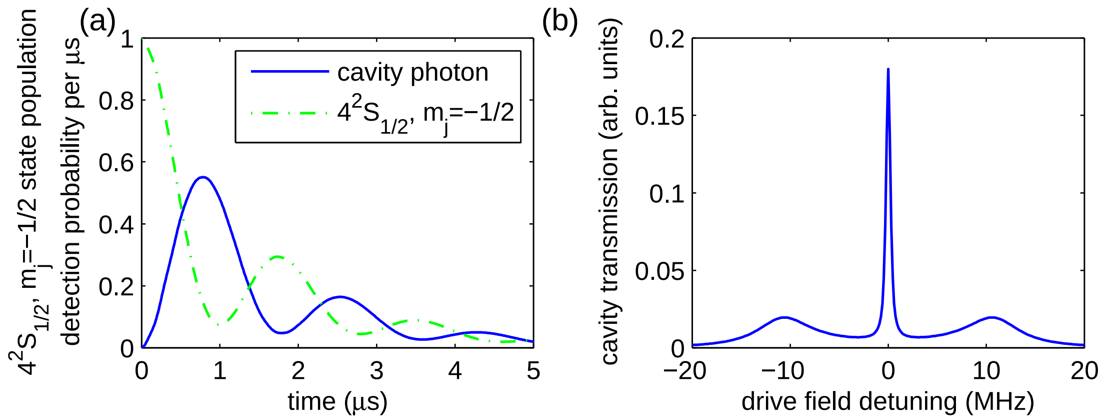

Figure 8.1: (a) Simulation of the temporal shape of a photon exiting the cavity and of the atomic population in $S_{1/2}, m_\mathrm{j} = -1/2$. The ion is initialized in the $S_{1/2}, m_\mathrm{j} = -1/2$ state and driven to the $D_{5/2}, m_\mathrm{j} = -5/2$ state via a Raman transition. In the strong coupling regime, the excitation of the system oscillates back and forth between ion and cavity field. This oscillation can be detected in the shape of the photon leaving the cavity. (b) Simulated cavity transmission spectrum of a $^{40}\mathrm{Ca}^+$ ion coupled to the cavity. The ion is repumped on the $S_{1/2} \leftrightarrow P_{3/2}$ transition.

cavity results in small values for κ. In this configuration, g is slightly smaller than γ. The cooperativity, however is still high.

8.1.1 Demonstrating strong coupling

Once the ion is successfully coupled to the cavity, we want to measure the coupling rate. Two possible experiments for this purpose, which could be used to prove that the system reaches the strong coupling regime, are the measurement of the temporal shape of the cavity photons and the observation of a vacuum Rabi splitting.

When driving a Raman transition from $S_{1/2}$ to $D_{5/2}$, a photon is produced in the cavity. Oscillations in the temporal shape of the photon exiting the cavity indicate that the excitation is repeatedly being transferred coherently from the atom to the cavity photon and back. This emission and reabsorption is only limited by damping in the system, such as the photon leaking out of the cavity. If g dominates over the losses, it is possible to observe these oscillations in the photon which exits the cavity. Fig. 8.1(a) shows a simulation of the temporal shape of the cavity photon, which has such oscillations. The figure also shows the oscillation of the population of $|S_{1/2}, m_\mathrm{j} = 1/2\rangle$, which is the initial state of the simulation. The parameters of the simulation are comparable to the values from Tab. 8.1(c): $g = 2\pi \times 10$ MHz and $\kappa = 2\pi \times 0.3$ MHz.

Measuring this temporal shape of the photon does not provide a direct way to measure g. The photon shape is not only determined by the CQED parameters g, κ, and γ but is also sensitive to the cavity detuning and the Rabi frequency of the drive field and therefore needs to be inferred from simulations.

The best known way to prove strong coupling in a CQED system is the observation of a vacuum Rabi splitting as shown in (Tho92). A vacuum Rabi splitting is the splitting of the normal modes in the eigenvalue spectrum of the strongly coupled atom-cavity system. As the cavity is tuned into resonance with the atom, the coupling leads to a new set of new eigenstates and eigenvalues. The new atom-cavity eigenstates are the positive and negative superposition states of atom or cavity being in the excited state, and the new eigenfrequencies of the coupled states are split by $2g$.

The vacuum Rabi splitting is measured by driving the atom or the cavity with a weak probe field. Two peaks, which are separated by $2g$ in frequency, are observed as the probe detuning is swept across the resonance. This is a conceptually easy measurement in a two-level system, as it can be done in steady state. The situation becomes more difficult for a Λ-type system as ours. To perform a measurement, the ion is initialized in a $D_{5/2}$ state. In the measurement process, the ion can decay from the $P_{3/2}$ state to the $S_{1/2}$ states. Therefore, the system needs to be recycled continuously from the $S_{1/2}$ states. This repump field influences the dynamics of the system.

In Fig. 8.1(b), a simulation of a weak probe field measuring the cavity spectrum of a three-level system in the cavity is plotted. The simulation uses the same CQED parameters as the simulation of the photon shape. As the drive field is detuned from resonance, two peaks which correspond to the coupled atom-cavity states are observed. At zero detuning, an additional sharp peak is present, which is an effect of the repump field.

8.2 Simulations of network protocols for improved CQED parameters

In this section, simulations of the quantum state-mapping and heralded ion-ion entanglement are shown for the new fiber-cavity parameter regime. To keep the simulations comparable to the simulations presented in Chapter 3, the same magnetic fields and detunings are used. For the simulations, values of g and κ similar to those of Tab. 8.1(c) are used.

As we will see, these two experiments would benefit significantly from a higher coupling rate. In contrast, an example of an experiment which would not benefit from an increased g is the ion-photon entanglement described in Sec. 3.4.1. The clever choice of Zeeman states used to store the quantum information in combination with the σ^- driving scheme makes the experiment insensitive to off-resonant excitation followed by spontaneous decay (compare Sec. 3.4.2). However, the cavity with which the experiment was performed has relatively large mirror losses of 68 ppm and only 13 ppm transmission of the outcoupling mirror (Stu12a). Improved coatings with state-of-the-art losses of 2 ppm (Rem92) would increase the efficiency of the process by almost an order of magnitude.

8.2.1 State mapping

Both the process fidelity and the efficiency of the state-mapping protocol (Sec. 3.3) are limited by the fact that the effective coherent coupling rate in the current experimental apparatus ($g = 2\pi \times 0.9$ MHz) is much smaller than the spontaneous decay rate ($\gamma = 2\pi \times 11.4$ MHz). Here, state-mapping simulations that use a coherent coupling rate of

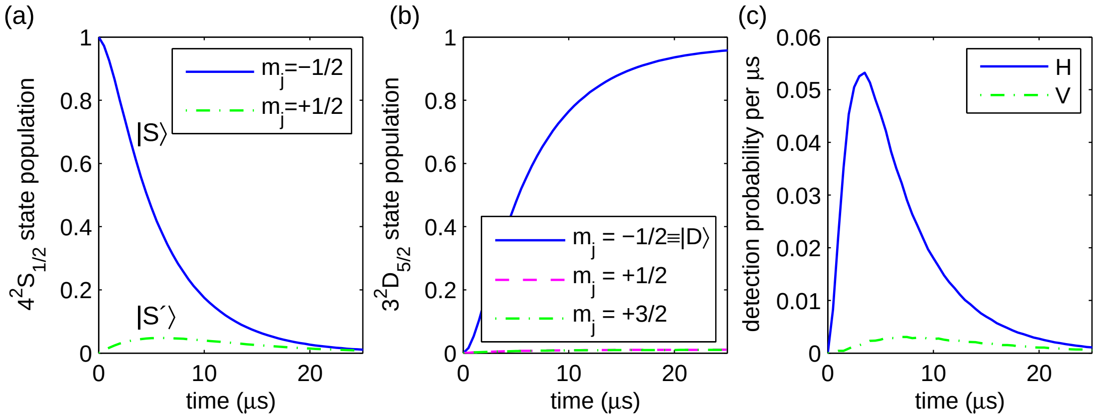

Figure 8.2: State mapping of the electronic state $|S\rangle$ to a horizontally polarized photon. (a) Population in the $S_{1/2}$ states and (b) in the $D_{5/2}$ states. (c) Temporal shape of the photon exiting the cavity. For the simulation, a coherent coupling rate of $2\pi \times 5$ MHz is used. After 40 µs, all the atomic population is in the $3^2D_{5/2}$ manifold, and 97% of the population is in the target state with $m_\mathrm{j} = -1/2$.

$2\pi \times 5$ MHz and a cavity decay rate of $2\pi \times 0.3$ MHz are shown. These values are similar to the parameters shown in Tab. 8.1(c) and are within reach of an FFPC setup.

Fig. 8.2 shows the result of mapping the ion's quantum state $|S\rangle$ to the photon's quantum state $|H\rangle$. The magnetic field of 4.5 G, the Rabi frequency of $\Omega_\mathrm{tot} = 2\pi \times 18$ MHz, and the detuning of -400 MHz from the $|D\rangle \leftrightarrow |P\rangle$ transition of the cavity are the same values as in the simulations described in Sec. 3.3. As the ratio γ/g is much smaller with this new set of parameters, the probability of a scattering event to $|S'\rangle$ and the subsequent production of a photon with the wrong polarization is decreased. Furthermore, the full state-mapping process is much faster, decreasing the impact of detector dark counts and magnetic field fluctuations. Using realistic detector dark counts of 5.6 Hz and magnetic field fluctuations corresponding to an atomic decoherence time of $\tau = 110$ µs, each of the those effects would decrease the process fidelity by less than 1%.

The process fidelity is obtained by evaluating the mapping process for four different initial states, as described in Sec. 3.3.1. Fig. 8.3 shows the process fidelity (a) and efficiency (b) as a function of the photon detection time window. Model 2 of Fig. 8.3 (a) includes detector dark counts, imperfect state initialization with a fidelity of 99%, and magnetic field fluctuations. The process fidelity first rises and reaches its highest value of 96% one microsecond after switching on the bichromatic drive field. Within this one microsecond time window, the photon generation efficiency inside the cavity is 3%. The highest fidelity of the experiment performed with the current apparatus (Fig. 3.5) was (92 ± 2)% at a photon generation efficiency inside the cavity of 0.6% (Sec. 3.3.3). The low fidelity and the following rise at the very beginning of the process is due to an off-resonant Raman process as explained in Sec. 3.3.3.

For this new parameter regime, after 25 µs, no population remains in the $|S\rangle$ state. The photon generation efficiency inside the cavity after 25 µs is 96%, with a process

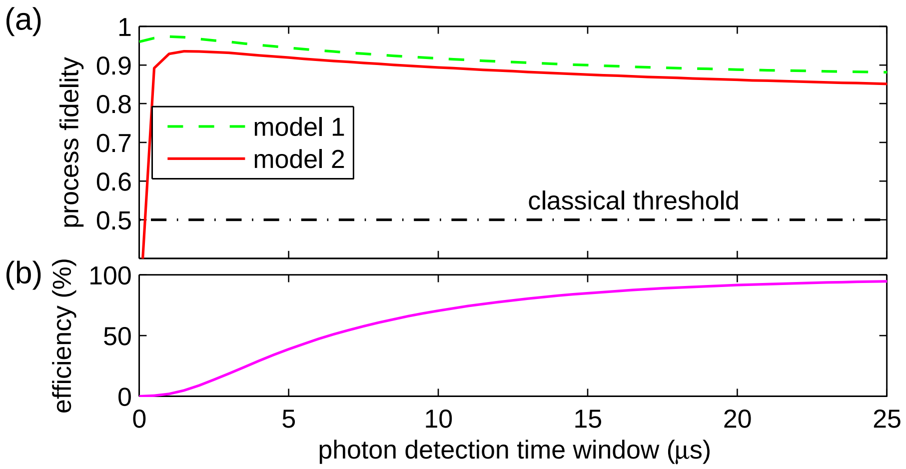

Figure 8.3: (a) Process fidelity and (b) efficiency of the state-mapping process as a function of the photon-detection time window. Model 2 includes detector dark counts, imperfect state initialization, and magnetic field fluctuations. Both fidelity and efficiency are improved by the higher coupling rate g.

fidelity of 85%, as compared to 16% efficiency and (66 ± 1)% fidelity in the current apparatus.

Assuming a fiber cavity with one mirror that is more transmissive than the other, almost all photons would exit the cavity on one side. To maintain polarization information, this fiber would need to be single mode. A realistic value for the coupling efficiency from the cavity mode to the single-mode fiber for a cavity of the parameters used here (Tab. 8.1(c)) is around 50% (Sec. 5.1.2 and Sec. 5.4.2). With mirror losses of 2 ppm and detector losses on the order of 42% of the APDs, the overall efficiency would be 16%, which is still fifteen times higher than the efficiency of the measurement in Sec. 3.3.3.

8.2.2 Ion-ion entanglement

A second example of an experiment that would benefit from improved CQED parameters is the heralded two-ion entanglement. Upon the detection of one horizontally and one vertically polarized cavity photon, two ions are entangled in the cavity, as described in Sec. 3.5. In the current setup with the substrate-mirror cavity, the fidelity of the entangled ion-ion state with respect to the Bell state $|\Psi^+\rangle$ (Eq. 3.25) is mostly limited by off-resonant excitation followed by spontaneous decay from the excited state $|P\rangle$. As this decay causes the fidelity to decrease rapidly with increasing time difference T between the two photons detections, the rate of producing a state with a high fidelity is low.

The simulations, which agree with the experimental results that were presented in Sec. 3.5.3, show that a state with 99% fidelity is produced when only photons with arrival time difference $T \leq 0.5$ µs are counted; this corresponds to 6% of all photons. For $T \leq 4.9$ µs the fidelity with respect to the Bell state decreases to 50%, with 57% of photon pairs taken into account.

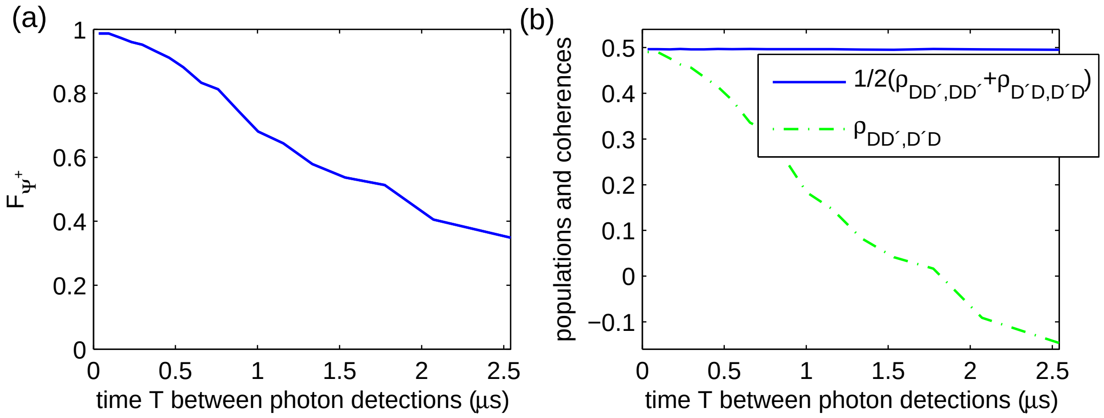

Figure 8.4: (a) Fidelity $\mathcal{F}_{\Psi^+}$ with respect to the Bell state $|\Psi^+\rangle$, and (b) populations and coherences of the entangled state as a function of the photon arrival time difference T. The Monte Carlo simulations were done with $g = 5$ MHz and $\kappa = 0.5$ MHz.

A simulation with fiber-cavity parameters similar to those of Tab. 8.1(c) with $g = 5$ MHz and $\kappa = 0.5$ MHz was carried out. Comparing the experimental results with these new simulations, we find that higher fidelities and efficiencies are reached. The fidelity again decreases as a function of photon arrival time difference; see Fig. 8.4(a). Fig. 8.4(b) shows populations and coherences as a function of T. The population is extracted from the density matrix elements by $1/2(\rho_{\mathrm{DD}',\mathrm{DD}'}+\rho_{\mathrm{D}'\mathrm{D},\mathrm{D}'\mathrm{D}})$ and the coherence is the off-diagonal entry of the density matrix $\rho_{\mathrm{D}'\mathrm{D},\mathrm{DD}'}$. As explained in Sec. 3.5.2, the populations stay constant while the coherences decrease as the arrival time difference increases. In this simulation, a state with 99% fidelity is produced from the first 12% of the photon pairs. Those photons correspond to a threshold $T \leq 0.1$ µs; note that this time difference is smaller than in Sec. 3.5.3 because the overall process of photon generation is now faster. The fidelity with respect to the Bell state decreases to 50% as 88% of photon pairs with $T \leq 1.8$ µs are taken into account.

Stronger coupling between ions and cavity improves the fidelity of the entangled state and considerably speeds up the rate of producing ion-ion entanglement. However, the simulations suggest that it is challenging to improve the CQED parameters further to a point at which the produced state becomes independent of photon arrival time difference.

9 Conclusion and outlook

An ion-cavity apparatus with a large ion-cavity coupling would be the ideal tool for realizing high-fidelity quantum network operations. It promises excellent fidelities for both entangling ions with photons and mapping quantum states from ions to photons. We also expect that it would be possible to perform a reverse state mapping experiment, in which the state of the photon is mapped to the state of the ion with high fidelity and efficiency.

One way to realize this is in an experiment in which the ion first generates a photon which exits the cavity. Then, the same photon is sent back to the cavity and is reabsorbed by the ion. When mapping a photon to the ion, however, the photon shape has to be optimized such that it is coupled into the cavity and absorbed by the ion optimally. This shape corresponds to the time-reversed photon shape generated in the state-mapping experiment. The part of the photon that does not overlap with this shape would be reflected by the cavity. Furthermore, the polarization of the photon leaving the cavity must be maintained in the fiber. This can be accomplished by either using the single-mode side of the current fiber cavity or constructing a new cavity in which both fibers are single mode.

As another experiment, we expect to be able to generate photonic cluster states with high fidelity (Lin09). Such states are a universal resource for measurement-based quantum computation (Rau01). In the ion-cavity apparatus such cluster states can be produced by applying a protocol similar to the atom-photon state-mapping protocol repeatedly, interleaved by rotations on the ion. Through the possibility to perform such local operations on the ion between subsequently generated photons, the ion-cavity system is an optimal candidate system to produce photonic cluster states. With multiple ions coupled to the cavity, furthermore, it is possible to deterministically generate higher dimensional states (Eco10).

The fidelity of the cluster states is limited by the fidelity of the state-mapping process. With the setup in which the state-mapping has already been shown, one-dimensional cluster-states with a single ion in the cavity could be generated. Such minimal cluster states could be produced as a prove-of-principle experiment. With the current fidelities and efficiencies, Andreas Stute estimated that a one-dimensional state of three qubits could be generated and measured within a few hours at a fidelity of around 75%. With the new apparatus, however, both higher fidelities and efficiencies would be possible, and larger one-dimensional states as well as two-dimensional states from two ions with fidelities over 90% could be generated in the same or in less time.

Connecting the two ion-cavity apparatuses via an optical fiber link would realize a prototype of a quantum network in our laboratory. An advantage of the two systems is that they work with the same ion species and, therefore, the cavity photons have the same wavelength. However, the different coupling and cavity-damping rates of the two apparatuses present a challenge because they result in different time scales of the experiments. For the protocols it is important to be able to either match the temporal shapes of the photons that are later detected or to couple a photon directly from one cavity to the other cavity. To tune the temporal shape of the cavity photon it is possible to shape the pulses of the drive lasers (Kel04) and to choose appropriate cavity detunings and thus change the effective coupling rate. A more difficult version would be to try to change g continuously during one experiment in the fiber-cavity setup by moving the fibers or the ions in and out of the cavity mode. In the fiber cavity apparatus, g could be set for each experiment by choosing a specific cavity length.

One possible experiment with the two apparatuses would be to transfer a quantum state from one ion in the first apparatus to another ion trapped in the second apparatus. The quantum state could be mapped from the ion to the photon in the first apparatus and then from the photon to the atom in the second apparatus. In this scenario the apparatus with the substrate cavity could be the one producing the photon, and the fiber-cavity apparatus would be the one receiving the photon. A combined efficiency of this process should around 2% for optimized photon shapes. The efficiency is mainly limited by the losses in the cavity mirrors of the first apparatus, which absorb 84% of the cavity photons (Stu12a).

Entanglement between remote ions could be generated by entangling ion and photon in the first apparatus, and then mapping the photon to the ion in the second apparatus. Another possible experiment to generate entanglement would be the application of the heralded ion-ion entanglement between two distant ions. To ensure that the photons that exit the two distant cavities are indistinguishable, the photons would need to interfere on a beam splitter, generating path interference. For such an experiment, it is important that the photons from the two setups have the same temporal shape, as it should not be known which ion the photon came from. A similar experiment also feasible with the two apparatuses would be the teleportation of a quantum bit between the two remote nodes in a protocol similar to (Nöl13).

This thesis presented technology and methods to implement an improved quantum interface by integrating fiber-based Fabry-Perot cavities with ion traps. In the course of this work, various ion-trap geometries together with the effects of dielectric fibers on the trapped ions were simulated. Furthermore, in collaboration with Jakob Reichel's research group at the ENS in Paris, concave fiber facets were fabricated. These fibers were subsequently coated with a low-loss mirror coating, and the fiber-based optical resonators formed with these mirrors were measured to have record finesses. By comparing fiber-mirrors with superpolished mirrors, we were able to conclude that fiber-surface roughness does not introduce additional losses to the cavity. During my research with fiber-based Fabry-Perot resonators, methods to build and improve fiber cavities that can be integrated with ion traps were developed.

The focus of my work has been the design of a miniaturized linear blade trap and its assembly. The ion trap provides a deep trap depth, room for a fiber cavity, and the trap blades shield the fibers from the ion. The fiber mount allows for the independent micropositioning of each fiber along three axes and thus for in-vacuum cavity alignment and the possibility to change the length of the cavity. Additional fast piezos actively stabilize the cavity length in vacuum. The constructed apparatus has the possibility to reach the strong coupling regime of CQED.

With the setup, we have successfully trapped and crystallized ions by Doppler cooling. The setup is still limited by the effect of the fibers on the ion and coupling from the ion to the cavity has not yet been shown. However, this coupling is in reach with technological improvements of either the ion trap or the FFPCs.

With improved fibers, we expect to be able to construct longer cavities which do not influence the ion's trapping potential. One of the first steps after integrating such a cavity would be to show coupling between ion and cavity field. Furthermore, we would determine the coupling strength of the system, which we expect to be in the strong coupling regime. This can be done by observing the first single-ion vacuum Rabi splitting or oscillations in the temporal shape of the cavity photon.

Integrating the 729 nm laser into our setup is a logical next step. The 729 nm laser that couples the qubit transition would allow for ground state cooling and coherent operations on the ion. This amount of control over the ion in combination with the cavity would allow the realization of high-fidelity quantum network protocols. With two such ion-cavity systems in hand, it would be possible to realize exciting experiments demonstrating elementary quantum network protocols.

Bibliography

[Ata95] E. Atanassova, T. Dimitrova and J. Koprinarova, *AES and XPS study of thin RF-sputtered Ta_2O_5 layers*, Appl. Surf. Sci. **84**, 193 (1995).

[Ban94] N. P. Bansal, *Low-temperature synthesis, pyrolysis and crystallization of tantalum oxide gels*, J. Mat. Sci. **29**, 5065 (1994).

[Bar00] P. A. Barton, C. J. S. Donald, D. M. Lucas et al., *Measurement of the lifetime of the $3d^2D_{5/2}$ state in* ^{40}Ca$^+$, Phys. Rev. A **62**, 032503 (2000).

[Bar09] H. G. Barros, A. Stute, T. E. Northup et al., *Deterministic single-photon source from a single ion*, New J. Phys. **11**, 103004 (2009).

[Bar10] H. G. de Barros, *Raman spectroscopy and single-photon source in an ion-cavity system*, Ph.D. thesis, Leopold-Franzens-Universität Innsbruck (2010).

[Ben08] J. Benhelm, G. Kirchmair, C. F. Roos and R. Blatt, *Towards fault-tolerant quantum computing with trapped ions*, Nat. Phys. **4**, 463 (2008).

[Bir05] K. M. Birnbaum, *Cavity QED with multilevel atoms*, Ph.D. thesis, California Institute of Technology (2005).

[Bli04] B. B. Blinov, D. L. Moehring, L. M. Duan and C. Monroe, *Observation of entanglement between a single trapped atom and a single photon*, Nature **428**, 153 (2004).

[Bra11] G. Brady, A. Ellis, D. Moehring et al., *Integration of fluorescence collection optics with a microfabricated surface electrode ion trap*, Appl. Phys. B **103**, 801 (2011).

[Car93] H. Carmichael, *An Open Systems Approach to Quantum Optics*, Springer, 1993.

[Cas13] B. Casabone, A. Stute, K. Friebe et al., *Heralded entanglement of two ions in an optical cavity* (2013).

[Cet13] M. Cetina, A. Bylinskii, L. Karpa et al., *One-dimesional array of ion chains coupled to an optical cavity* (2013), arxiv:1302.2904.

[Chi05] J. Chiaverini, R. B. Blakestad, J. Britton et al., *Surface-electrode architecture for ion-trap quantum information processing*, Quantum Information & Computation **5**, 419 (2005).

[Chw09] M. Chwalla, J. Benhelm, K. Kim et al., *Absolute Frequency Measurement of the $^{40}Ca^+$ $4s\,^2S_{1/2} - 3d\,^2D_{5/2}$ Clock Transition*, Phys. Rev. Lett. **102**, 023002 (2009).

[Cir97] J. I. Cirac, P. Zoller, H. J. Kimble and H. Mabuchi, *Quantum State Transfer and Entanglement Distribution among Distant Nodes in a Quantum Network*, Phys. Rev. Lett. **78**, 3221 (1997).

[Col07] Y. Colombe, T. Steinmetz, G. Dubois et al., *Strong atom-field coupling for Bose-Einstein condensates in an optical cavity on a chip*, Nature **450**, 272 (2007).

[CT98] C. Cohen-Tannoudji, J. Dupont-Roc and G. Grynberg, *Atom-Photon Interactions*, John Wiley & Sons, Inc., 1998.

[Cui06] G. Cui, J. M. Hannigan, R. Loeckenhoff et al., *A hemispherical, high-solid-angle optical micro-cavity for cavity-QED studies*, Opt. Express **14**, 2289 (2006).

[Deh75] H. G. Dehmelt, *Proposed* 10^14 *Dv < v Laser Fluorescence Spectroscopy on* Tl^+ *Mono-Ion Oscillator II (spontaneous quantum jumps)*, Bull. Am. Phys. Soc. **20** (1975).

[Deu08] C. Deutsch, *High finesse fibre Fabry-Perot resonators. Production, characterization and applications*, Master's thesis, Fakultät für Physik, Ludwig-Maximilians Universität München (2008).

[Dre83] R. W. P. Drever, J. L. Hall, F. V. Kowalski et al., *Laser phase and frequency stabilization using an optical resonator*, Appl. Phys. B **31**, 97 (1983).

[Dua03] L.-M. Duan and H. J. Kimble, *Efficient engineering of multiatom entanglement through single-photon detections*, Phys. Rev. Lett. **90**, 253601 (2003).

[Dub10] F. Dubin, C. Russo, H. Barros et al., *Quantum to classical transition in a single-ion laser*, Nat. Phys. **6**, 350 (2010).

[Eco10] S. E. Economou, N. Lindner and T. Rudolph, *Optically Generated 2-Dimensional Photonic Cluster State from Coupled Quantum Dots*, Phys. Rev. Lett. **105**, 093601 (2010).

[Enk97] S. J. van Enk, J. I. Cirac and P. Zoller, *Ideal Quantum Communication over Noisy Channels: A Quantum Optical Implementation*, Phys. Rev. Lett. **78**, 4293 (1997).

[Fis59] E. Fischer, *Die dreidimensionale Stabilisierung von Ladungsträgern in einem Vierpolfeld*, Zeitschr. Phys. **159**, 1 (1959).

[Gan12] D. Gandolfi, M. Niedermayr, M. Kumph, M. Brownnutt and R. Blatt, *Compact radio-frequency resonator for cryogenic ion traps*, Rev. Sci. Instrum. **83**, 084705 (2012).

[Gar04] C. Gardiner and P. Zoller, *Quantum Noise: A Handbook of Markovian and Non-Markovian Quantum Stochastic Methods with Applications to Quantum Optics*, Springer Series in Synergetics, Springer, 2004.

[Gho95] P. K. Ghosh, *Ion traps*, Clarendon Press, 1995.

[Gla63] R. J. Glauber, *Coherent and Incoherent States of the Radiation Field*, Phys. Rev. **131**, 2766 (1963).

[Goy83] P. Goy, J. M. Raimond, M. Gross and S. Haroche, *Observation of Cavity-Enhanced Single-Atom Spontaneous Emission*, Phys. Rev. Lett. **50**, 1903 (1983).

[Gul01] S. Gulde, D. Rotter, P. Barton et al., *Simple and efficient photo-ionization loading of ions for precision ion-trapping experiments*, Appl. Phys. B **73**, 861 (2001).

[Gul03] S. T. Gulde, *Experimental Realization of Quantum Gates and the Deutsch-Jozsa Algorithm with Trapped* $^{40}\mathrm{Ca}^{+}$ *Ions*, Ph.D. thesis, Leopold-Franzens-Universität Innsbruck (2003).

[Gut01] G. R. Guthöhrlein, M. Keller, K. Hayasaka, W. Lange and H. Walther, *A single ion as a nanoscopic probe of an optical field*, Nature **414**, 49 (2001).

[Häf08] H. Häffner, C. Roos and R. Blatt, *Quantum computing with trapped ions*, Phys. Rep. **469**, 155 (2008).

[Hän75] T. Hänsch and A. Schawlow, *Cooling of gases by laser radiation*, Optics Communications **13**, 68 (1975).

[Har10] M. Harlander, M. Brownnutt, W. Hänsel and R. Blatt, *Trapped-ion probing of light-induced charging effects on dielectrics*, New J. Phys. **12**, 093035 (2010).

[Hei87] D. J. Heinzen, J. J. Childs, J. E. Thomas and M. S. Feld, *Enhanced and inhibited visible spontaneous emission by atoms in a confocal resonator*, Phys. Rev. Lett. **58**, 1320 (1987).

[Her08] P. Herskind, A. Dantan, M. Langkilde-Lauesen et al., *Loading of large ion Coulomb crystals into a linear Paul trap incorporating an optical cavity*, Appl. Phys. B **93**, 373 (2008).

[Her09] P. Herskind, A. Dantan, J. Marler, M. Albert and M. Drewsen, *Realization of collective strong coupling with ion Coulomb crystals in an optical cavity*, Nat. Phys. **5**, 494 (2009).

[Hun10] D. Hunger, T. Steinmetz, Y. Colombe et al., *A fiber Fabry – Perot cavity with high finesse*, New J. Phys. **12**, 065038 (2010).

[Jam98] D. James, *Quantum dynamics of cold trapped ions with application to quantum computation*, Appl. Phys. B **66**, 181 (1998).

[Jam01] D. F. V. James, P. G. Kwiat, W. J. Munro and A. G. White, *Measurement of qubits*, Phys. Rev. A **64**, 052312 (2001).

[Jay63] E. T. Jaynes and F. W. Cummings, *Comparison of quantum and semiclassical radiation theories with application to the beam maser*, Proc. IEEE **51**, 89 (1963).

[Jia07] L. Jiang, J. M. Taylor, A. S. Sørensen and M. D. Lukin, *Distributed quantum computation based on small quantum registers*, Phys. Rev. A **76**, 062323 (2007).

[Jin93] J. Jin and D. A. Church, *Precision lifetimes for the* Ca$^+$ $4p^2P$ *levels: Experiment challenges theory at the 1% level*, Phys. Rev. Lett. **70**, 3213 (1993).

[Joy84] W. B. Joyce and B. C. DeLoach, *Alignment of Gaussian Beams*, Appl. Opt. **23** (1984).

[Kel03] M. Keller, B. Lange, K. Hayasaka, W. Lange and H. Walther, *Deterministic coupling of single ions to an optical cavity*, Appl. Phys. B **76**, 125 (2003).

[Kel04] M. Keller, B. Lange, K. Hayasaka, W. Lange and H. Walther, *Continuous generation of single photons with controlled waveform in an ion-trap cavity system*, Nature **431**, 1075 (2004).

[Kim08] H. J. Kimble, *The quantum internet*, Nature **453**, 1023 (2008).

[Kim11] Y.-S. Kim, Y.-C. Jeong, S. Sauge, V. Makarov and Y.-H. Kim, *Ultra-low noise single-photon detector based on Si avalanche photodiode*, Rev. Sci. Instrum. **82**, 093110 (2011).

[Kla10] F. Klauser, S. Ghodbane, R. Boukherroub et al., *Comparison of different oxidation techniques on single-crystal and nanocrystalline diamond surfaces*, Diam. Relat. Mater. **19**, 474 (2010).

[Kre04a] A. Kreuter, *Spontaneous Emission of a Single Trapped Ca$^+$-Ion*, Ph.D. thesis, Leopold-Franzens-Universität Innsbruck (2004).

[Kre04b] A. Kreuter, C. Becher, G. P. T. Lancaster et al., *Spontaneous Emission Lifetime of a Single Trapped Ca$^+$ Ion in a High Finesse Cavity*, Phys. Rev. Lett. **92**, 203002 (2004).

[Lam11] L. Lamata, D. R. Leibrandt, I. L. Chuang et al., *Ion Crystal Transducer for Strong Coupling between Single Ions and Single Photons*, Phys. Rev. Lett. **107**, 030501 (2011).

[Lei03a] D. Leibfried, R. Blatt, C. Monroe and D. Wineland, *Quantum dynamics of single trapped ions*, Rev. Mod. Phys. **75**, 281 (2003).

[Lei03b] D. Leibfried, B. DeMarco, V. Meyer et al., *Experimental demonstration of a robust, high-fidelity geometric two ion-qubit phase gate*, Nature **422**, 412 (2003).

[Lei09] D. R. Leibrandt, J. Labaziewicz, V. Vuletić and I. L. Chuang, *Cavity Sideband Cooling of a Single Trapped Ion*, Phys. Rev. Lett. **103**, 103001 (2009).

[Lin09] N. H. Lindner and T. Rudolph, *Proposal for Pulsed On-Demand Sources of Photonic Cluster State Strings*, Phys. Rev. Lett. **103**, 113602 (2009).

[Liu05] X. Liu, K.-H. Brenner, M. Wilzbach et al., *Fabrication of alignment structures for a fiber resonator by use of deep-ultraviolet lithography*, Appl. Opt. **44**, 6857 (2005).

[Lou73] R. Loudon, *The quantum theory of light*, Oxford University Press Inc., New York, 1973.

[Lyn03] T. W. Lynn, *Measurement and control of individual quanta in cavity QED*, Ph.D. thesis, California Institute of Technology (2003).

[Mai09] R. Maiwald, D. Leibfried, J. Britton et al., *Stylus ion trap for enhanced access and sensing*, Nature Phys. **5**, 551 554 (2009).

[Mau09] P. Maunz, S. Olmschenk, D. Hayes et al., *Heralded Quantum Gate between Remote Quantum Memories*, Phys. Rev. Lett. **102**, 250502 (2009).

[Mil88] P. W. Milonni and J. H. Eberly, *Lasers*, John Wiley and Sons, 1988.

[Mil05] R. Miller, T. E. Northup, K. M. Birnbaum et al., *Trapped atoms in cavity QED: coupling quantized light and matter*, J. Phys. B **38**, S551 (2005).

[Moe07] D. L. Moehring, P. Maunz, S. Olmschenk et al., *Entanglement of single-atom quantum bits at a distance*, Nature **449**, 68 (2007).

[Mon11a] T. Monz, *Quantum information processing beyond ten-ion qubits*, Ph.D. thesis, Leopold-Franzens-Universität Innsbruck (2011).

[Mon11b] T. Monz, P. Schindler, J. T. Barreiro et al., *14-qubit entanglement: creation and coherence*, Phys. Rev. Lett. **106**, 130506 (2011).

[Mul09] A. Muller, E. B. Flagg, M. Metcalfe, J. Lawall and G. S. Solomon, *Coupling an epitaxial quantum dot to a fiber-based external-mirror microcavity*, Appl. Phys. Lett. **95**, 173101 (2009).

[Mul10] A. Muller, E. B. Flagg, J. R. Lawall and G. S. Solomon, *Ultrahigh-finesse, low-mode-volume Fabry–Perot microcavity*, Opt. Lett. **35**, 2293 (2010).

[Mun02] A. B. Mundt, A. Kreuter, C. Becher et al., *Coupling a Single Atomic Quantum Bit to a High Finesse Optical Cavity*, Phys. Rev. Lett. **89**, 103001 (2002).

[Mun03] A. B. Mundt, *Cavity QED with Single Trapped* Ca^+*-Ions*, Ph.D. thesis, Leopold-Franzens-Universität Innsbruck (2003).

[Nag86] W. Nagourney, J. Sandberg and H. Dehmelt, *Shelved optical electron amplifier: Observation of quantum jumps*, Phys. Rev. Lett. **56**, 2797 (1986).

[Nöl13] C. Nölleke, A. Neuzner, A. Reiserer et al., *Efficient Teleportation Between Remote Single-Atom Quantum Memories*, Phys. Rev. Lett. **110**, 140403 (2013).

[Nor08] T. E. Northup, *Coherent control in cavity QED*, Ph.D. thesis, California Institute of Technology (2008).

[Pau58] W. Paul, O. Osberghaus and E. Fischer, *Ein Ionenkäfig*, Tech. Rep. 415 (1958).

[Pau90] W. Paul, *Electromagnetic traps for charged and neutral particles*, Rev. Mod. Phys. **62**, 531 (1990).

[Pau11] A. Pauli, *Classical control of an ion in a surface trap*, Master's thesis, Leopold-Franzens-Universität Innsbruck (2011).

[Rai01] J. M. Raimond, M. Brune and S. Haroche, *Manipulating quantum entanglement with atoms and photons in a cavity*, Rev. Mod. Phys. **73**, 565 (2001).

[Rau01] R. Raussendorf and H. J. Briegel, *A One-Way Quantum Computer*, Phys. Rev. Lett. **86**, 5188 (2001).

[Rem92] G. Rempe, R. J. Thompson, H. J. Kimble and R. Lalezari, *Measurement of ultralow losses in an optical interferometer*, Opt. Lett. **17**, 363 (1992).

[Rie05] M. Riebe, *Preparation of entangled states and quantum teleportation with atomic qubits*, Ph.D. thesis, Leopold-Franzens-Universität Innsbruck (2005).

[Rit12] S. Ritter, C. Nölleke, C. Hahn et al., *An elementary quantum network of single atoms in optical cavities*, Nature **484**, 195 (2012).

[Roh01] H. Rohde, S. T. Gulde, C. F. Roos et al., *Sympathetic ground-state cooling and coherent manipulation with two-ion crystals*, J. Opt. B **3**, S34 (2001).

[Roo00] C. F. Roos, *Controlling the quantum state of trapped ions*, Ph.D. thesis, Leopold-Franzens-Universität Innsbruck (2000).

[Roy11] A. Roy and M. D. Barrett, *Fabrication of glass micro-cavities for cavity quantum electrodynamics experiments*, Appl. Phys. Lett. **99**, 171112 (2011).

[Rus08] C. M. Russo, *Photon statistics of a single ion coupled to a high-finesse cavity*, Ph.D. thesis, Leopold-Franzens-Universität Innsbruck (2008).

[Rus09] C. Russo, H. G. Barros, A. Stute et al., *Raman spectroscopy of a single ion coupled to a high-finesse cavity*, Appl. Phys. B **95**, 205 (2009).

[Sac00] C. Sackett, D. Kielpinski, B. King et al., *Experimental entanglement of four particles*, Nature **404**, 256 (2000).

[Sau86] T. Sauter, W. Neuhauser, R. Blatt and P. E. Toschek, *Observation of Quantum Jumps*, Phys. Rev. Lett. **57**, 1696 (1986).

[Sch93] C. Schrama, E. Peik, W. Smith and H. Walther, *Novel miniature ion traps*, Opt. Commun. **101**, 32 (1993).

[Sch08a] P. Schindler, *Frequency synthesis and pulse shaping for quantum information processing with trapped ions*, Master's thesis, Leopold-Franzens-Universität Innsbruck (2008).

[Sch08b] S. A. Schulz, U. G. Poschinger, F. Ziesel and F. Schmidt-Kaler, *Sideband cooling and coherent dynamics in a microchip multi-segmented ion trap*, New J. Phys. **10**, 045007 (2008).

[Sch12] K. Schüppert, *Birefringence in fiber cavities*, Master's thesis, Leopold-Franzens-Universität Innsbruck (2012).

[Sco76] J. Scofield, *Hartree-Slater subshell photoionization cross-sections at 1254 and 1487 eV*, J. Electron Spectrosc. Rel. Phenom. **8 (2)**, 129 (1976).

[Sei06] S. Seidelin, J. Chiaverini, R. Reichle et al., *Microfabricated Surface-Electrode Ion Trap for Scalable Quantum Information Processing*, Phys. Rev. Lett. **96**, 253003 (2006).

[Sie86] A. E. Siegman, *Lasers*, University Science Books, Sausalito, CA, 1986.

[Slo13] L. Slodička, G. Hétet, N. Röck et al., *Atom-Atom Entanglement by Single-Photon Detection*, Phys. Rev. Lett. **110**, 083603 (2013).

[Sø99] A. Sørensen and K. Mølmer, *Quantum Computation with Ions in Thermal Motion*, Phys. Rev. Lett. **82**, 1971 (1999).

[Spl09] F. E. Splatt, *Development and Operation of Miniaturized Ion Traps for Scalable Quantum Computation*, Ph.D. thesis, Leopold-Franzens-Universität Innsbruck (2009).

[Ste06] T. Steinmetz, Y. Colombe, D. Hunger et al., *Stable fiber-based Fabry-Pérot cavity*, Appl. Phys. Lett. **89**, 111110 (2006).

[Ste12] J. D. Sterk, L. Luo, T. A. Manning, P. Maunz and C. Monroe, *Photon collection from a trapped ion-cavity system*, Phys. Rev. A **85**, 062308 (2012).

[Ste13] M. Steiner, H. M. Meyer, C. Deutsch, J. Reichel and M. Köhl, *Single Ion Coupled to an Optical Fiber Cavity*, Phys. Rev. Lett. **110**, 043003 (2013).

[Stu12a] A. Stute, *A light-matter quantum interface: ion-photon entanglement and state mapping*, Ph.D. thesis, Leopold-Franzens-Universität Innsbruck (2012).

[Stu12b] A. Stute, B. Casabone, B. Brandstätter et al., *Toward an ion-photon quantum interface in an optical cavity*, Appl. Phys. B **107**, 1145 (2012).

[Stu12c] A. Stute, B. Casabone, P. Schindler et al., *Tunable ion-photon entanglement in an optical cavity*, Nature **485**, 482 (2012).

[Stu13] A. Stute, B. Casabone, B. Brandstätter et al., *Quantum-state transfer from an ion to a photon*, Nature Photonics **7**, 219 (2013).

[Tan99] S. M. Tan, *A computational toolbox for quantum and atomic optics*, J. Opt. B: Quantum Semiclass. Opt. **1**, 424 (1999).

[Tho92] R. J. Thompson, G. Rempe and H. J. Kimble, *Observation of normal-mode splitting for an atom in an optical cavity*, Phys. Rev. Lett. **68**, 1132 (1992).

[Tog10] E. Togan, Y. Chu, A. S. Trifonov et al., *Quantum entanglement between an optical photon and a solid-state spin qubit*, Nature **466**, 730 (2010).

[Tru05] M. Trupke, E. Hinds, S. Eriksson et al., *Microfabricated high-finesse optical cavity with open access and small volume*, Appl. Phys. Lett. **87**, 211106 (2005).

[Tur00] Q. A. Turchette, Kielpinski, B. E. King et al., *Heating of trapped ions from the quantum ground state*, Phys. Rev. A **61**, 063418 (2000).

[Van10] A. P. VanDevender, Y. Colombe, J. Amini, D. Leibfried and D. J. Wineland, *Efficient Fiber Optic Detection of Trapped Ion Fluorescence*, Phys. Rev. Lett. **105**, 023001 (2010).

[Vol06] J. Volz, M. Weber, D. Schlenk et al., *Observation of Entanglement of a Single Photon with a Trapped Atom*, Phys. Rev. Lett. **96**, 030404 (2006).

[Wal94] D. Walls and G. Milburn, *Quantum Optics*, Springer-Verlag, Berlin, 1994.

[Wer09] G. Werth, V. N. Gheorghe and F. G. Major, *Charged particle traps II*, Springer-Verlag Berlin Heidelberg, 2009.

[Wil11] A. Wilson, H. Takahashi, A. Riley-Watson et al., *Fiber-coupled single ion as an efficient quantum light source* (2011), arxiv:1101.5877.

[Win75] D. Wineland and H. G. Dehmelt, *Proposed* 10^{14} *Dv* $<$ *v Laser Fluorescence Spectroscopy on* Tl^+ *Mono-Ion Oscillator III (spontaneous quantum jumps)*, Bull. Am. Phys. Soc. **20** (1975).

[Wue59] R. F. Wuerker, H. Shelton and R. V. Langmuir, *Electrodynamic Containment of Charged Particles*, J. Appl. Phys. **30**, 342 (1959).

[Zäh12] F. Zähringer, *Quantum walks and relativistic quantum simulations with trapped ions*, Ph.D. thesis, Leopold-Franzens-Universität Innsbruck (2012).

[Zol05] P. Zoller, T. Beth, D. Binosi et al., *Quantum information processing and communication*, Eur. Phys. J. D **36**, 203 (2005).

Journal publications

The work of this thesis resulted in the following publications:

- **B. Brandstätter**, A. McClung, K. Schüppert, B. Casabone, K. Friebe, A. Stute, P.O. Schmidt, C. Deutsch, J. Reichel, R. Blatt, T.E. Northup, *Integrated Fiber-Mirror Ion Trap for Strong Ion-Cavity Coupling*, submitted (2013).
- B. Casabone, A. Stute, K. Friebe, **B. Brandstätter**, R. Blatt, T.E. Northup, *Heralded entanglement of two ions in an optical cavity*, submitted (2013).
- A. Stute, B. Casabone, **B. Brandstätter**, K. Friebe, T.E. Northup, R. Blatt, *Quantum-state transfer from an ion to a photon*, Nature Photonics **7**, 219-222 (2013).
- A. Stute, B. Casabone, P. Schindler, T. Monz, P.O. Schmidt, **B. Brandstätter**, T.E. Northup, R. Blatt, *Tunable ion-photon entanglement in an optical cavity*, Nature **485**, 482-485 (2012).
- A. Stute, B. Casabone, **B. Brandstätter**, D. Habicher, P.O. Schmidt, T.E. Northup, R. Blatt, *Toward an ion-photon quantum interface in an optical cavity*, Applied Physics B, **107(4)**: 1145-1157 (2012).
- T.E. Northup, **B. Brandstätter**, A. Stute, B. Casabone, D. Habicher, A. McClung, J. Ghetta, P.O. Schmidt, J. Reichel, R. Blatt, *Cavity QED with single trapped ions*, ICOLS Conference Proceedings (2011).